

DISSERTATION

Laser ablation of high bandgap materials: Novel process strategies for efficient light-material interaction

ausgeführt zum Zwecke der Erlangung des akademischen Grades eines
Doktors der technischen Wissenschaften

unter der Leitung von
ao. Univ.-Prof. Dr. rer. nat. Georg A. Reider
am Institut für Photonik E387

eingereicht an der Technischen Universität Wien,
Fakultät für Elektrotechnik und Informationstechnik von

DI(FH) Sandra Zoppel

Matrikelnummer 0126965
Schwabengasse 5
6971 Hard

Dornbirn, im Juni 2008

Acknowledgements

I would like to thank my supervisor Georg Reider for his great support through all the years of my PhD work. Although there is a distance of more than 600 km between my lab and his office I was perfectly supervised. I could never imagine how much one can discuss and learn via telephone. I will especially treasure our journeys to various conferences which always led into some kind of adventures.

I would like to express my gratitude to Costas Fotakis. Impressed by his strong personality and kindness it was a pleasure of being part of his institute for awhile. A special thank goes to Maria Farsari. She was my supervisor during my time as a Marie Curie fellow at Forth. She took great care of me from the first day on and was always more like a friend to me. Nevertheless we made great research work during this short time and I will always bear this special time in remembrance.

Special thanks go to Wolfgang Kautek who spent his narrow time in examine my thesis. With his comments and criticism I was able to increase the quality of my work.

Additional I would like to thank my colleagues at the Research Center for Microtechnology. I capitalized on working with an interdisciplinary group of researchers which was an important impact for my thesis. Great thanks go to Johann Zehetner. Especially in the beginning he was a big support joining me in the lab for extensive “from dusk `til dawn”-experiments. Additional I want to thank the head of our group, Johannes Edlinger, who always knows how to inspire us with his expertise in combination with a special “have fun” attitude.

Thanks go to Günther Stangl. He was my source for all the samples you can't buy and a support in everything which deals with excimer lasers. Special thanks go to my cousine Ju for always hosting me during my times in Vienna. She is one of the reasons why I love to visit Vienna.

I am very grateful for Harald, the second half of my heart, who always was there for me also in times when my head was just filled with photons. Nevertheless just he was the absolute term during this time.

Finally I would like to thank my parents for their boundless love. My mother naturally had pity with my unattended student household and my father always stocked me up with fresh fish to keep me healthy. To them and to my beloved grandmother I dedicate my thesis. Unfortunately she was not able to be with me until the end. I will drink a second glass of champagne on your behalf.

Table of Contents

Table of Contents	5
<u>Chapter 1: Introduction and survey</u>	9
<u>Chapter 2: Theory of ablation</u>	11
2.1. Ablation mechanisms	11
2.1.1 Thermal ablation	11
Melting and evaporation	13
2.1.2 Nonthermal ablation	14
Photochemical– photophysical ablation	14
Two temperature model - Plasma induced ablation	14
Nonlinear absorption and impact ionization	16
Optical breakdown	20
Coulomb explosion	23
Ultrafast melting, Phase explosion	23
Shockwave generation	25
<u>Chapter 3: Properties of Semiconductors and dielectrics</u>	29
Silicon, single crystal	31
Strontium titanate	32
Silicon carbide	33
<u>Chapter 4: Experimental</u>	35
4.1. Laser Systems	35
4.1.1 Excimer lasers	35
4.1.2 Solid-State lasers	36
4.2. Determination of the beam- and ablation parameters	38
4.2.1 Fluence and intensity of the laser pulse	39
4.2.2 Threshold fluence	40
4.2.3 Ablation rate	42
<u>Chapter 5: Influence of the pulse duration in ablation of 3C-SiC and SrTiO₃</u>	43
5.1.1 Experimental	44
5.1.2 Results	46
5.1.3 Morphology	50
<u>Chapter 6: Selective ablation schemes</u>	55
6.1. Thin Film removal for Photovoltaic Applications	55
6.2. Selective Laser Ablation of Photoresists for MEMS Devices	60
<u>Chapter 7: Two color ablation</u>	69
7.1. Two color ablation: Nanosecond pulses	70
7.2. Picosecond pulses: Delay time dependence of the yield enhancement	73

7.3. Theoretical considerations on the two-color ablation scheme	78
7.4. Morphology	81
<u>Chapter 8: Morphological effects of laser ablation</u>	85
Ripple formation	85
<u>Chapter 9: Conclusions</u>.....	91
References	95
List of Publications	101
Conference Contributions	103
Invited Presentations	103
Oral Presentations	103
Poster presentations	104
List of figures	107
Index of symbols and abbreviations	113
Appendix	115

Chapter 1: Introduction and survey

Laser materials processing is of great interest for industrial applications as well as for scientific investigations. The underlying laser-material interaction depends on the specific properties of the laser system such as wavelength, pulse duration and peak power. Emission in the visible to the infrared spectra enables the use of the laser as a heat source where laser systems for drilling, cutting, bonding or welding are well established. Main advantages of the laser as a manufacturing tool are the high speed at which a laser beam can be moved and, contrary to mechanical tools, laser light is not subject to wear and tear. The beam as a massless tool can eliminate the need of complex mechanical holders so that handling of brittle materials on the one side or very soft and sensitive materials on the other side is facilitated. Moving to shorter wavelengths enables linear absorption of materials exhibiting wider band gaps which increases the variety of materials processed by laser light. Laser sources emitting in the UV permit linear absorption and processing even of high band gap materials like glass. For example excimer lasers can be operated at wavelengths down to 157 nm to bridge a band gap of up to 7.9 eV.

By applying intensities high enough, laser ablation occurs where material is removed from the sample surface. Depending on the laser parameters, the underlying mechanisms of laser ablation are of different nature. The influence of the specific laser properties on the laser-material interaction and the resulting ablation is discussed in chapter 2.

This work mainly discusses the structuring of semiconductors and insulators with focus on technologically important materials like silicon or silicon carbide where laser ablation is shown to be a promising process solution compared to conventional structuring methods. The properties of these materials and the particular samples used in this work are discussed in chapter 3.

By looking deeper into the ablation process it can be split up into an absorption process to generate free electrons and the consecutive heating of the electron gas by free carrier excitation. As mentioned before the wavelength has to be short enough to obtain efficient linear absorption. On the other hand, the heating of the electron gas scales with the square of the wavelength. Because of this λ^2 -dependence of the free carrier heating rate, IR-irradiation is much more efficient for the further energy deposition into the electron system. Based on these considerations a “two-color scheme” is discussed in this work, where for both processes the suitable wavelength is provided to enhance the overall ablation process. The possibility to generate harmonic wavelengths by simply inserting a nonlinear crystal into the beam allows two-color ablation with the fundamental wavelength and a fraction of the

second and third harmonic, respectively. The ablation enhancement by “harmonics seeding” is discussed in chapter 7 with focus on semiconductor materials.

Besides the wavelength, the pulse duration of the laser source is the main parameter influencing the nature of the laser-material coupling. Pulse durations of down to a few femtoseconds are available from state of the art laser systems. The high peak intensities provided by ultrashort pulses initiate multiphoton absorption mechanisms, bridging a band gap much larger than the photon energy. Thus, by applying ultrashort pulses the ablation of nearly any material is possible by multiphoton absorption. In addition the ablation process happens on time scales so short that no significant thermal diffusion can take place. Moreover, compared to pulse durations in the nanosecond time scale or longer, no radiation is scattered by ablated products. The non-thermal nature of ultrashort pulsed ablation together with the ultrafast mechanism offers well-defined ablation threshold fluences and enables laser structuring with high precision.

This well-defined ablation threshold was demonstrated in literature to allow even sub-wavelength structuring if the laser fluence is controlled to be close to the ablation threshold. Chapter 6 of this work capitalizes on these ablation characteristics of ultrashort pulses to be able for selective material removal from a substrate. The use of ultrashort pulsed ablation for structuring thin film solar cells is demonstrated where the removal of minimized line widths at high process speed and without thermal damage is required. As prototypical systems, the ablation of Molybdenum and two different transparent conductive oxides (TCOs) on glass substrates were studied.

Next to thin film structuring, the selective ablation scheme is a tool for 2½-dimensional patterning. One possible application is the ablation of thick photoresist from substrates. In this case the substrate acts as an etch-stop layer. The structuring of thick photoresist is discussed, showing the potential of this mask- and developmentless method to build prototypes faster than with conventional lithography methods where a mask is needed for the pattern generation.

Chapter 2: Theory of ablation

2.1. Ablation mechanisms

Laser ablation is the general term for material removal by intense coherent radiation. The underlying mechanisms differ significantly depending on the laser sources. Wavelength, pulse duration and peak power are the dominant laser parameters in this case. The wavelength provided from laser sources which are relevant for industrial applications range from the deep UV up to the far IR. As an example, F₂-excimer lasers emit at 157 nm (7.9 eV) whereas a CO₂ laser exhibits a wavelength of 10.6 µm (0.12 eV). Next to the wavelength an enormous range of pulse durations spanning six orders of magnitude (from tens of fs to ns) influences the ablation process. Generally the mechanisms can be divided in thermal and nonthermal ablation.

2.1.1 Thermal ablation

For pulse durations in the nanosecond time regime thermal ablation occurs. The temperature distribution during nanosecond laser ablation can be expressed by the parabolic heat equation given by

$$\frac{K}{D} \frac{\partial T(x, y, z, t)}{\partial t} = K \nabla^2 T(x, y, z, t) + q(x, y, z, t) . \quad \text{Equ. 1}$$

where K [Wm⁻¹K⁻¹] is the thermal conductivity and D [m²s⁻¹] the thermal diffusivity. In many cases it is feasible to simplify this equation to a one-dimensional problem where just the heat flow in z-direction is considered:

$$\frac{K}{D} \frac{\partial T(z, t)}{\partial t} = K \frac{\partial^2 T(z, t)}{\partial z^2} + q(z, t) \quad \text{Equ. 2}$$

with the source term given by

$$q(z, t) = \alpha (1 - R) I(t) e^{-\alpha z} \quad \text{Equ. 3}$$

where R is the reflectivity of the material for the particular wavelength, α [m^{-1}] the linear absorption coefficient and q the heat deposition per unit volume per unit time as a function of position and time [58].

This simplification is allowed for geometries where the illuminated area is big in comparison to the optical penetration depth and the thermal diffusion length. According to Beers Law the optical penetration depth is given by

$$l_{\alpha} = \frac{\lambda}{4\pi\kappa}, \quad \text{Equ. 4}$$

where λ is the wavelength and κ is the imaginary part of the index of refraction, which describes the decay of the intensity inside the bulk caused by linear absorption. After the distance of l_{α} the intensity has decreased by a factor of e .

The energy coupling of the radiation into the bulk is given by $q(z,t)$ and the temperature distribution inside the material is given by thermal diffusion.

A value which allows the estimation of the thermal load affecting the material is the thermal diffusion length. It is defined by

$$l_{diff} = 2\sqrt{Dt} \quad \text{Equ. 5}$$

and describes the distance covered by an isotherm during the time t [58]. In the case of pulsed laser sources the time t is corresponding to the pulse duration. For good heat conductors like metals ($l_{diff} \gg l_{\alpha}$), the temperature on the material surface can be calculated by

$$T(z = 0, t) = \frac{2(1 - R)I\sqrt{Dt}}{K\sqrt{\pi}} \quad [58]. \quad \text{Equ. 6}$$

The equation is simplified assuming a constant intensity value over the time t and a uniform energy deposition over the illuminated area. The temperature of the material increases – depending on the material – within the duration of the laser pulse. The heating of the material occurs within the optical penetration depth. A simple approximation on the temperature after the laser pulse in a volume given by the diffusion length l_{diff} and the laser spot area A_L can be calculated from the energy balance

$$mC\Delta T = I(1-R)\tau_p A_L \quad \text{Equ. 7}$$

where m is the mass heated up by the laser energy and C is the heat capacity of the material. With $C = K/\rho D$ where ρ is the material density and $m = \rho A_L l_{diff}$ equation 7 can be written as

$$T = \frac{I(1-R)\tau_p D}{l_{diff} K} = \frac{I(1-R)\tau_p D}{2\sqrt{D\tau_p} K} = \frac{I(1-R)\sqrt{D\tau_p}}{2K}. \quad \text{Equ. 8}$$

Compared to the calculated heat on the sample surface given by equation 6, the temperature according to equation 8 is of a factor 0.56 smaller due to the assumption of a homogenous heat distribution inside the volume $A l_{diff}$.

Melting and evaporation

Up to now just heating of the material was estimated without onset of a phase transformation. If the temperature is matching the melting point of the material it changes from its solid to the liquid state. For further energy deposition it can often be assumed that the thermal properties of the molten and the solid material does not vary marginally (e.g. a factor of the order of two for metals [58]) so the same assumptions can be taken to estimate further increasing of the temperature to the evaporating point.

Due to cooling of the uppermost surface region by evaporation and radiation, the underlying bulk may exhibit higher temperatures leading to an explosive material removal of the underlying melted material and the formation of an ablation plume containing vapor and droplets (debris).

For material removal with pulse durations in the nanosecond time scale, ablation and the formation of a plume starts during the pulse. As a consequence, a shielding effect occurs where a fraction of the pulse energy is lost by scattering and absorption by the ablation products. So the overall ablation behavior depends on laser/plume interactions and not only on the above mentioned interactions of light with bulk material. If pulse durations in the pico- or femtosecond timescale are employed, the process of energy input into the bulk and ablation are temporally decoupled.

2.1.2 Nonthermal ablation

Photochemical– photophysical ablation

A reduction of the thermal load on the material is possible by choosing short wavelengths and/or employing ultrashort laser pulses.

By employing wavelengths in the UV range the high photon energy may be sufficient for direct bond breaking. The UV lasers used in this work are excimer lasers emitting at 248 nm (5eV) and 193 nm (6.4eV), respectively. As a consequence, single atoms or clusters desorb from the surface and no thermal interaction with the bulk material takes place. This mechanism is known in the literature as “photochemical ablation”, describing a purely nonthermal process [15] where the probability of direct bond breaking increases with increasing photon energy. If a significant fraction of electrons drop back to lower energy levels and the energy is transferred to the lattice, a combination of both thermal and non-thermal mechanisms leads to “photophysical ablation”.

Two temperature model - Plasma induced ablation

When employing femtosecond laser pulses the heat equation can not be used in this form because the absorption of the energy (by electrons) happens on timescales shorter than the electron-phonon coupling. The electron system and the lattice are not in equilibrium and the temperature of both systems has to be calculated separately in a two-temperature model [15]. In figure 1 a schematic graph of the two-temperatur model compared to thermal ablation is shown.

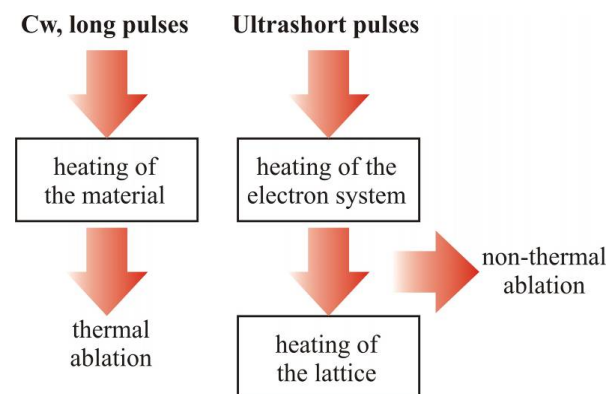


Figure 1: Schematic graph of the two-temperature model. When the energy deposition happens on an ultrashort time scale the heating of the electrons and the lattice has to be considered separately

Compared to thermal ablation where the electron system and the lattice are in equilibrium, non-thermal ablation occurs before significant energy transfer from the thermalised electrons to the lattice can take place.

It should be noted that the two-temperature model is also suitable to describe the ablation of metals with ultrashort pulses. The model assumes a high concentration of electrons in the conduction band permitting the fast heating of the electron gas. In the case of insulators or semiconductors preceding processes to obtain a conduction band population have to be considered. For the model two corresponding heat equations are given for the lattice and the electron system:

$$C_e \frac{\partial T_e}{\partial t} = \nabla(K_e \nabla T_e) - \Gamma_{e-ph}(T_e - T_l) + q(x, y, z, t) \quad \text{Equ. 9}$$

and

$$C_l \frac{\partial T_l}{\partial t} = \nabla(K_l \nabla T_l) + \Gamma_{e-ph}(T_e - T_l) \quad \text{Equ. 10}$$

C_l and C_e are the heat capacities of the electron and the lattice system, respectively, Γ_{e-ph} is the electron-phonon coupling and K_e is the thermal conductivity of the electrons. The primary source term remains the same as for the one-temperature model. The first term on the right-hand side describes the heat conduction within the lattice and the electron systems, respectively. The heat equations are linked by an additional term which considers the electron-phonon coupling.

For pulse durations in the femtosecond region, no energy transfer from the electrons to the lattice occurs during the pulse. As a consequence the electron-phonon coupling can be ignored as well as the heat conduction of the lattice and by electrons during the exposure time. After the pulse, energy transfer from the electron system to the lattice occurs. In Figure 2 the evolution of the lattice and the electron temperature of a 100 nm thick nickel foil are calculated for a pulse duration of 200 fs ($\lambda = 400$ nm, $F \sim 23$ mJ/cm²). The solid line displays the temperature on the front side and the dashed line the temperature of the rear side of the sample. The thermalisation of the electrons occurs during the laser pulse which is in this case within 200 fs. Subsequently, thermal equilibrium is attained at a picosecond timescale depending on the electron-phonon coupling. The strong coupling in case of Ni permits a faster cooling of the electrons on a time scale of several picoseconds which leads to a reduced energy transport into the bulk by electron diffusion. As a consequence, these

materials are characterized by lower damage thresholds for ablation with ultrashort pulse durations.

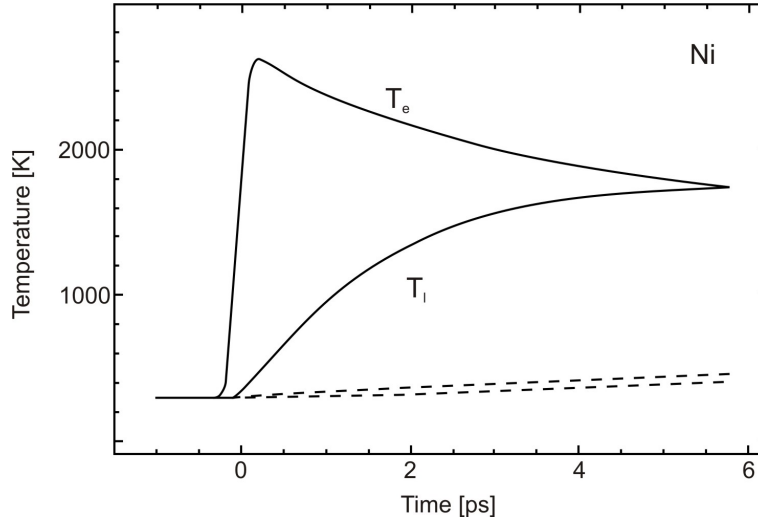


Figure 2: Temperature of the electron system and the lattice versus time on the front (solid lines) and the back surface (dashed lines) of a 100 nm thin nickel foil irradiated with 200 fs pulses at 400 nm ($F \sim 234 \text{ mJ/cm}^2$). Thermal equilibrium is reached after a time of approx. 6 ps [15]

For femtosecond pulse durations the energy transfer from electrons to the lattice occurs in situ whereas for pulse durations in the picosecond timescale or longer diffusion of electrons can not be ignored. The distance covered by diffusion is given by $l_e \approx \sqrt{K_e \tau_e / C_e}$.

The two-temperature model is a feasible tool to describe the laser material interaction up to moderate fluences. Various experiments show that for higher values the ablation rate shows a saturation effect due to changes of the optical and thermal properties of the material during the pulse which is not covered by this model.

Nonlinear absorption and impact ionization

By choosing shorter pulse durations for a given pulse energy nonlinear optical processes may become relevant due to higher peak intensities affecting the material. Materials with a band gap higher than the photon energy of the laser wavelength can be ablated by two- or multi-photon absorption. The linear and two-photon absorption is given by

$$\frac{dI}{dz} = -\alpha I - \beta I^2 \quad \text{Equ. 11}$$

where α is the linear and β is the two photon absorption coefficient. As an example silicon has a linear absorption coefficient of $\alpha = 2.19 \cdot 10^3 \text{ m}^{-1}$ [20] and a two-photon absorption coefficient of $\beta = 1.5 \text{ cm/GW}$ [50],[109] at a wavelength of 1064 nm. The two-photon absorption and the linear absorption are equal when $\alpha I = \beta I^2$, which is at an intensity of $I = 14.6 \text{ GW/cm}^2$.

The equation can be directly integrated to yield the intensity as a function of the distance z .

$$I(z, t) = \frac{I(0, t)e^{-\alpha z}}{1 + \beta I(0, t)[1 - e^{-\alpha z}] / \alpha} \quad \text{Equ. 12}$$

In figure 3 the decrease of intensity versus penetration depth is shown for three ratios of the linear and TP absorption coefficient. The abscissa and the ordinate are normalized to the initial intensity and to the optical penetration depth, respectively. For values of $\alpha \gg \beta I$, the process is dominated by linear absorption and the intensity drops, as expected, to I_0/e at the distance of $l_\alpha = 1/\alpha$. At incident intensities for which $\alpha \sim \beta I$, the absorption increases slightly whereas for a dominant two-photon process ($\alpha \ll \beta I$) it can be seen that most of the energy is absorbed within a very narrow region compared to the optical penetration depth.

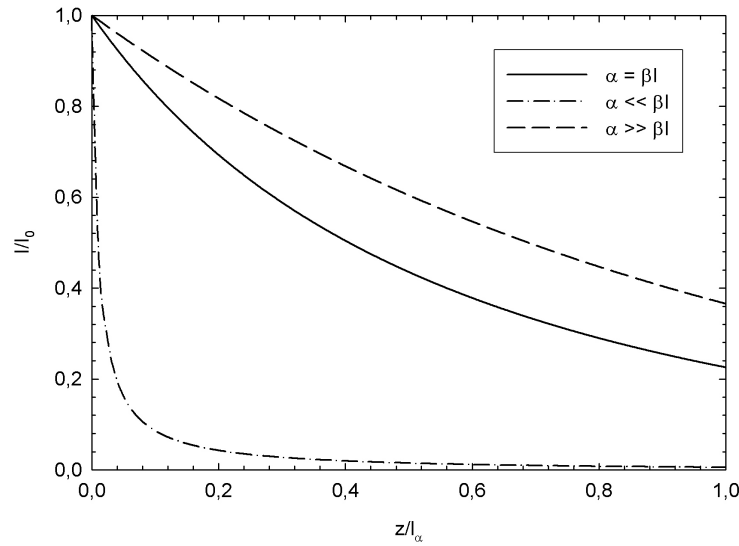


Figure 3: Decay of the intensity versus penetration depth for different ratios of the linear and TPA coefficient. The axes are normalized to the initial intensity and to the optical penetration depth, respectively

In Figure 4 the decay of the TPA is shown for various values of the initial intensity to outline the intensity dependence of the nonlinear absorption process. Considering a Gaussian spacial

profile of the pulse, the nature of the TPA leads to changes of the absorption during the pulse. Efficient absorption initiates at the rising edge of the pulse where the intensity reaches a value high enough for a dominant two-photon absorption process.

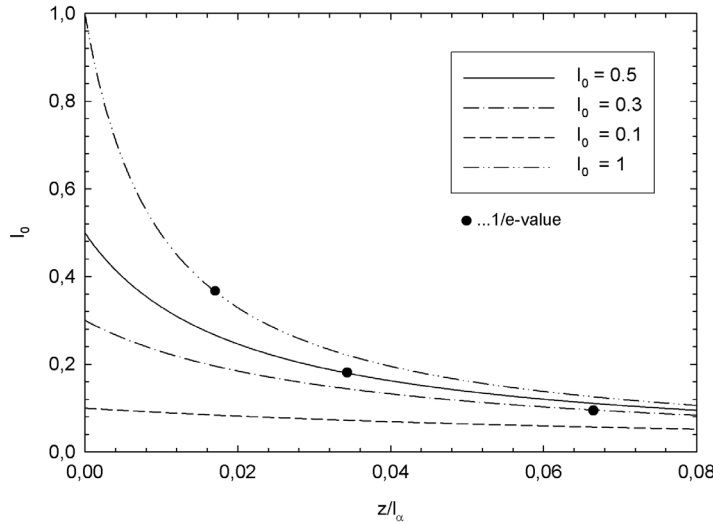


Figure 4: Decay of the intensity versus distance for different values of the initial intensity

Once carriers are excited into the conduction band, they gain energy by free carrier absorption where the free carrier heating rate scales with λ^2 (Drude Model). Originally transparent materials become highly absorbing due to free carrier absorption where the initial population of electrons in the conduction band has to be achieved by an n -photon process. The process of photon absorption and electron acceleration is called “inverse Bremsstrahlung”, characterized by a free-free absorption where a free electron is present in the initial and the final state.

Subsequently, the hot electron gas exhibit sufficient energy to generate additional free carriers by impact ionization of lattice atoms (production of additional electron-hole pairs). This effect is denoted in the literature as “avalanche ionization”, leading, together with the above mentioned absorption processes, to a fast increasing carrier density in the conduction band [26]. The evolution of the free carrier density by avalanche ionization and n -photon absorption can be calculated by the rate equation

$$\frac{dN_e}{dt} = \alpha_a I(t) N_e(t) + \sum_{i=2}^n \beta_i I^i(t) - \gamma N_e^2. \quad \text{Equ. 13}$$

The first term describes the change of the electron density by impact ionization with the avalanche coefficient α_a . The second term considers the multi-photon excitation where β_m is proportional to the n -photon absorption cross-section. Depending on the bandgap of the material and the laser wavelength, n is the minimum number of photons necessary to bridge the band gap ($n\hbar\nu \geq E_g$). It represents a direct ionization by the laser light and thus just depends on the laser pulse intensity $I(t)$ whereas the first term exhibits an additional dependence on the instantaneous electron density leading to electron avalanche. An additional third term is possible to consider a recombination channel which has, however, a minor influence for femtosecond pulse durations.

The n -photon absorption process generates “seed” electrons with the ionization peaking at the maximum intensity of the laser pulse. After the pulse maximum, the photoionization becomes less important and the seed electrons serve to initiate the avalanche process. In figure 5 the generation of electrons in the conduction band is shown versus time for a 100 fs laser pulse with an intensity of 12 TW/cm² ($\lambda = 1053$ nm). The data has been calculated for fused silica [74] where 8-photon absorption is required to overcome the bandgap of 9 eV. The comparison of a pure multiphoton process (dashed line) with the additional avalanche process highlights the dependency of the avalanche on the present electron density.

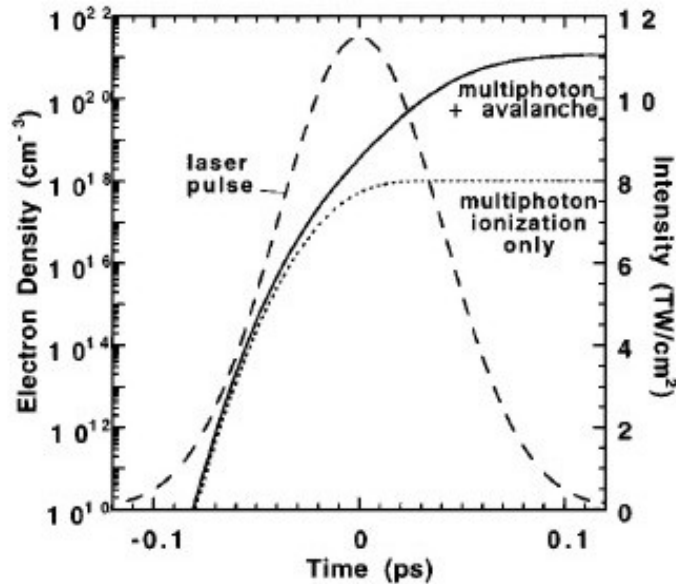


Figure 5: Evolution of the electron density due to multiphoton and avalanche ionization with respect to the intensity envelope of a Gaussian laser pulse [74]

Optical breakdown

When a critical electron density is exceeded, material damage occurs by “Optical Breakdown”. Typical values for the critical electron density (N_e^{cr}) are 10^{19} to 10^{21} per cubic centimeter which is close to the value at which the plasma becomes reflective. The corresponding laser fluence for ablation can be calculated by

$$F_{cr} = \frac{2}{\alpha_a} \ln\left(\frac{N_{cr}}{N_0}\right) \quad \text{with} \quad N_0 = N_s \int_{-\infty}^{\infty} \sigma_n \left(\frac{I(t)}{\hbar\omega} \right)^n dt \quad \text{Equ. 14}$$

assuming that the processes of MPA and avalanche ionization are serial in time and thus can be separated [9]. N_0 is the number of electrons in the conduction band produced by multiphoton absorption. It can be seen that the fluence is strongly dependent on the intensity whereas it changes only logarithmically with the multiphoton cross section σ_n and the critical density. For high intensities the critical density plasma can be exclusively achieved by multiphoton absorption. For such intensities the threshold fluence scales with $\tau^{(n-1)/n}$ for a dominant n -photon process. It should be noted that these estimations are valid for materials where the critical electron density for optical breakdown is close or below the value where the plasma starts being reflective and no further energy can be coupled into the bulk.

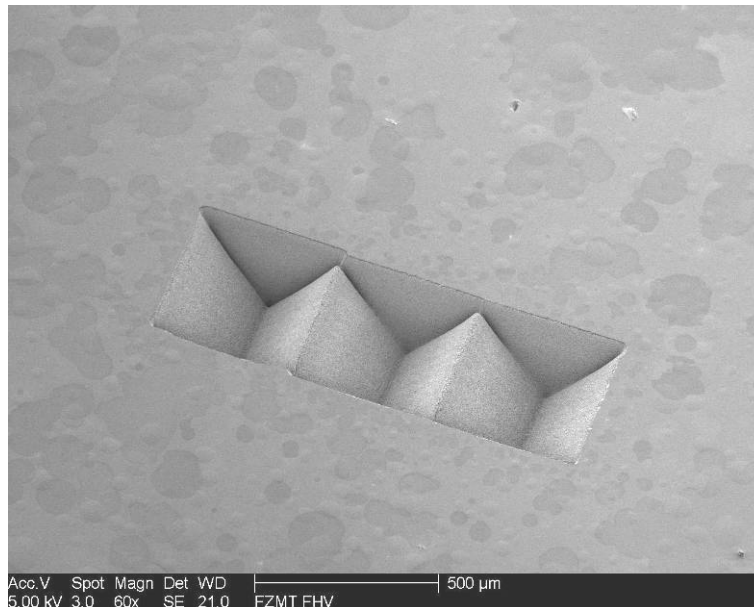


Figure 6: Cavity ablated in glass with a pulse duration of 300 fs at a wavelength of 1040 nm and a repetition rate of 1 kHz demonstrating high quality structuring by plasma-induced ablation with ultrashort laser pulses.

Typical power densities causing ablation by optical breakdown are approx. 10^{11} W/cm² for solids and fluids and 10^{14} W/cm² [73]. In the literature the terms “plasma-induced” or “plasma-mediated ablation” are widely used for this ablation process. In this case - by using adequate laser parameters - very clean and high resolution patterning can be achieved where thermal impact and mechanical load on the material can be excluded. An example is the three-dimensional test structure that has been ablated in glass with a pulse duration of 300 fs at a wavelength of 1040 nm (figure 6).

Pulse durations short enough to render thermal diffusion negligible show sharp and well-defined ablation threshold fluences. This offers the possibility to ablate structures smaller than the beam diameter [61],[87] which is schematically demonstrated in figure 7.

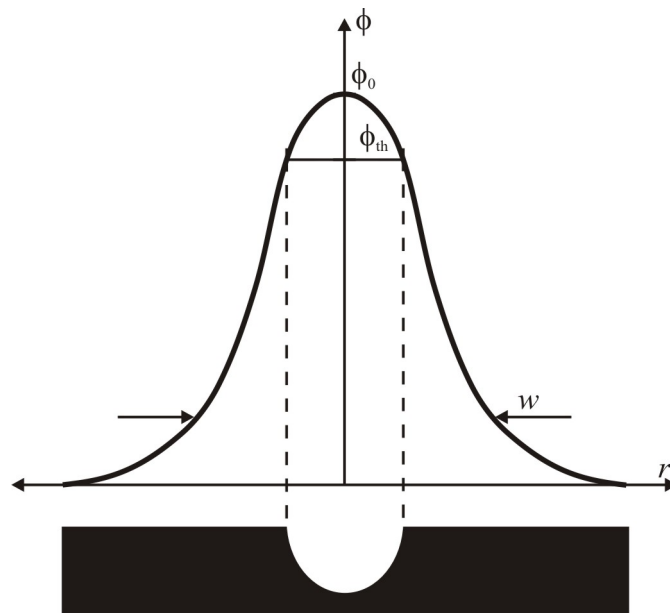


Figure 7: Well-defined ablation thresholds in ultrashort pulsed laser ablation enables feature sizes smaller than the beam diameter by tuning the intensity close to the threshold value

Laser-induced optical breakdown may lead to various physical effects like plasma formation, shock wave generation as well as cavitation or jet formation if breakdown occurs inside soft tissues or fluids. Ablation with highly reduced mechanical load can be achieved by moving to short pulse durations in the picosecond time scale or shorter and by applying moderate fluences. Higher pulse energies - leading to higher energy deposition into the plasma - increase the significance of mechanical effects. As a consequence crack formation or spallations of material from adjacent areas may occur which drastically reduces the ablation

quality or may harm the functionality of the ablated structures. Ablation takes place in the breakdown volume whereas mechanical load in form of shock waves or cavitation effects propagate into adjacent regions. For this ablation regime the term “photodisruption” is widely used because of the mechanical impact affecting the material. Plasma-induced ablation without mechanical load by photodisruption is limited to a pulse length of approx. 500 ps. Longer pulses need higher energy densities to achieve breakdown ($E_{th} \sim \tau^{1/2}$) where at the threshold value already significant mechanical side effects are observed [73].

The time scales on which these effects occur are shown in figure 8. The formation of the electron plasma starts during the laser pulse and persists for a few nanoseconds. The generation of a shockwave during the plasma formation is associated with the expansion of the plasma.

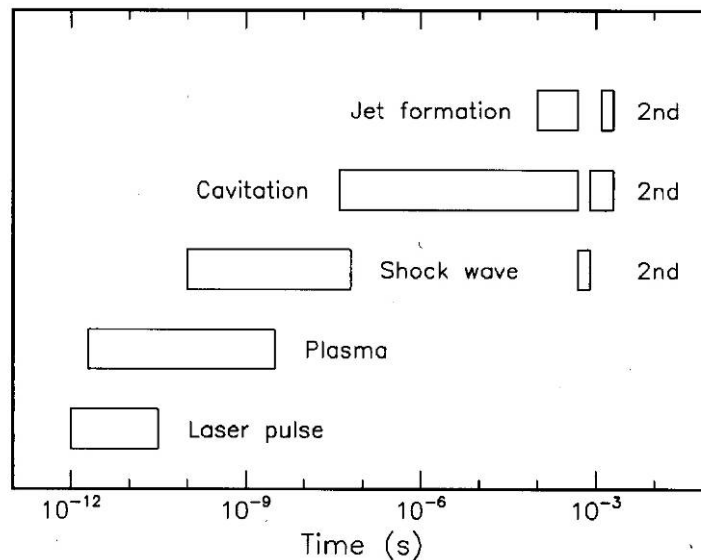


Figure 8: Time scale of physical effects induced by optical breakdown after an estimated laser pulse of 30 ps. Cavitation and jet formation may only occur in soft or liquid materials [73]

Cavitation occurs 50-150 ns after the laser pulse. It results from the formation and collapse of bubbles inside liquid or soft materials by vaporization of the focal volume due to the high plasma temperature. The bubble implodes again in a time scale less than one millisecond due to outer static pressure. The collapse of the cavitation bubble is accompanied by an increase of the pressure which may leads to a second occurrence of a shock wave.

Coulomb explosion

Compared to conducting materials the excitation of wide bandgap materials, either by linear absorption of high energetic photons or multiphoton processes, leads to the generation of electron-hole pairs and thus to a charging of the surface. By using moderate fluences coulomb explosion can occur from the surface region due to the high surface charging where an electrostatic repulsion between the surface positive ions follows the electron emission. The coulomb explosion process is schematically illustrated in figure 9. The occurrence of this process induced by ultrashort pulse laser irradiation has been shown by R. Stoian et al [94] where time of flight (TOF) measurements show equal momenta of positive ions that correspond to impulsive acceleration from a surface.

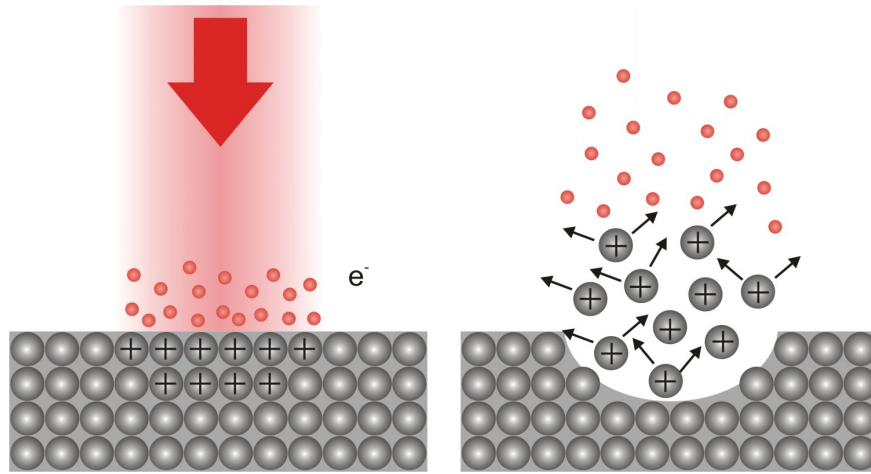


Figure 9: Schematic diagram showing the mechanism of material removal by coulomb explosion

The process occurs in a volume corresponding to the electron escape depth and as a consequence dominant coulomb explosion is characterized by low ablation rates. It has not been identified for semiconductor or metallic materials due to the fast charge neutralization in the electron depletion zone. For laser pulses longer than a few ps as well as for high fluence values for sub-ps pulses a thermal contribution to the ablation process is assumed.

Ultrafast melting, Phase explosion

In laser ablation of dielectric materials removal takes place after optical breakdown and the formation of a plasma. In case of semiconductors or metals, which are more or less linearly absorbing, energy coupling into the bulk is much more efficient and ablation is of thermal nature. Compared to pulses in the nanosecond time scale, heat conduction is strongly reduced by employing pico- and femtosecond pulse durations. The ablation is localized and

the heat affected zone is small or even avoided characterizing the overall process as “nonthermal” [21]. In case of femtosecond pulse duration the fluence absorbed by the material lead to different effects. When employing an intensity below the threshold for ablation or melting, the hot carriers relax via scattering and transfer most of the absorbed energy to the lattice on a picosecond time scale. By further increasing of the fluence the lattice may reaches the melting temperature and nucleation of the liquid phase takes place at the sample surface. At this fluence regime, which is still underneath the ablation value, the melting process is strictly thermal [28]. At higher fluences there is a change of the character of the transformation from solid to liquid. The excitation of a dense electron-hole plasma occurs leading to a destabilization of the lattice where the material melts on a sub-picosecond time scale. At this regime the process of melting is considered as ultrafast and nonthermal [85] due to the short time scale of the phase transition which can not be explained by classical thermal melting. By exceeding the threshold for ablation the transport of particles from the surface starts induced either by evaporation or boiling.

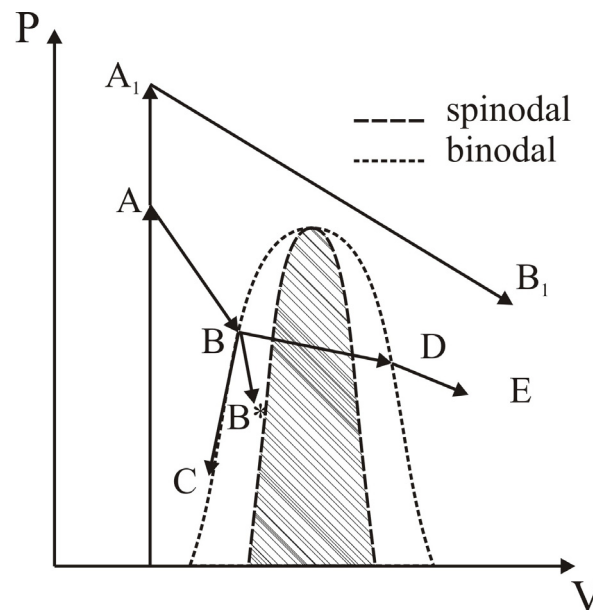


Figure 10: Thermodynamic pathway during ablation schematically outlined in a P - V diagram of a material

The process of ablation after irradiation of the sample can be shown in a P - V -diagram where the thermodynamic pathway is schematically outlined in figure 10.

The left and the right hand side of the diagram correspond to the liquid and the gas phase of the material, respectively. The binodal margins the metastable area where the material in equilibrium is composed by an inhomogeneous mixture of the two phases. Within this area

the spinodal represents the change from the meta- to the unstable phase and the system enters a region where a small perturbation in composition leads to a decrease in energy and thus spontaneous growth of the perturbation. The phase separation process is known as spinodal decomposition.

After irradiation of a semiconductor or a metal by a femtosecond laser pulse heating occurs at a constant density and the material is pushed to extremely high temperatures and pressures, initially very far from the metastable and unstable liquid regions. It can be regarded as an isochoric process and as a vertical transition in the P-V diagram (points A, A₁). The pressure is then released within several picoseconds through mechanical expansion of the material (adiabatic cooling) while the material remains in the liquid state (A→B). If significant heat diffusion exists, the liquid tends to cool along the binodal and to remain in the liquid state (B→C). If crossing of the binodal occurs the material tends to homogeneously nucleate the gas phase (B→B*). The competition of these two processes, nucleation of the gas phase and cooling, determines the onset of ablation by evaporation.

Finally, ablation is caused by phase explosion inside the metastable liquid region (B→D) and the material transforms into a gas, which can either be composed of single atoms or clusters (D→E).

If the fluence is high enough the material is heated to a point (A₁) where the subsequent adiabatic expansion takes place without entering the two-phase area.

Shockwave generation

Compared to acoustic waves, which travel through media at the speed of sound causing continuous pressure changes, shockwaves are initiated by a high pressure gradient leading to a shock wave front moving at supersonic speed. The high pressure amplitude causes a temperature rise (fall) at the areas with the highest (lowest) pressure leading to different velocities of the wave crest and wave trough, respectively. This leads to a deformation of the wave form from sinusoidal to sawtooth-like. These shock wave fronts cause discontinuous changes of pressure and temperature.

By inducing optical breakdown, a fast increase of plasma temperature occurs due to the kinetic energy of the excited free electrons. These electrons diffuse into the surrounding material. The motion of ions due to this electron migration results in a shock wave. Initially, the shockwave propagates at hypersonic speed (up to 5000 m/s) and then slows down to the speed of sound. To describe the propagation of the shock wave and the pressure gradient of a shock front, a slab of material is considered exhibiting a cross-section of A_0 . This area is passed through by a shock front with a velocity of u_s . The geometry of the shock wave propagation is schematically outlined in figure 11.

$$u_s = \frac{dx_s}{dt} \quad \text{Equ. 15}$$

The shock front leads to an increase of the local pressure and the density from p_0 to p_1 and from ρ_0 to ρ_1 , respectively.

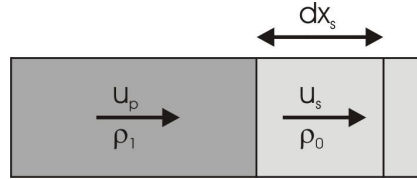


Figure 11: Schematic drawing of the propagation of a shock wave through a slab of material [73]

In calculating the shock wave propagation the conservation of mass as well as the conservation of momentum has to be fulfilled. Particles following from the left side move at the speed of u_p . The mass $(\rho_1 - \rho_0)A_0 dx_s$ is provided in a time interval dt by particles following at the speed of u_p from the zone with the higher density of ρ_1 leading to the expression $u_p \rho_1 A_0 dt = (\rho_1 - \rho_0) A_0 dx_s$. With equation 15 the velocity of the particles is given by

$$u_p = \frac{\rho_1 - \rho_0}{\rho_1} u_s \quad \text{Equ. 16}$$

In addition to the conservation of mass, the conservation of momentum has to be fulfilled. The momentum of a mass $A_0 \rho_1 dx_s$ moving at a speed of u_p is given by $A_0 \rho_1 u_p dx_s$. This momentum is provided by two means given by

$$A_0 \rho_1 u_p dx_s = A_0 \rho_1 u_p^2 dt + A_0 (p_1 - p_0) dt \quad \text{Equ. 17}$$

where the first term on the right side is the mass $A_0 \rho_1 u_p dt$ at the speed of u_p and the second term is the momentum induced by the mechanical force $A_0 (p_1 - p_0)$ during the time interval dt . With inserting equation 16 into 17 the pressure increase is given by

$$p_1 - p_0 = \rho_0 u_p u_s$$

Equ. 18

An empirical relationship between the shock speed and particle speed was first determined by M.H. Rice and J.M. Walsh [76]. The particle as well as the shock speed in water with respect to the shock wave pressure is outlined in figure 12.

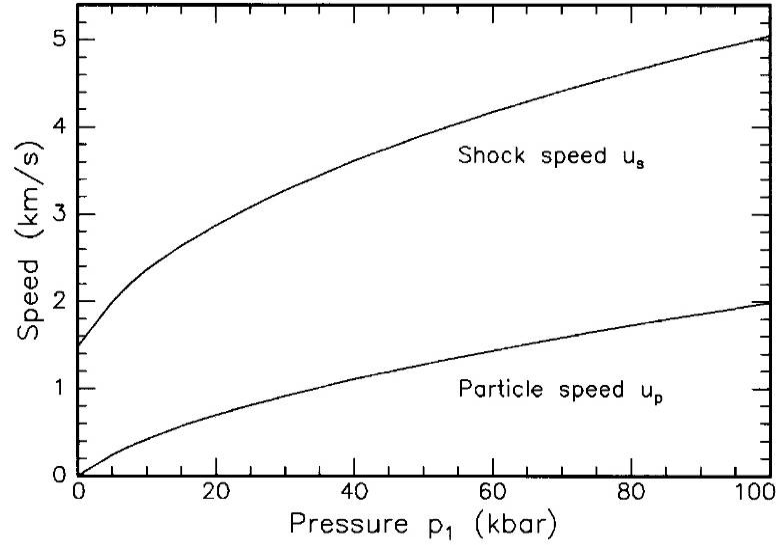


Figure 12: Shock and particle velocity versus shock wave pressure in water [73]

The shockwave pressure is usually very difficult to determine. The calculations shown in figure 12 can be used to derive the shockwave pressure as a function of the shock speed. Resulting values of the shockwave pressure versus distance for a pulse duration of 6 ns and 30 ps, respectively, are shown in figure 13.

For pulse durations of 20 ps and 6 ns at comparable intensities the shock pressures in water at the region of optical breakdown was calculated to be 17 and 21 kbar, respectively. In case of shorter pulse durations the decay of the pressure is much steeper with a shock wave dimension of just 3 microns, compared to the nanosecond results showing a width of approx. 10 microns. By estimating the energies contained in the shock waves it turns out that the shock waves from ultrashort pulses are weaker than those induced by longer pulses exhibiting comparable peak pressures. The energy contained in a shockwave can be approximated by

$$E_s \approx (p_1 - p_0) A_s \Delta r$$

with the shock wave surface area A_s and the shock wave width Δr . Vogel et al. [8] observed that the width of shock waves as well as the the surface area is smaller in the case of picosecond pulses compared to pulse widths in the nanosecond time scale.

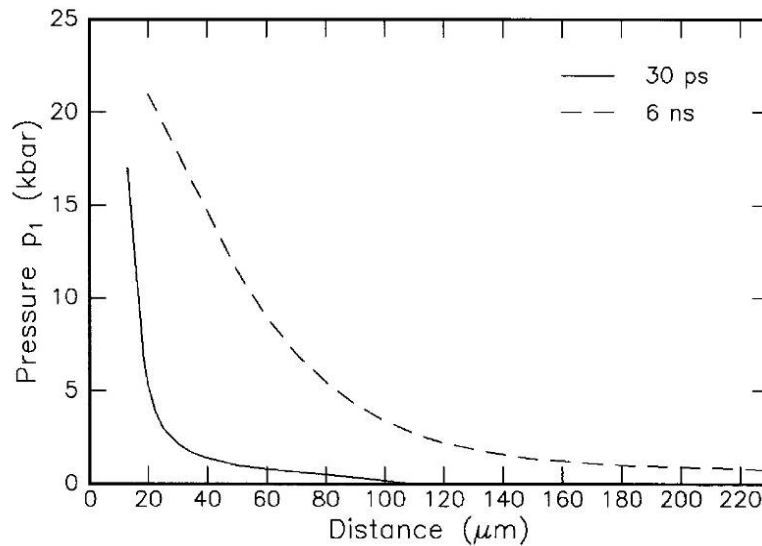


Figure 13: Laser induced shock wave pressure versus distance from the centre of emission after optical breakdown in water. The values are calculated for pulses with a duration of 30 ps (50 μ J pulse energy) and 6 ns at 1 mJ, respectively [73]

Simulations by M.D. Perry et al. [75] results in a shock wave exhibiting an amplitude of up to 12 Mbar for a 500 fs laser pulse at an intensity of $5 \cdot 10^{14}$ W/cm². The calculations were made for fused silica, irradiated with ultrashort pulses at a wavelength of 1053 nm. The pressure drops to a few kbar within less than one micron. The sharp decline of the pressure accompanied by the minimal heat transport into the bulk enables material processing with high precision and minimal heat or shock effected zone beyond approx. one micron of the machined area.

Chapter 3: Properties of Semiconductors and dielectrics

The target materials used in this work are predominantly semiconductors (Si) and especially wide-bandgap semiconductors (SiC, SrTiO₃).

In the case of Si and SiC an atom is surrounded by four next neighbours in a tetrahedral arrangement. It crystallizes either as diamond structure (e.g. Ge, Si) or as zinc blende in the case of III-V-semiconductors (e.g. GaAs).

The periodic arrangement of the atoms due to the crystal structure leads to the grouping of energy states into binding and non-binding energy bands. The probability of an electron to occupy a quantum state is given by the Fermi-Dirac-distribution which takes into regard the Pauli principle into

$$f(E) = \frac{1}{e^{(E-E_F)/k_B T} + 1} \quad \text{Equ. 19}$$

where E_F is the Fermi level and k_B the Boltzmann constant [30].

Semiconductors are defined as solids where the uppermost band of occupied electron energy states, the valence band, is completely full at absolute zero. Between this valence band and the so-called conduction band semiconductors exhibit a zone without energy states, the band gap, in contrast to metals where at absolute zero the conduction band is partially filled. For semiconductors the band gap is typically in the range of approx 1 eV (1240 nm). For wide band gap semiconductors which are predominantly used in this work the band gap is in the range of 2-3 eV (620-414 nm). The Fermi level lies in this forbidden zone.

In figure 14 the band structure and the optical transitions is shown schematically for a direct and an indirect semiconductor, respectively.

If the energy of a photon exceeds the band gap an excitation of electrons into the conduction band is possible. Due to the negligible photon momentum compared to that of an electron the transition occurs for constant values of the wave vector. Indirect interband transitions happen with less probability because an additional phonon has to be involved. This is also valid for the reverse transition, where the electron is transferred from the conduction band back into the valence band which is outlined in figure 14b.

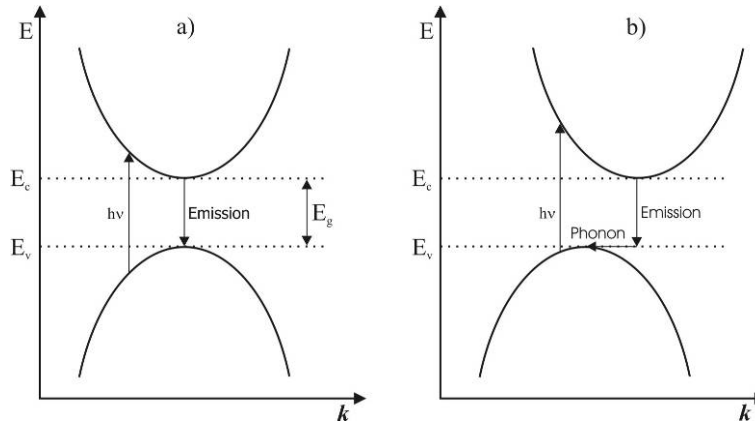


Figure 14: Band structure and optical transitions of a direct (a) and an indirect semiconductor (b)

The radiative lifetime of the excited states is in the range of ns. For high excitation rates with an electron density of approx. 10^{18} cm^{-3} or higher, Auger-recombination becomes important where the energy of the excited electron is transferred to another electron in the conduction band which is lifted to a higher energy state.

For photon energies lower than the band gap, linear absorption is negligible but absorption by free carriers, the formation of electron-hole pairs (excitons) or absorption by phonons may occur at these energies. For high intensities two- or multi-photon absorption processes may play a role in ultrashort pulse laser ablation for pulse durations in the femto- or picosecond time scale.

Once electrons are excited into the conduction band, the absorption by free carriers plays an important role in light-material interactions. Free electrons in a material act as a plasma. Derived from the Drude model the dielectric constant can be written as

$$\varepsilon = \varepsilon' + j\varepsilon'' = 1 - \frac{\omega_p^2 \tau_e^2}{1 + \omega^2 \tau_e^2} + j \frac{\omega_p^2 \tau_e}{\omega(1 + \omega^2 \tau_e^2)} \quad \text{Equ. 20}$$

where τ_e is the mean time of collisions between electrons and ω_p is the plasma frequency.

It is defined as

$$\omega_p^2 := \frac{N_e e^2}{\varepsilon_0 m_e} \quad \text{Equ. 21}$$

where N_e is the electron density, e is the elementary charge, ε_0 is the permittivity of free space and m_e is the electron mass. The plasma frequency of metals is in the deep UV whereas for semiconductors it is in the infrared spectra. Frequencies below the plasma frequency exhibit a high imaginary part of the refractive index leading to strong absorption and a high reflectivity.

The corresponding absorption coefficient is valid for low density plasmas. It is given by

$$\alpha_{fc} \approx \frac{\omega_p^2}{\tau_e c \omega^2} \propto \lambda^2. \quad \text{Equ. 22}$$

For frequencies higher than the plasma frequency, the imaginary part of the dielectric constant approaches zero leading to very low absorption. With the approximations

$$\varepsilon' \approx 1 - \frac{\omega_p^2}{\omega^2} \quad \text{and} \quad \varepsilon'' \approx 0. \quad \text{Equ. 23}$$

the refractive index is then given by

$$n = \sqrt{\varepsilon} \approx 1 - \frac{\omega_p^2}{2\omega^2}. \quad \text{Equ. 24}$$

Above the plasma frequency the material is therefore transparent and the refractive index is below one.

Silicon, single crystal

Silicon is an indirect semiconductor where the direct and indirect band gap is 2.5 and 1.12 eV corresponding to wavelengths of 496 and 1107 nm, respectively. In figure 15 the absorption coefficient of Si is presented as a function of the wavelength. The laser lines of the fundamental and the second harmonic of the Nd:Vanadate laser are highlighted. The fundamental wavelength (1064 nm) is in the range of the indirect band gap.

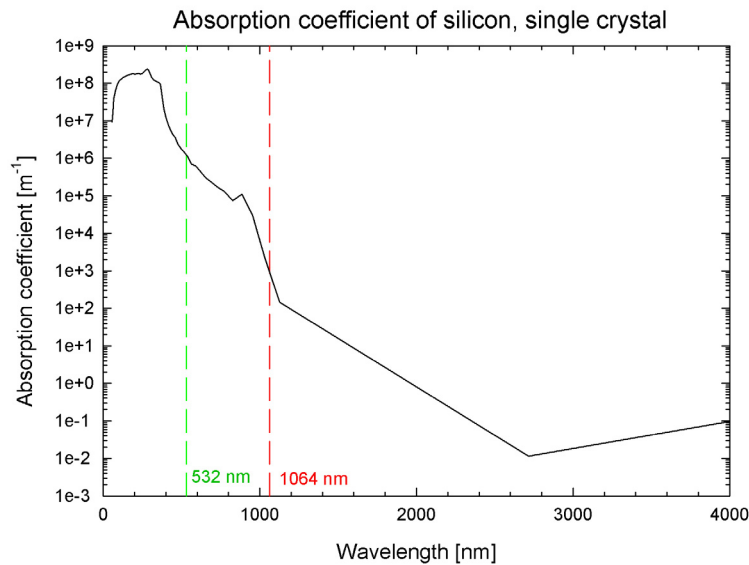


Figure 15: The absorption coefficient [20] of Si highlighting the values for the fundamental and the second harmonic of the Nd:Van laser wavelength. The linear absorption of the fundamental is negligible. The absorption has to rely on two-photon transitions for this wavelength

Strontium titanate

Strontium titanate exhibits a cubic perovskite structure at room temperature which is typical for ABO_3 compounds. It has a bandgap of 3.2 eV, corresponding to a wavelength of 388 nm. A specific property of SrTiO_3 is that it transforms into the tetragonal structure at temperatures less than 105K, which is due to the rotation of the titanium-octahedron. It is ferroelectric and also exhibits a very large dielectric constant and is used in high-voltage capacitors. At very low temperatures, it exhibits piezoelectric and superconductive properties. In figure 16 the absorption coefficient of SrTiO_3 at room temperature is shown. Strontium titanate is considered extremely brittle and has the tendency of building cracked surfaces when treated with laser radiation. The most important properties of SrTiO_3 and the materials used during this work are outlined in appendix 2.

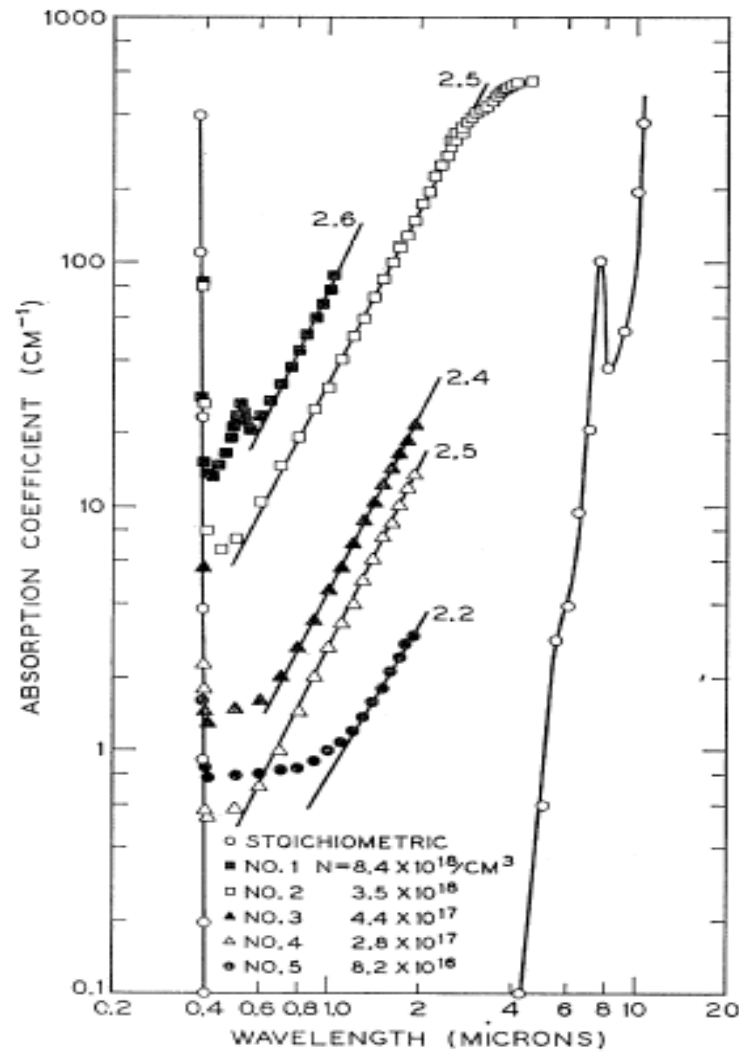


Figure 16: Absorption coefficient of SrTiO_3 at room temperature.

Silicon carbide

Silicon carbide is classified as a wide bandgap semiconductor. The stoichiometric ratio of silicon and carbon is 1:1 and each atom is bonded to four atoms of the respective other element in tetrahedral configuration.

One of the most specific properties of SiC is its polytypism, which is the existence of different stacking orders of the basic structural element layers. The basic building block is a hexagonal bilayer with alternating site occupation in which each element is positioned in one of the two sublayers. SiC in cubic crystal structure is often called β -SiC whereas all other configurations (hexagonal, rhombohedral) are categorized as α -SiC. For a more detailed description, the polytype is generally indicated by the number of bilayers within the unit cell and a letter indicating the true lattice symmetry (see figure 17).

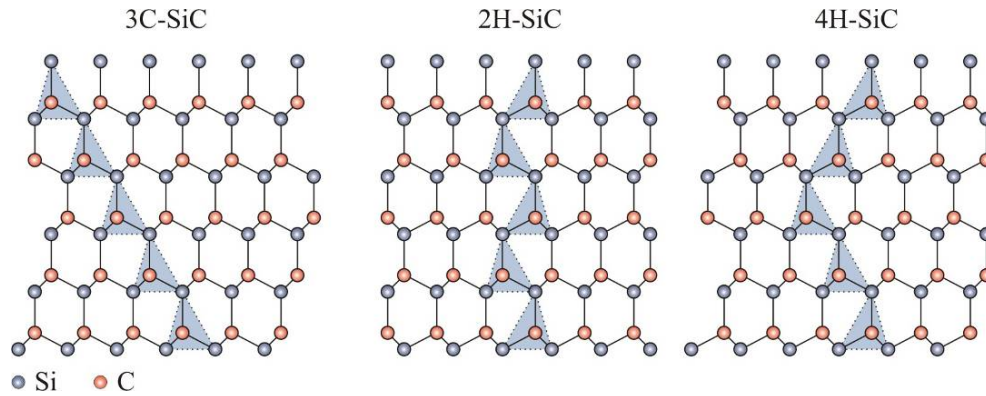


Figure 17: Stacking order of three different SiC polytypes. It is indicated by the number of bilayers within the unit cell and a letter indicating the lattice symmetry

Correspondingly, the cubic structure with 3 bilayers per unit cell is called 3C-SiC. The commonly used SiC polytypes are the hexagonal 4H- and the 6H-SiC. The wafer used in this work was cubic 3C-SiC, exhibiting a zinc blende structure.

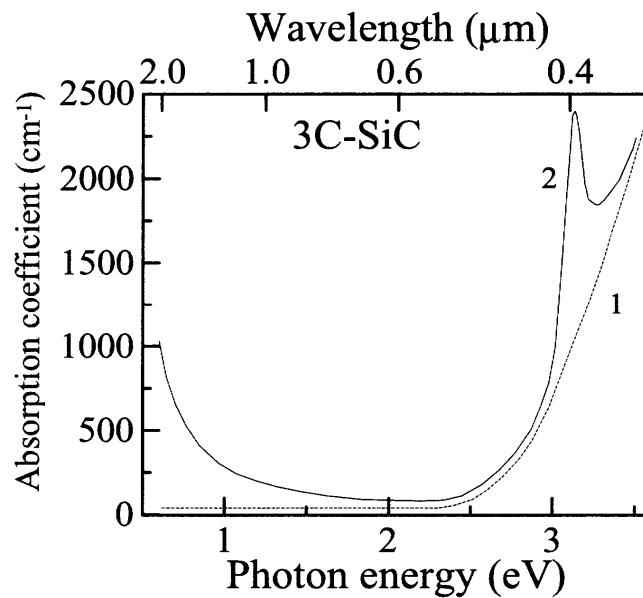


Figure 18: The absorption coefficient of cubic silicon carbide vs. photon energy for different electron concentrations $T=300\text{ K}$ (1:relatively pure crystal, 2: $N_d = 1019\text{ cm}^{-3}$ [70])

Figure 18 shows the absorption coefficient of cubic silicon carbide for photon energies relevant in this work. At high photon energies corresponding to wavelengths of the excimer lasers used there were no data on absorption coefficients available.

Chapter 4: Experimental

4.1. Laser Systems

The big variety of laser parameters applied during this work with wavelengths ranging from the IR down to the UV and pulse durations down to femtoseconds have been provided by various laser systems. The systems as well as the different optical setups needed for the experiments are described in this chapter.

4.1.1 Excimer lasers

The UV lasers used in this work are excimer lasers emitting light at a wavelength of 193 (ArF) and 248 nm (KrF), respectively, at pulse durations in the nanosecond time regime.

For comparative studies of laser ablation with emphasis on the pulse duration another UV laser was used emitting at 248 nm with pulse durations in the femtosecond time regime. The system is based on the amplification of the frequency doubled output of a subpicosecond dye laser system. The laser can be operated at pulse durations of 150 fs, 500 fs and 5 ps providing 10 mJ of pulse energy at a maximum repetition rate of 10 Hz. As an additional option the subpicosecond-output of the dye-laser provides pulses at a wavelength of 496 nm at the same repetition rate.

The beam profile of an excimer laser exhibits nearly a Gaussian shape in y-direction and a tophat profile in x-direction. The beam size at the laser exit is relatively large, approx. 2 centimeters by 5 centimeters. Mainly due to the poor spatial coherence of excimer lasers, the field in the focal plane exhibits an intensity distribution which is not satisfying for micromaching applications.

One procedure to improve the beam profile is to use a homogenizer. The optics in this case consists of two crossed arrays of cylindrical lenses that divide the incident laser beam into separated rays. These are combined by a subsequent spherical lens into a tophat beam profile [14]. A schematical setup is shown in figure 19. To allow fluences high enough for ablation an additional lens is used for imaging the homogenized plane. By placing a mask in the homogenized plane patterns can be ablated over a relatively big area.

In this work the pattern transfer was of minor interest. To study relevant ablation parameters like the ablation threshold an easier setup can be used by selecting, with an aperture, a nearly homogeneous area in the center of the beam. With a focusing lens, a circular laser spot with a constant intensity profile is ablated.

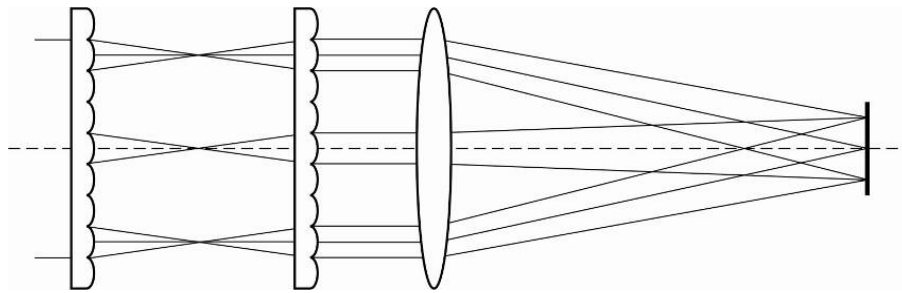


Figure 19: Optical path for micromachining purposes with an excimer laser. An array of cylindrical lenses is used to achieve a constant intensity distribution in the homogenized plane.

4.1.2 Solid-State lasers

Most lasers used in this work are diode pumped solid-state lasers in a wide range of pulse durations.

The basic principle of ultrashort pulse generation is the introduction of a saturable loss mechanism into the cavity. Common methods are Kerr-lens modelocking or modelocking by a semiconductor saturable absorber mirror (SESAM).

The Kerr lensing principle (Titan sapphire laser) utilizes the nonlinear self-focusing effect of the laser material known as optical Kerr effect. An aperture is placed in the oscillator cavity operating as an intensity dependent loss. If the intensity of the pulse is high enough the lensing effect enables a passing through the aperture whereas low intensity light is partly blocked.

In case of SESAM modelocking a mirror with an intensity dependent absorption behavior is used in the resonator to obtain a self-amplitude modulation of the radiation. The reflectivity of the mirror is increased for higher intensities leading to an amplification of lower-loss coupled modes.

The generation of pulses in the nanosecond regime is done by Q-switching techniques where an additional loss is inserted into the laser cavity. Due to the high overall losses the laser is suppressed leading to the built up of a high inversion inducing a fast photon generation after switching off the gain. The pulse duration of approx. 10 ns is given by the time to release the inversion which happens within a few resonator round-trips. Q-switching can be realized by active or passive techniques where common methods are for example the use of a saturable absorber element in the cavity (passive) or by means of a pockels-cell (active) which can be externally controlled working in combination with a polarizer as an intracavity switchable loss. In table 1 a list of all laser systems used during this work is given.

Laser source	Type / medium	Wavelength	Pulse duration	Pulse energy	Rep. rate
<i>femto</i> REGEN	SSL / Yb:glass	1040 nm	300 fs	100 μ J	15 kHz
s-pulse	SSL / -	1026 nm	400 fs	100 μ J	10 kHz
	SSL / Ti:Sapphire	800 nm	30 fs		1 kHz
<i>pico</i> REGEN	SSL / Nd:Van	1064 nm	10 ps	320 μ J	5 kHz
LPF220	Excimer / ArF	193 nm	25 ns	250 mJ	200 Hz
LPX200	Excimer / KrF	248 nm	34 ns		
	dye-laser	248 nm	500 fs	10 mJ	10 Hz
Brilliant	SSL / Nd:YAG	1064 nm	5 ns		

Table 1: Laser systems and their key parameters applied during this work.

For the picosecond experiments a Nd:Vanadate (Nd:YVO₄) seed laser followed by a regenerative amplifier was used. The system operates at a center wavelength of 1064 nm. The maximum pulse energy is 300 μ J (@5kHz) and the repetition rate can be varied up to 10 kHz. The pulse duration of this system is 10 ps.

The femtosecond system was an Yb:Glass seed laser amplified by a regenerative amplifier similar to the ps system. An additional stretcher/compressor system was implemented to prevent damage of the components due to high peak intensities. The laser can be operated at repetition rates up to 15 kHz and the maximum pulse energy provided by the system was 100 μ J (@1 kHz). The pulse length was 300 fs, a duration where the pulse duration is not yet affected by dispersion effects due to the optics in the beam path.

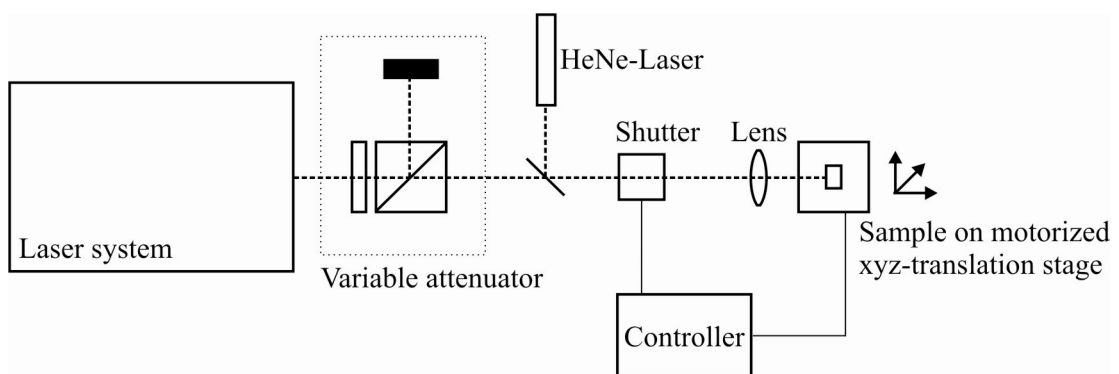


Figure 20: Setup used for direct structuring with a focussed beam. The sample was positioned on a 3-axis translation stage. The beam can be blanked by means of a electric mechanical shutter, operated by the motion controller of the motorized stage.

The Gaussian beam shape of solid-state lasers allows direct writing techniques by focusing the beam with a single lens or a microscope objective. The general setup used for most experiments is shown in figure 20. The combination of a rotatable half-wave plate and a polarizer allows the variable attenuation of the laser power. A HeNe laser collinear to the laser beam was used for the adjustment of the optics along the beam path and for positioning the beam focus on the sample surface.

4.2. Determination of the beam- and ablation parameters

For the analysis of the ablation process one of the basic requirements is the characterization of the beam profile within the ablation plane.

In the case of the experiments carried out with the excimer lasers a constant intensity over the whole laser spot was obtained by the optical setup used. In this fashion the fluence can be determined simply by calculating the ratio of the pulse energy and the illuminated area.

For lasers with a Gaussian beamshape the two-dimensional intensity profile can be determined by the use of a CCD- camera. This method has the disadvantage, that the CCD-chip is very sensitive and exhibits a very low saturation value. This leads to the need of a strong attenuation of the focused laser beam with the risk of distorting the original beam profile.

An alternative procedure to determine the intensity profile is the pinhole method where a micron size aperture is scanned across the laser beam. In this configuration, the detector measures the power of the beam over the aperture of the pinhole. The result is, similar to the one obtained with the CCD-camera, a two-dimensional array of the intensity. The resolution in this case is determined by the size of the pinhole. In this work, predominantly tightly focussed beams of a few microns diameter have been used which makes this method impractical. An easy and simple alternative is the measurement by the knife edge method, scanning the sharp edge of a razor blade across the laser beam. The setup of the knife edge method used to determine the beam diameter is shown in figure 21.

The transmitted power of the beam is measured by a detector. The disadvantage of the knife edge method is that it does not yield directly the shape of the intensity profile.

The experimental data is obtained by moving the razor blade in small increments across the beam. The resulting graph is shown in figure 21.

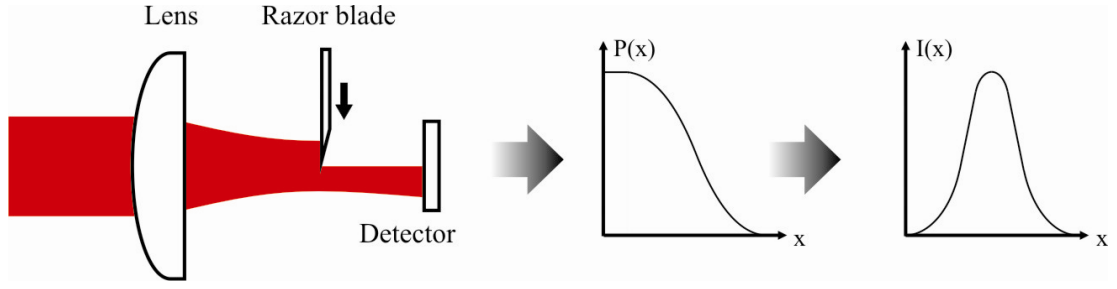


Figure 21: Setup of the knife edge method used to determine the $1/e^2$ diameter of the Gaussian beam shape in the ablation plane. The razor blade was fixed on a motorized translation stage with a resolution of 100 nm and an accuracy of 200 nm.

Assuming a Gaussian profile numerical differentiation (central differentiation) results in the beam diameter. To avoid inaccuracies due to distortions at the bottom of the profile, the FWHM-diameter was extracted out of the data where the $1/e^2$ -diameter is

$$d_{1/e^2}(z) = \sqrt{\frac{2}{\ln(2)}} d_{fwhm}. \quad \text{Equ. 25}$$

4.2.1 Fluence and intensity of the laser pulse

In laser machining it is common to characterize the radiation by the fluence, which is the local energy flow [J/cm²]. The fluence profile of a Gaussian beam is given by

$$\phi(r, z) = \phi_0 e^{-2r^2/w^2} \quad \text{Equ. 26}$$

where w is the beam radius. ϕ_0 is the maximum fluence in the center of the beam. The integration of equation 26 yields

$$E_{pulse} = \int_0^\infty \phi(r, 0) 2r\pi dr = \frac{\phi_0 \pi w^2}{2} \Rightarrow \phi_0 = \frac{2 E_{pulse}}{\pi w^2} \quad \text{Equ. 27}$$

The result is a simple equation connecting the pulse energy with the fluence. For laser pulses in the ultrashort time regime it may be more meaningful to give peak intensities

$$I = \frac{\phi_0}{\tau_p} = \frac{2 E_{pulse}}{\pi w^2 \tau_p}$$

Equ. 28

where τ_p is the pulse duration.

4.2.2 Threshold fluence

There are various methods to determine the ablation threshold fluence. For ablation experiments carried out in vacuum there is the possibility to detect ablated material with a mass spectrometer. The advantage of this method is its high sensitivity. The method can also be used universally to analyze the ablated products and the ablation process in general. Another method is the detection of acoustic waves resulting from the plasma expansion. This method requires a sufficient acoustic insulation of the setup.

A widely used method is to evaluate the ablated cavity. By plotting the crater depth versus the laser fluence the ablation threshold can be determined by extrapolating the depth to zero. For the ablation with pulses exhibiting a Gaussian beam shape a convenient method was presented by J.M. Liu [54], which has also been adopted in this work. The method allows the determination of the beam diameter and the ablation threshold from a plot of ablated area vs. pulse energy. When a material is exposed to a fluence above the ablation threshold, a circular zone of area $A_{abl} = r_{abl}^2 \pi$ is ablated (figure 22).

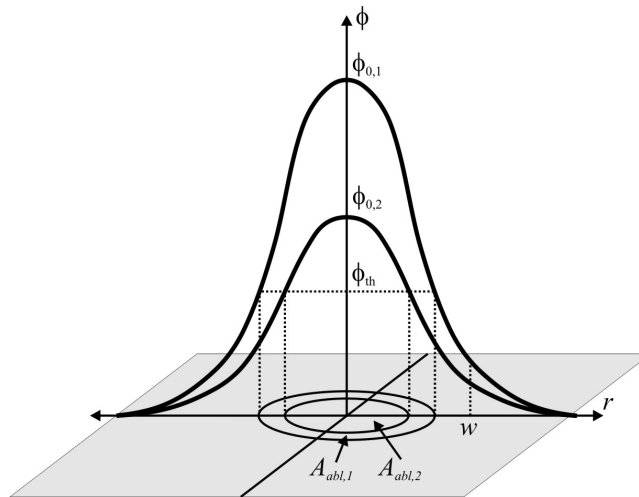


Figure 22: Schematic diagram on the dependence of the ablated spot area on the pulse energy to determine the beam diameter as well as the ablation threshold of the treated material by means of a Liu-plot

According to equation 26 the area A_{abl} can be calculated from

$$\phi_0 e^{-2r_{abl}^2/w^2} = \phi_0 e^{-2A_{abl}/A_L} = \phi_{th}, \quad \text{Equ. 29}$$

where $A_{abl} = r_{abl}^2\pi$ is the ablation area and $A_L = w^2\pi$ is the laser spot area. Therefore, the ablated area

$$A_{abl} = \frac{A_L}{2} (\ln(\phi_0) - \ln(\phi_{th})) \quad \text{Equ. 30}$$

is a linear function of the logarithm of the fluence. From a plot of A_{abl} vs. $\ln(\phi_0)$ we can immediately extract the threshold fluence as the interception of the extrapolated plot with the horizontal ($A_{abl} = 0$) axis. By the same token, the laser spot area A_L follows from the slope of the plot

$$A_L = \frac{2(A_{abl,2} - A_{abl,1})}{\ln(\phi_{0,2}) - \ln(\phi_{0,1})} = \frac{2(A_{abl,2} - A_{abl,1})}{\ln(E_{p,2}) - \ln(E_{p,1})} \quad \text{Equ. 31}$$

where E_p is the pulse energy and the indices 1 and 2 refer to different points on the plot.

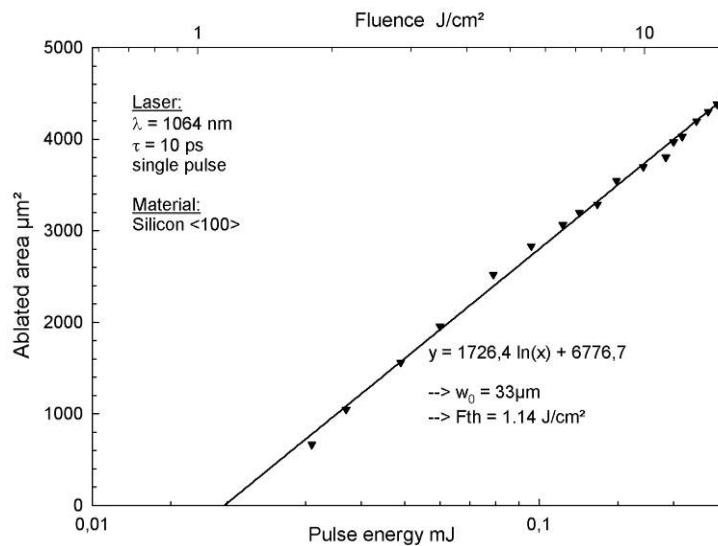


Figure 23: Liu-plot to determine the single pulse ablation threshold of silicon and the beam diameter in the ablation plane.

The advantage of this technique over the knife edge method is that the beam diameter and the ablation rate are measured with the sample itself. This allows reliable measurements of the parameters also in case of tightly focused laser beams. In addition, the method is suitable for thin films where other methods, for example the extrapolation of the crater depth, are not suitable. Measurements can be carried out easily by using a microscope whereas the crater depth has to be measured with a profilometer which requires sufficiently large hole diameters for reliable measurements.

4.2.3 Ablation rate

An important parameter for the efficiency of a process and its suitability for industrial use is the ablation rate or yield. It is given by the ablated depth or volume per laser pulse. The ablation rates in this work are in the range of a few hundreds of nanometers per pulse. To guarantee ablation rate measurements with a high accuracy the sample is treated with a train of pulses and the ablation rate is determined by the crater depth divided by the number of laser pulses. In some cases it is more suitable to determine the volume ablation rate instead of the depth. This can be necessary for example when the laser beam exhibits an inhomogeneous intensity profile.

The time needed to structure a pattern of a certain shape can then be estimated by calculating the laser pulses needed for the removal (volume or depth) of the material. This is valid for shallow cavities where the amount of material removed by each pulse is approximately constant. When applying more pulses the rate exhibits a strong variation. Especially in laser drilling the ablation rate is not constant. At a certain depth the drilling process shows a saturation effect where the ablation rate drops to values of one up to two orders of magnitude smaller [26]. This is a general phenomenon and can be explained by various mechanisms, one being the energy coupling into the material. The formation of a deep cavity during laser processing changes the area illuminated by the laser beam. The increase of the surface area can then lead to a remarkable reduction of the intensity and consequently of the ablation rate. When the underlying ablation mechanism is of thermal nature the heat conduction is an additional factor decreasing the ablation rate. While a one-dimensional description of heat conduction can be used in case of minimal lateral variations of the surface topography, a three-dimensional heat conduction has to be considered in case of strongly concave surfaces. Depending on the shape the material can conduct heat slower or faster than on flat surfaces because of a more efficient heat diffusion or accumulation [5].

An additional effect decreasing the ablation rate is absorption and scattering by the ablated products.

Chapter 5: Influence of the pulse duration in ablation of 3C-SiC and SrTiO₃

In microtechnology silicon is still one of the most important materials and methods for structuring silicon are well established and sophisticated. However, technological important materials like silicon carbide are convincing due to their outstanding material properties but, compared to silicon, structuring of SiC is rather demanding. Also perovskites like SrTiO₃ are of great practical interest for modern electronic devices and as substrates in thin film technology. Earlier studies ([17],[25]), have shown that laser machining of SrTiO₃ with nanosecond lasers suffers from the tendency of this material to form cracked surfaces (figure 30). In this chapter the possibility of laser processing cubic silicon carbide and SrTiO₃ has been studied with different laser sources providing wavelengths from the UV to the IR as well as pulse durations ranging from ns down to the femtosecond time scale.

The electrical properties from SrTiO₃ vary from insulating to semiconducting and even metall-like behaviour. It is paraelectric and maintains the perovskite crystal structure over a wide temperature range. Its large dielectric constant and high dielectric breakdown field makes SrTiO₃ a potential candidate for storage capacitor cells in next-generation dynamic random access memories [63], and its large dielectric nonlinearity at cryogenic temperatures is a desirable property for various applications such as tunable filters and phased array antennas [7]. Some important industrial properties of SrTiO₃ and SiC have been outlined in Appendix 2.

As mentioned in chapter 3 silicon carbide exists in several polytypes. Thanks to its outstanding diamond-like properties, silicon carbide (SiC) has long been recognized as an excellent material for high power, high frequency and high temperature electronics. It has a wider band-gap, higher breakdown field, higher thermal conductivity and higher saturation velocity than silicon. Because of its high thermal conductivity, good chemical resistance and mechanical hardness SiC is now receiving added attention for its potential in microelectromechanical systems (MEMS) [10],[72],[86], where Si is currently the leading material. Using SiC allows to expand the application of MEM devices to harsh temperature, wear, chemical and radiation environments.

Most work on single-crystal oxides (MgO [56],[68],[98] and SrTiO₃ [17],[25],[35]) found in literature has been carried out with lasers emitting in the UV, with pulse durations in the nanosecond timescale. Ablation studies with ultrafast (femtosecond) UV lasers have been carried out on various materials, predominantly on polymers [65],[24],[1],[78] but also on

dielectric materials [43],[44] and semiconductors [84]. The potential of these systems for microstructuring, even in the submicron range, has been shown by Chen and co-workers [59],[52],[60]. As with ultrafast IR-lasers [75], the non-thermal mechanism of ultrafast ablation has been shown to improve the ablation process considerably.

Microstructuring of SiC is difficult because of its chemical inertness. There are no known wet etchants that can be used to machine bulk device structures from SiC substrates at room temperature. Sophisticated techniques such as electrochemical etching [103],[113], high intensity plasma or reactive ion etching (RIE) have been employed for structuring SiC [33], [53], [81], [82]. Laser ablation is therefore an attractive alternative for microstructuring SiC. Recently, studies have been carried out with infrared pulses in the nanosecond [101] and in the femtosecond time regime [115], [116]. Good ablation results have been achieved with ultraviolet and multiwavelength excitation [45],[46],[92].

5.1.1 Experimental

Most experiments in bulk SiC have been carried out in hexagonal 6H-SiC. The sample used in our work was polished single crystal 3C-SiC. Its cubic (zincblende) structure entails significantly different material parameters. In case of SrTiO₃ the samples were 1 mm thick bulk SrTiO₃ <100>.

The UV lasers used are two Excimer lasers (LPX 200 and LPF220, Lambda Physik), one with a pulse duration of 34 ns at a wavelength of 248 nm (KrF) and the other with a pulse duration of 25 ns at a wavelength of 193 nm (ArF) and a distributed feedback dye laser system pumped and amplified by a KrF excimer laser, yielding 500 fs pulses at 248 nm, respectively. For experiments in the IR diode pumped solid state lasers were used emitting pulses at a wavelength of 1040 and 1026 nm with a pulse duration of 300 (*femto*REGEN, High Q Laser) and 400 fs (s-pulse, Amplitude), respectively.

In the nanosecond excimer laser experiments, a (circular) iris aperture was placed in the beam path and imaged by means of a single lens with a focal length of 60 mm. The sample, which was fixed on a xyz-stage, was positioned in the image plane of this lens system. For the UV-femtosecond experiments, the sample was positioned closer to the lens to avoid undesired energy losses and distortions of the energy distribution due to electrical breakdown in air in the focal plane.

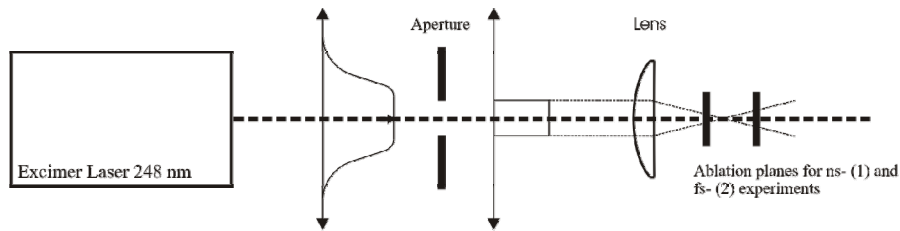


Figure 24: Optical Setup used for the determination of the ablation threshold and the ablation rate for experiments with the excimer lasers and the dye laser, respectively. For ns pulse durations the sample was placed in the conjugated plane of the aperture (1), for the UV-femtosecond pulses the sample was positioned closer to the lens (2) due to breakdown in air in the focal plane.

In both cases the intensity of the beam was adjusted with a reflecting variable attenuator and all experiments were done under ambient conditions.

For the experiments with the solid state lasers the beam (Gaussian beam shape) was directly focused onto the surface of the sample. The diameter of the beam was measured in the ablation plane with a knife edge permitting the determination of the laser fluence with a high accuracy.

The ablated cavities were measured out with a Tencor Alphastep to determine the ablation rate. Scanning electron microscopy was used to image the surface morphology of the ablated cavity and its surroundings.

The focal intensity distribution of the UV-femtosecond laser beam exhibited concentric fringes which lead to an uneven ablated structure at the sample. This makes it more difficult to derive the ablation parameters. To compare the results, the volume instead of the ablated depth of the cavities was determined for the nanosecond and the femtosecond experiments. Assuming a rotational symmetry of the cavity, the volume was calculated on the base of a radial cross section of the ablated area provided by the Alphastep profilometer (see figure 25).

From these data, an effective ablation rate (nm/pulse) was extracted. Each cavity was treated with a train of 100 pulses at a repetition rate of 4 Hz.

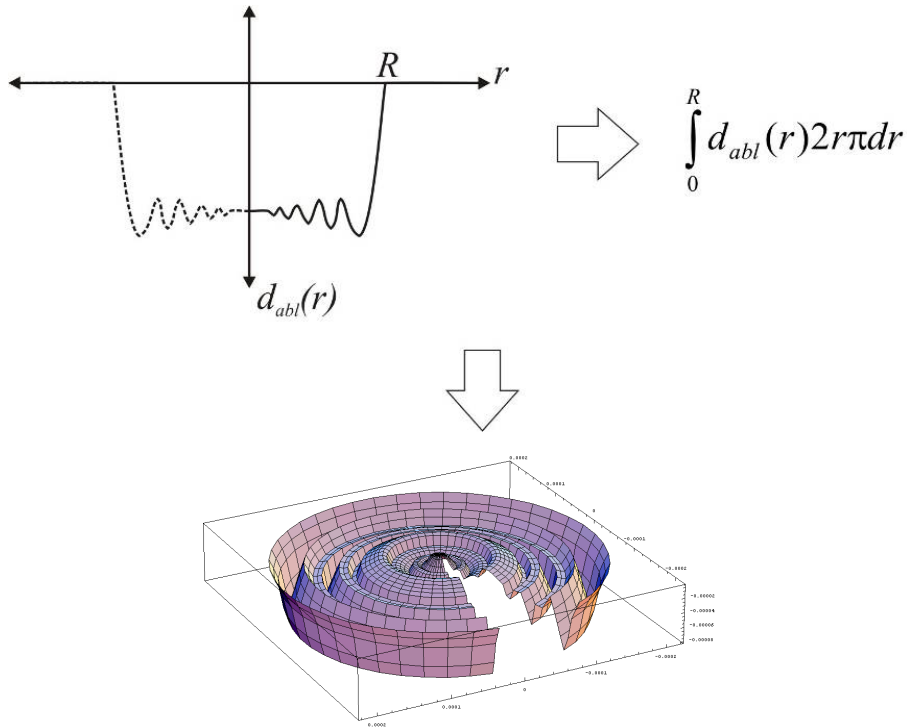


Figure 25: Cavity ablated with a pulse duration of 500 fs at a wavelength of 248 nm. The cross-section measured by a profilometer was transferred to Matlab[®] to calculate the ablated volume.

5.1.2 Results

Figure 26 shows a direct comparison between nanosecond- and femtosecond ablation yield of SrTiO₃. In the case of ablation with nanosecond pulses the ablation rate increases linearly with the pulse energy and number of laser shots. For femtosecond pulses, the systematic scatter of the pulse energy does not allow to extract such a dependence unambiguously, but a linear behavior seems to dominate in the measured range of pulse energies. Obviously, however, the ablation rate is significantly higher for the femtosecond ablation. While the above-bandgap photon energy permits ablation by a single photon process, there is still a large benefit from using sub-picosecond pulses because of the reduced thermal diffusion during the exposure time.

The ablation thresholds have been determined for multi pulse and single pulse treatment to be $\phi_{s,ns} = 0,6 \text{ J/cm}^2$ for a single pulse and $\phi_{m,ns} = 0,3 \text{ J/cm}^2$ for multi-pulse ablation in the case of a pulse duration of 34 ns. The difference in the threshold values for single and multipulse ablation has been observed by other researchers [13] and is explained by accumulated

microscopic damage in the exposed areas, which leads to ablation after a certain number of pulses.

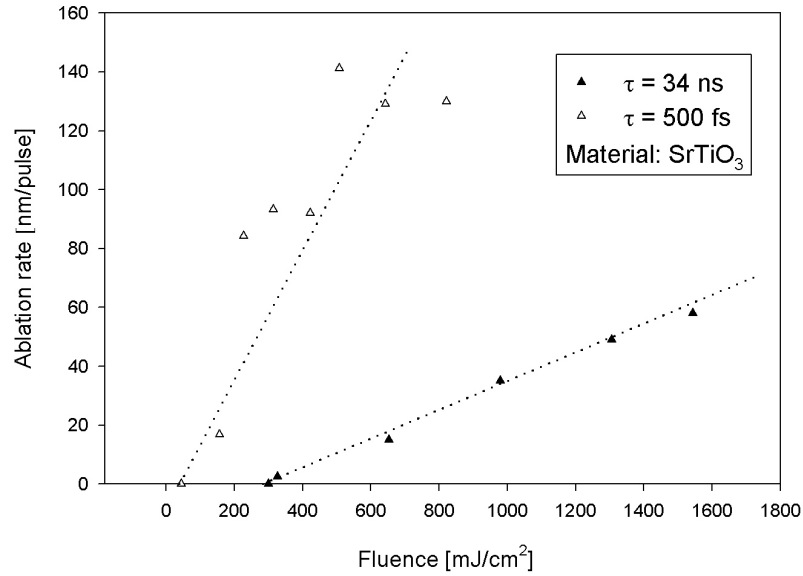


Figure 26: Comparison of the ablation rate of SrTiO_3 for a wavelength of 248 nm at pulse durations of 34 ns and 500 fs, respectively. The dotted lines are a guide for the eye [P11]

The threshold fluences for the pulses in the femtosecond time regime are $\phi_{s,fs} = 0.15 \text{ J/cm}^2$ and $\phi_{m,fs} = 0.044 \text{ J/cm}^2$, respectively. For multi pulse ablation the value is approximately one order of magnitude lower compared to the nanosecond results.

The much lower threshold fluence and enhanced ablation yield are due the fact that for sub-picosecond UV pulses the laser energy is deposited within the optical penetration depth of approx. 13 nm ($n = 2.085 + j1.474$ at 245 nm wavelength [23]) while it spreads, via thermal diffusion, into a much deeper volume during nanosecond irradiation (350 nm at our pulse duration [100]).

To determine ablation rates and thresholds of 3C-SiC, cavities were ablated with 100, 50 and with single shots for each adjusted laser energy. In case of the ns experiments the laser beam profile was very smooth. Experiments were carried out with fluences ranging from 0.06 up to 10 J/cm^2 . Figure 27 shows the ablation rate of 3C-SiC for three different sets of laser parameters, the multi and single pulse ablation thresholds of 3C-SiC as well as SrTiO_3 are outlined in table 2.

Due to the linear absorption mechanism underlying the ablation with lasers emitting in the UV, a linear dependence of the ablation rate on the fluence is again observed in case of 3C-SiC.

Table 2: Ablation thresholds for multi and single pulse experiments for various sets of laser parameters

Laser Parameters		Ablation threshold (mJcm ⁻²)			
		3C-SiC		SrTiO ₃	
Wavelength / photon energy	Pulse length	Single Pulse	Multi Pulse	Single Pulse	Multi Pulse
248 nm / 5 eV	500 fs	260	130	150	44
248 nm / 5 eV	34 ns	1500	850	600	300
1026 nm / 1.2 eV	400 fs	550 [71]	60	-	-

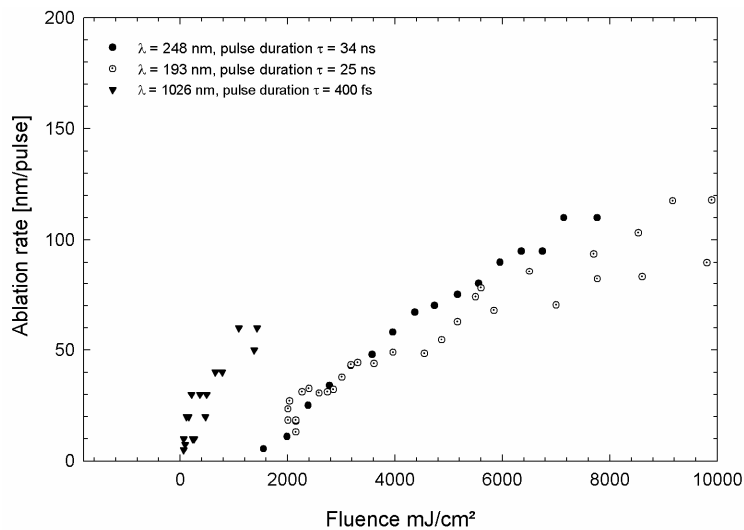


Figure 27: Ablation rate of 3C-SiC for three different sets of laser parameters [P7]

3C-SiC is a wide band gap semiconductor with an indirect band gap. Its minimum indirect band gap is 2.39 eV, corresponding to a wavelength of 519 nm. Its direct band gap of 5.3 eV [83] (6 eV [93]) is situated between the ArF (6.4 eV) and the KrF (5 eV) photon energy. To our knowledge there is no data available of absorption coefficients of 3C-SiC for UV-photon energies of 6.4 eV but it can be assumed that the absorption of 193 nm radiation is higher than the one at 248 nm. Somewhat surprisingly, however, the ablation yields of both ns-excimer lines turn out to be comparable.

The ablation yield achieved with femtosecond pulses is, equally to the results with SrTiO_3 , significantly higher and the threshold lower than the one obtained by the excimer lasers (see table 2). Since the linear absorption at a wavelength of 1026 nm (1.2 eV) is negligible, the absorption mechanism has to rely on two-photon transitions.

When comparing different laser systems for micromachining one has to keep in mind that data of the ablation rates as shown in figure 27 cannot be interpreted without further considerations because of the different performance parameters of the various laser systems. Excimer lasers provide low pulse repetition rates in the range of a few hundreds per second but the large beam cross section permits parallel processing by means of mask projection. Solid state lasers with there high repetition rates of up to 10^6 Hz, on the other hand, allow efficient sequential processing by focusing the beam.

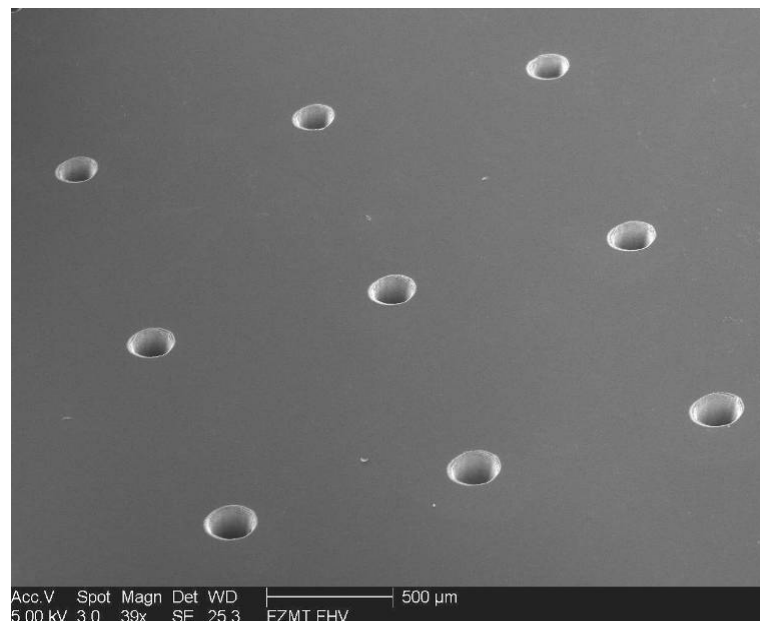


Figure 28: Array of through-vias in a 3C-SiC wafer with a thickness of 400 μm drilled with a solid state laser providing pulses with a duration of 300 fs at a wavelength of 1040 nm. [P7]

Figure 28 shows an array of vias drilled in 3C-SiC at a wavelength of 1040 nm with a pulse duration of 300 fs. Despite the relatively low fluence of 10.6 J/cm^2 , through via drilling was possible by employing trepan drilling where the beam moves along a circular path. The drilled vias exhibit smooth sidewalls and the surrounding area is not affected by the drilling process. The drilling speed of approx. 10 to 15 $\mu\text{m/s}$ is significantly higher than the one of RIE which is in the range of a few microns per minute. Of course, depending on the

application, the RIE process is more efficient by parallel processing, while for single vias or as a flexible tool for fast prototyping laser ablation is an attractive option.

5.1.3 Morphology

The different mechanisms underlying ablation with pulses in the nanosecond and femtosecond time regime leads to significant variations in morphology of the cavities.

But also just moving from 248 nm wavelength to 193 nm at comparable pulse lengths leads to a high improvement of the structure quality. Figure 29 shows SEM micrographs of cavities in silicon carbide ablated with excimer lasers with pulse durations in the ns time scale and a wavelength of 193 nm (A) and 248 nm (B), respectively. In both cases the sample was machined with a train of 100 pulses. The sidewalls are smooth, steep and in addition the upper edge is very sharp. The bottom surface is only slightly undulated compared to the KrF experiments.

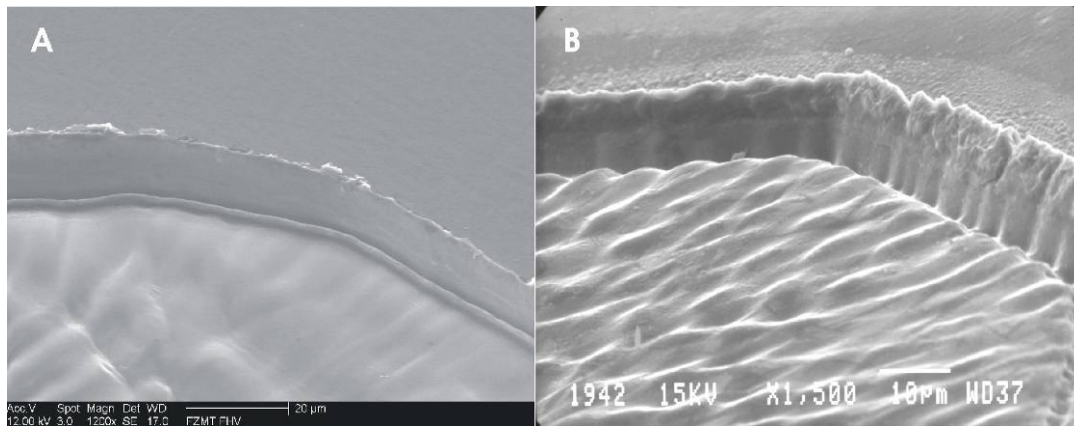


Figure 29: Comparison of cavities (3C-SiC) ablated with excimer lasers with pulse durations in the ns time scale and a wavelength of 193 nm (A) and 248 nm (B), respectively

In the case of ns-ablation of SrTiO_3 and depending on the laser intensity various detrimental effects can be observed that are due to the thermal nature of the ablation process. At a fluence of 0.2 J/cm^2 darkening of the irradiated area occurs after a single pulse, which may be due to a chemical modification of the surface region. More strikingly, higher fluences lead to the formation of cracks along the crystallographic axis. This effect has also been mentioned in an earlier study with ns pulses [25]. In figure 30 a section of an ablated area is shown after a single shot at a fluence of 1.5 J/cm^2 . It can be seen that parts of the rectangular cracks extend beyond the irradiated area. They resemble shingles and their size is varying

from approximately three up to twenty microns. The threshold fluence for crack formation is 0.3 J/cm^2 , which is below the ablation threshold of 0.6 J/cm^2 for single pulse irradiation. The cracks appeared over the whole energy range used for the single pulse experiments ($0.3\text{-}7 \text{ J/cm}^2$).

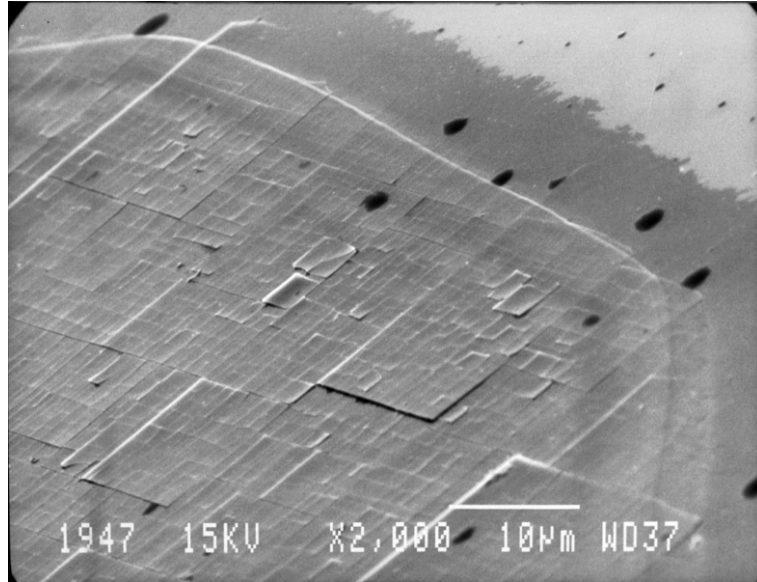


Figure 30: Crack formation along the crystallographic axis of SrTiO_3 after a single shot with a fluence of 1.5 J/cm^2 , $\lambda = 248 \text{ nm}$, $\tau = 34 \text{ ns}$ [P11]

After hundred pulses the effect of cracking can still be observed but it starts to disappear at fluences higher than 0.7 J/cm^2 , which we attribute to partial thermal annealing. Despite the annealing, a significant residual distortion of the crystal lattice remains, as outlined below. In the case of ultra short pulses neither darkening nor formation of cracks can be observed at any fluence neither for single nor for multi-shot irradiation.

The formation of cracks has been attributed to a thermal process comprising shockwave excitation in the material [75]. Although the photon energy (5eV , 248 nm) used is high, thermal interactions seem to dominate on the nanosecond timescale. As SrTiO_3 exhibits low thermal conductivity ($12 \text{ Wm}^{-1}\text{K}^{-1}$) and the melting/boiling points are very high (2080°C and $>3000^\circ\text{C}$, respectively), a strong temperature gradient, resulting in thermal shock is induced in the surrounding material, leading to the cracking of the material along the crystallographic planes.

On the femtosecond time scale the ablation process is faster than the energy transfer into the bulk material. So nearly all of the energy deposited by the laser pulse is used for the material

removal and carried away by the ablation products. Because of the negligible heat transfer into the material bulk, thermal shock and melting is avoided.

To study the mechanical impact on the material x-ray diffraction (XRD) measurements have been carried out after exposure of the samples with fluences below the multi pulse ablation threshold. With x-ray diffraction one can reveal information about the crystallographic structure, chemical composition, and physical properties of materials and thin films and is based on observing the scattered intensity of an x-ray beam hitting a sample. Shifts in the diffraction spectrum compared to a reference (untreated sample in this case) indicate a change of a lattice parameter and gives information about the strain. In figure 31 the graph of the untreated surface is juxtaposed with results from areas irradiated with femto- and nanosecond pulses, respectively.

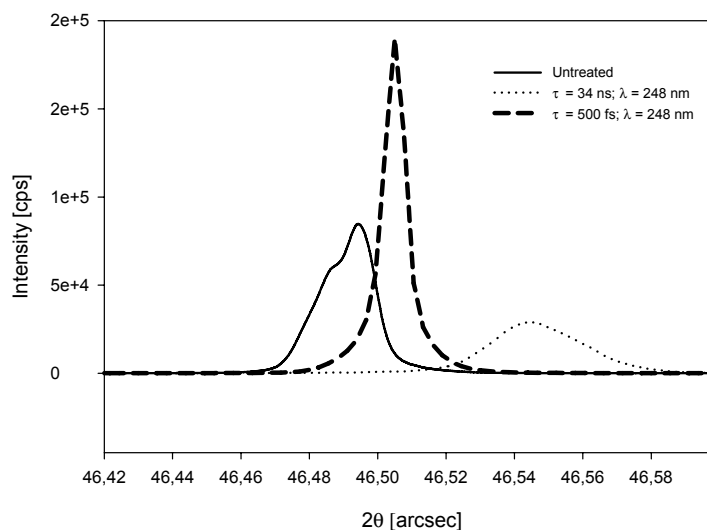


Figure 31: XRD-measurement of SrTiO₃. The sample has been exposed with fluences just below the ablation threshold. [P11]

Sample areas exposed to nanosecond pulses display a shift of the diffraction peak to larger diffraction angles indicating compressive stress. The shift resulting after femtosecond irradiation is significantly smaller indicating the much lower mechanical load on the material.

Besides the effect of cracking, additional differences in morphology can be seen by comparing the ablated cavities. Figure 32 shows a scanning electron micrograph of an area ablated with hundred shots at a fluence of 3.3 J/cm² and a pulse duration of 34 nanoseconds. The corrugated shape of the bottom area most likely results from the annealing of the afore mentioned cracks by melting and resolidification of the material.

The bottom also shows pores with a size of approximately 300 to 800 nm, which is also an evidence for melting. Their appearance is significantly more abundant at the partially annealed, but still distinguishable cracks. The sidewalls are smooth and, in addition, the lower edge is very sharp. In comparison to ablation with femtosecond pulses (figure 33) the surrounding area is more affected due to the higher heat transfer into the bulk material.

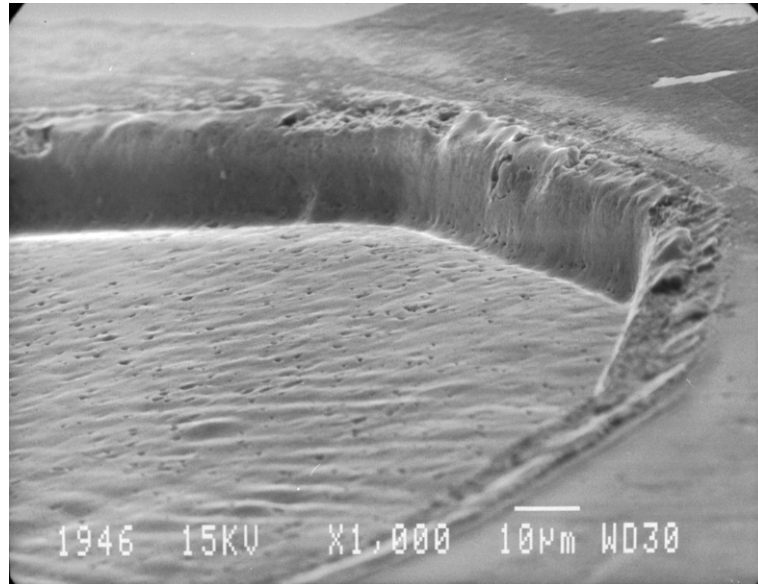


Figure 32: Ablated cavity in SrTiO_3 after 100 shots at a fluence of 3.3 J/cm^2 , $\lambda = 248 \text{ nm}$, $\tau = 34 \text{ ns}$

The upper edge is rounded and the transition to the unexposed area shows ejected material and a rough surface indicating thermal damage.

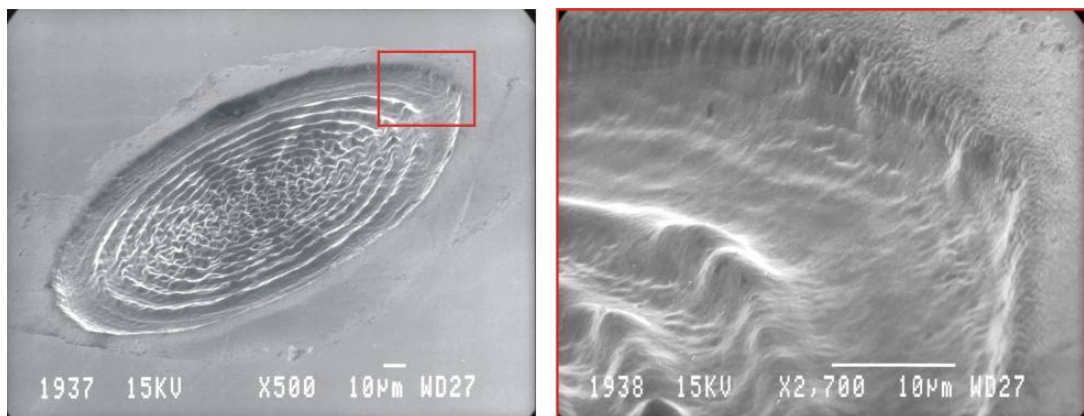


Figure 33: Ablated structure in SrTiO_3 , $\lambda = 248 \text{ nm}$, $\tau = 500 \text{ fs}$

In contrast to this, the SEM micrograph of the femtosecond ablated structure (figure 33) shows no indication of melting. It exhibits sharp edges and less debris deposited at the surrounding area. The pores mentioned before can not be observed when using femtosecond pulses. The surface relief is a replica of the intensity distribution of the laser beam (which is a diffraction pattern of the circular aperture used for beam shaping).

Chapter 6: Selective ablation schemes

The well defined ablation thresholds in ultrashort pulsed ablation and the resulting selectivity of ablation of material layers allows 2- and 2½-dimensional patterning, respectively. The benefit of the selective ablation scheme compared to bulk machining is that variations in the vector velocity and the resulting variation of the pulse-to-pulse overlap do not affect the depth profile.

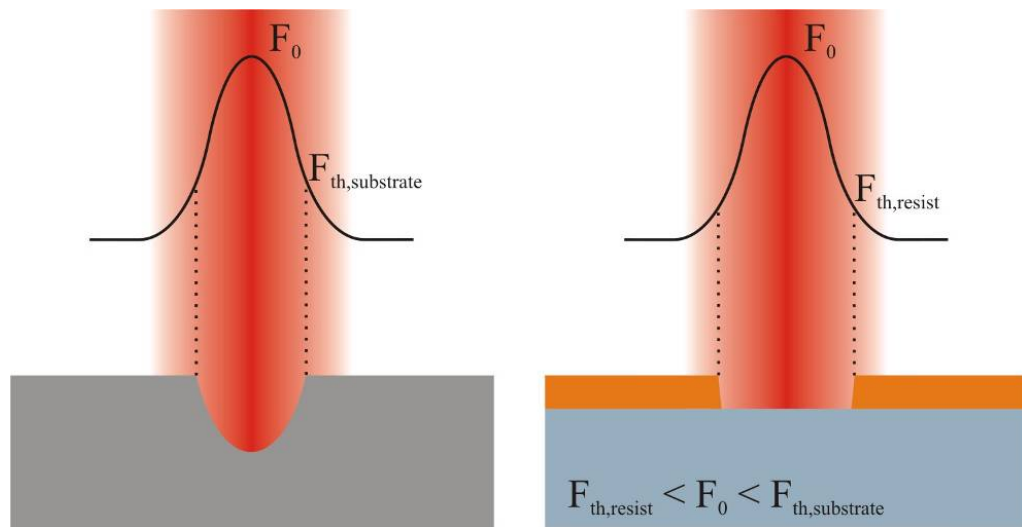


Figure 34: Schematic diagram of selective structuring of photoresist compared to bulk machining. The cross section of the ablated area exhibits a trapezoidal shape.

Additional, the cross-section of an ablated structure by applying the selective ablation scheme does not exhibit the (Gaussian) intensity profile of the laser (see schematic drawing in figure 34) and the depth of the structure is solely determined by the thickness of the material layer.

6.1. Thin Film removal for Photovoltaic Applications

In view of the increasing importance of solar energy technology, new, efficient and versatile process steps in the fabrication of solar cells are in great demand. One of the critical manufacturing processes is the layer specific structuring of the cells.

In general there exist two different concepts to build solar cells: One is based on conventional silicon microtechnology, the other one on thin film technology where integrated circuits are

generated on insulating substrates by vapor deposition techniques. The most important types are CIS (copper-indium-diselenide) - and a-Si solar cells (figure 35).

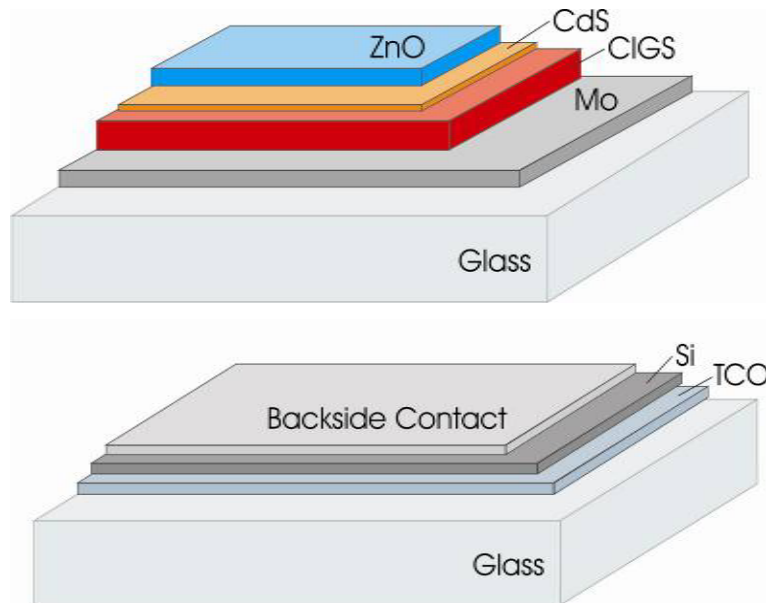


Figure 35: Schematic view of a copper indium selenide (CIS, upper side) and an a-Si solar cell. The transparent conductive oxide (TCO) and the Mo layer must be selectively ablated from the glass substrate for structuring the first layer

Although thin film solar cells exhibit lower efficiencies, their much lower manufacturing costs and the minimized silicon input are convincing advantages [4], [99]. Laser ablation of metals [102] and transparent materials with ultrashort UV and IR pulses, respectively, has been demonstrated to yield very well defined microstructures [12]. Structuring of solar cells has been studied previously with IR as well as with UV laser sources [6], [42], [64]. In this work the selective ablation of TCO (ZnO, SnO₂) and Mo with femtosecond laser pulses has been studied. In particular, the multipulse ablation thresholds for various layers and the substrate has been determined. Additional focus was set on the structuring speed and the minimized material loss (small ablation kerf widths).

We used a diode pumped solid-state laser emitting pulses at a wavelength of 1040 nm and a pulse duration of 300 fs (High Q Laser). The laser can be operated at a repetition rate of up to 10 kHz. The intensity of the beam was adjusted with a combination of a half-wave plate and a polarizer. The beam (Gaussian beam shape) was focused onto the surface of the sample by means of a microscope objective (20) or a single lens with a focal length of 50 mm. The sample was placed on a motorized xyz-translation stage.

The beam diameter on the sample surface as well as the ablation threshold of the material was derived by the Liu-methode described in chapter 4.2.2. In case of the TCO coatings, a single spot treated with a train of 100 pulses was ablated to determine the ablation parameters.

Thin films were made of Molybdenum (backside contact for CIS solar cells), the metal which exhibits the highest melting point of all pure elements (2623°C) and transparent conductive oxides (ZnO, SnO₂).

For the experiments with the Mo-layer of 500 nm thickness the beam was focused to a diameter of 8.6 microns by means of a microscope objective. On the one hand the line width should be minimized so as not to waste active area and on the other hand the machining velocity should be maximized. By focusing the beam to diameters of a few microns, a pulse energy in the sub- μ J range is sufficient to achieve ablation. In this pulse energy regime so called cavity dumped laser systems are available with repetition rates of one MHz and more. Alternatively, amplified laser sources provide maximum rates of 500 kHz.

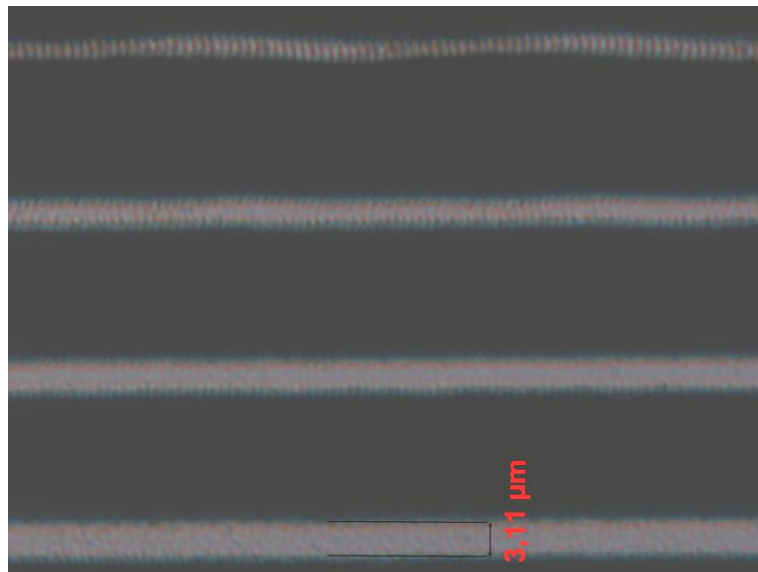


Figure 36: Thin film of molybdenum on glass structured at different velocities (0.5, 1, 2 and 4 mm/s) with a pulse energy of 800 nJ. The beam was focused to a diameter of 8.6 μ m [P1]

Our experiments have been carried out at repetition rates of 10 kHz, generating straight lines at various scan velocities and pulse energies. At a pulse energy of 800 nJ and a velocity of 1 mm/s, molybdenum layers can be completely removed from the glass substrate. By extrapolating the ablation parameters to a repetition rate of 1 MHz a process speed of 100 mm/s appears to be possible with a cavity dumped laser system.

In figure 36 an optical transmission microscope image of four lines ablated at different velocities is shown. In this low fluence regime the upper velocity limit is determined by the formation of ripple structures. The formation of ripples is a well known effect in ultrashort pulsed laser ablation [118]. An SEM image of these ripples is shown in figure 37. The orientation is perpendicular to the laser electric field which in our case was parallel to the processing direction. By employing circular polarization this effect can be partially suppressed.

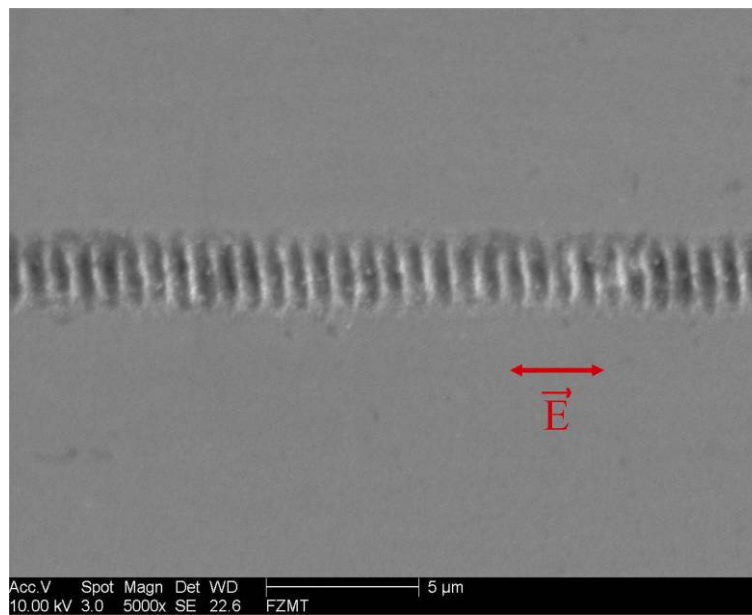


Figure 37: Line ablated in Molybdenum with linear polarized light. At fluences close to the ablation threshold the well known effect of ripple formation can be observed. By employing circular polarization this effect can be practically avoided [P1]

The ablation rate of molybdenum was determined to be 0.7 J/cm² and is given for a pulse to pulse overlap of 99.4% calculated by

$$\text{Overlap [\%]} = 100 \cdot \left(1 - \frac{\text{process speed [m/s]}}{\text{Rep Rate [s}^{-1}\text{]} \cdot \text{spot diameter [m]}} \right)$$

whereas the threshold for the glass substrate was found to be between 2 and 2.6 J/cm², depending on the glass type.

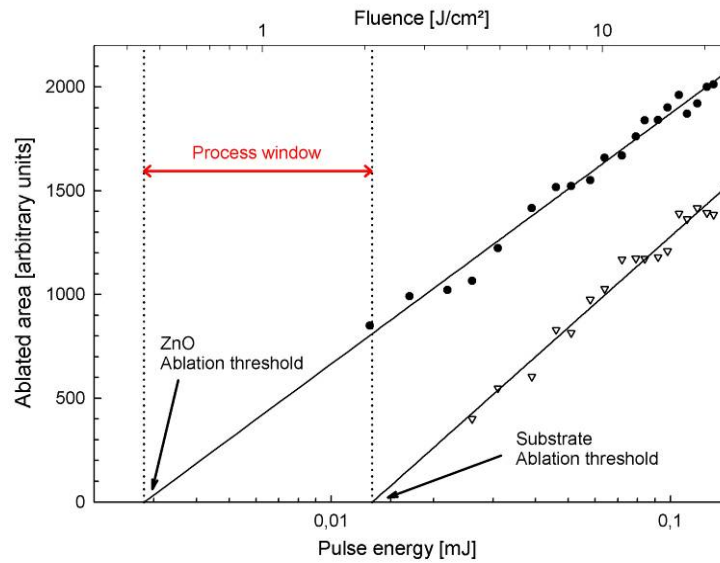


Figure 38: Determination of the ablation threshold of ZnO and the substrate by plotting the ablated area versus pulse energy. The intersection with the ordinate indicates the ablation threshold. The range of fluences between the two threshold values defines a process window where the TCO film can be selectively removed from the substrate. [P1]

In figure 38 a plot of ablated area versus pulse energy is shown, from which the ablation threshold of ZnO and the glass substrate was inferred to be 0.44 J/cm^2 and 2.6 J/cm^2 , respectively. At 0.73 J/cm^2 , the ablation threshold of SnO_2 turned out to be slightly higher than that of ZnO. The values are given for a train of 100 pulses ($\lambda = 1040 \text{ nm}$, $\tau = 300 \text{ fs}$).

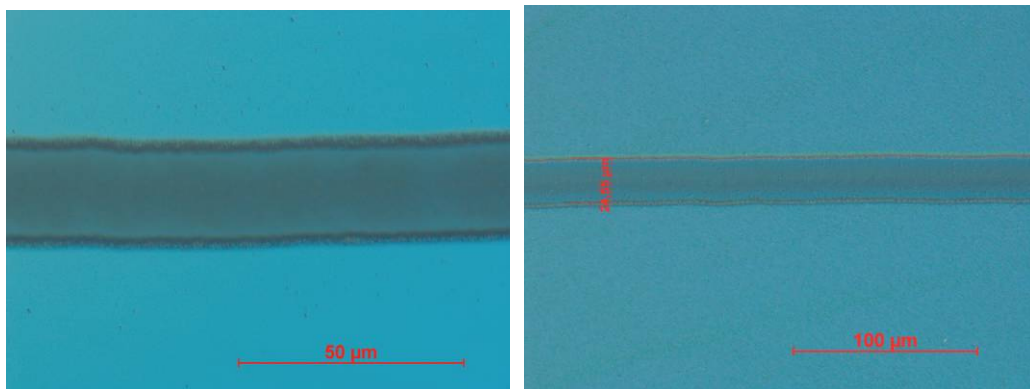


Figure 39: Thin layer of zinc oxide (a) and tin dioxide (b) selectively ablated from the glass substrate with a fluence of 0.5 J/cm^2 and 0.8 J/cm^2 , respectively (10 kHz , 1 mm/s). [P1]

The different thresholds for TCO and glass substrate permits selective ablation of the TCO layer from the latter. Figure 39 shows experimental results for ZnO and SnO₂, respectively, on glass (layer thickness 1 µm).

6.2. Selective Laser Ablation of Photoresists for MEMS Devices

Another possible application for selective ablation is the structuring of thick photoresist from substrates exhibiting a higher ablation threshold. In this case the substrate operates as an etch-stop layer.

Structuring thick photoresist layers is usually done with conventional lithography methods. Resist materials like SU-8 or KMPR are widely used for the UV-LIGA (Lithographie, Galvanik und Abformung) process where the resist is exposed through a mask with UV light from a mercury lamp, usually at wavelengths between 250-450 nm. One of the disadvantages of this process is the need of a mask, which reduces the flexibility, especially at the stage of early development. Direct structuring by laser ablation, because mask- and developementless, may be a suitable process to overcome this problem.

Selection of a suitable Substrate/Resist -System

The proper substrate-resist combination is the first step which has to be considered to guarantee a process window where selective ablation is possible. Additionally the width of this window has to be big enough to allow an acceptable process speed.

There exist various resist materials used for photolithography. First of all, they are classified into two groups, the positive and negative types, respectively. Once exposed to (UV-) light a positive resist becomes soluble and the illuminated areas can be removed by a proper developer. In the case of a negative resist the areas that are exposed to light become insoluble to the developer. These areas remain whereas the unexposed parts can be easily dissolved.

In our case negative resist types are used for two main reasons. The first one is the laser plasma plume during ablation. It exhibits high energetic photons so that the surrounding area of the generated structure would be exposed and turned to the soluble state. This limits the possible wet cleaning liquids for a subsequent rinse step drastically. Negative resist types, once exposed, are unaffected to the laser plume radiation on the one side and are resistant to a variety of solvents on the other side.

The negative resist material AZ[®] nLOF 2070 is resistant to Isopropyl Alcohol (IPA), which was used for cleaning the sample between the process steps.

In figure 40 the absorption coefficient of this resist type for a wavelength range from 300 to 500 nm is shown. Due to the fact that the resist is conventionally used for UV lithography with a mercury-lamp emitting between 250 and 450 nm, no absorption spectra are available for lower photon energies. Since the material is transparent in the visible coupling into the material has to rely on two- or multiphoton absorption.

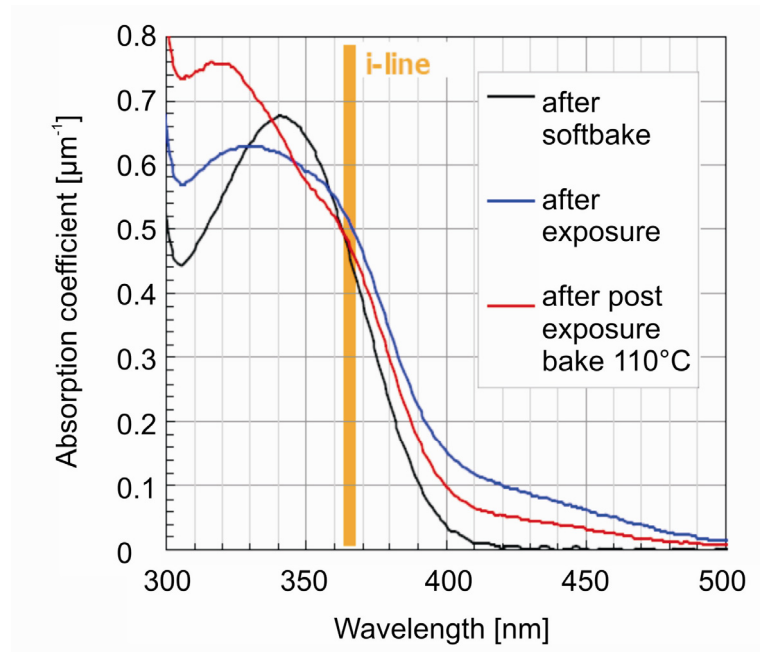


Figure 40: Absorption coefficient of AZ® nLOF versus wavelength; the resist is a poor absorber at the second harmonic (520 nm) so the light-material coupling has to rely on two-photon absorption (source: Microchemicals GmbH)

The multipulse ablation threshold of AZ® nLOF 2070 for the second harmonic wavelength was determined by the method explained in section 4.2.2 and turned out to be 0.21 J/cm². To determine the ablation thresholds for the substrate and the resist the beam was focused by a single lens ($f = 60$ mm) on the sample surface. Structuring tests have been carried out with resist coated silicon wafer. However, silicon exhibits a threshold below that of the resist material and is for that reason not suitable as substrate material for selective laser processing. A material providing an ablation threshold high enough to allow selective ablation is glass. We used borosilicate glass wafers (D 263 T, Schott) of four inch diameter and a thickness of 300 microns to replace silicon as substrate material.

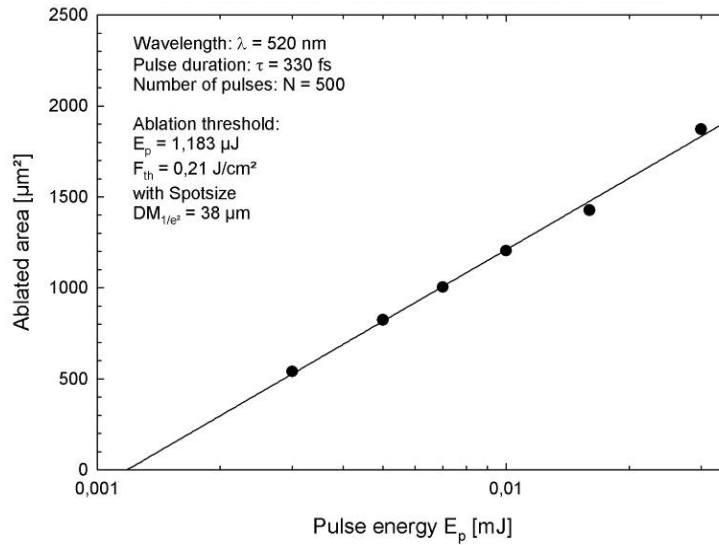


Figure 41: Determination of the multipulse ablation threshold of AZ[®] nLOF 2070. The sample was treated with a burst 500 pulses at a repetition rate of 1 kHz

The substrate exhibits a multipulse ablation threshold of 2 J/cm² for the fundamental and 1.04 J/cm² for the second harmonic wavelength (see figure 42), respectively.

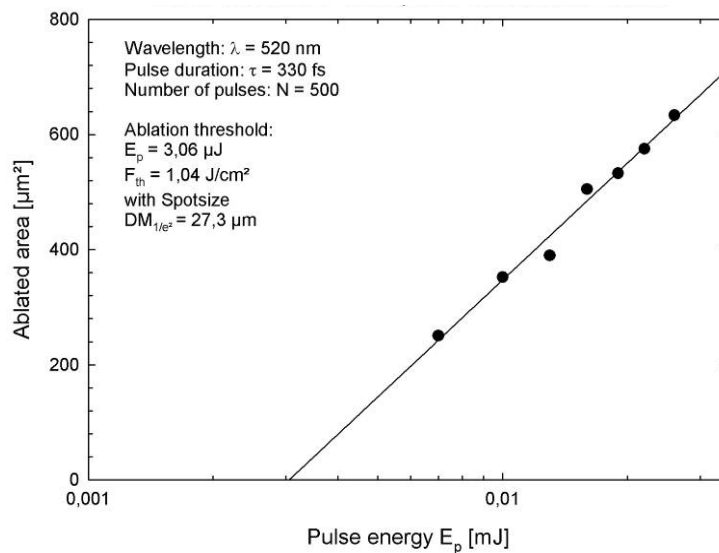


Figure 42: Determination of the multipulse ablation threshold of borosilicate glass (D 263 T, Schott) for a pulse duration of 330 fs and a wavelength of 520 nm.

The samples were prepared as followed. At first the glass wafers were cleaned with Acetone and IPA. To avoid stripping of the resist from the glass wafer an adhesive layer (Ti-Prime) was applied. Afterwards the resist was spinned on and softbaked for two minutes at 100 °C. With one spincoating step a resist thickness of approx. 15 microns can be achieved. This process was repeated up to three times which results in a layer thickness of approx. 44 microns. A subsequent flood exposure turns the material in its unsolvable state. After a postexposure bake at 110° for 15 minutes the sample was ready for the ablation experiments.

Resist structuring at 1040 and 520 nm

Test structures of circular and rectangular shapes were first generated with 1040 nm radiation. When ablating with this wavelength, the resist material tends to form shell-shaped spallations at the edges of the structures which is not acceptable for applications in microtechnologies. Even with a fluence slightly above the threshold this effect could not be avoided. For this reason the second harmonic was used for further experiments.

For tests at a shorter wavelength SH radiation was generated in a BBO crystal and separated by using a dichroic mirror in the beam path. The beam was directly focused on the sample surface by a single lens with a focal length of 75 mm. The beam diameter was determined to be 38 microns on the sample surface.

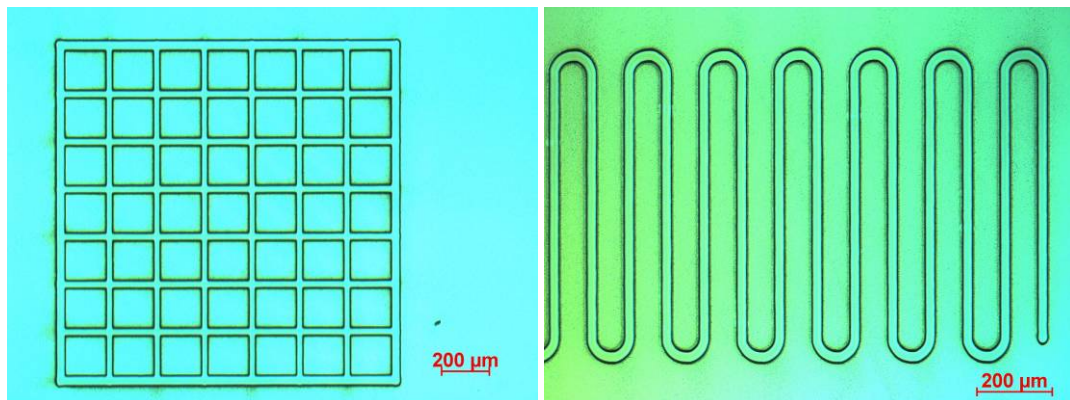


Figure 43: Test structures ablated on an 11 micron thick resist sample with a wavelength of 520 nm, a fluence of 0.4 J/cm², a repetition rate of 5 kHz and a scan velocity of 0.5 mm/s. The resist shows no tendency of local melting; the cutting edges are well defined and show no chipping of material as observed when using the fundamental wavelength

Rectangular and meander-shaped test structures were generated on an 11 micron-sample by removing the resist from the glass substrate (see figure 43). The bottom surface of the

structure is not affected by the structuring process and the microscope images show no significant recast.

Figure 44a and b show different structures ablated in AZ[®] nLOF of 44 μm thickness with a fluence of 0.35 J/cm² at a repetition rate of 5 kHz and a pulse duration of 330 fs. They were generated by scanning with a pitch of 10 microns between the lines and a scan velocity of 1 mm/s. It can be clearly seen that the cutting edges are again well defined and the problem of spallation could not be observed also for thick resist layers.

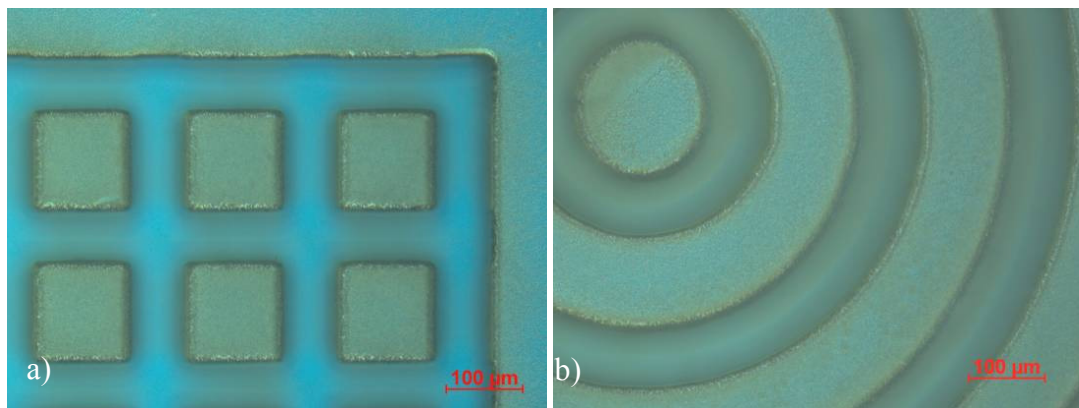


Figure 44: Test structures in AZ[®] nLOF 2070 selectively removed from a glass substrate with a fluence of 0.35 J/cm², a repetition rate of 5 kHz and a scan velocity of 5 mm/s

With increasing resist thickness the problem of debris which is deposited around the structures becomes more and more serious. Because of the high resistance of this photoresist to solvents rinsing with isopropyl alcohol (IPA) after laser structuring was not effective to remove the recast material. Additional ultrasonic treatment leads to a partial stripping of the resist from the substrate which is shown in figure 45. This may cause a problem for subsequent process steps.

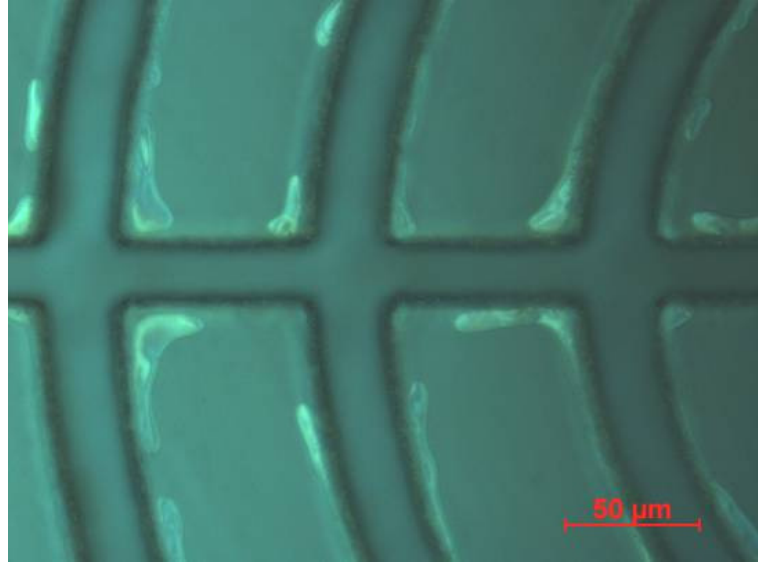


Figure 45: Structure showing a partial stripping of the resistlayer from the substrate after treatment in an ultrasonic bath to remove the recast layer on the top surface

One possible strategy to prevent deposition of debris is to increase the mean free path of the ablated particles given by

$$l_m = \frac{1}{\sqrt{2}} \frac{1}{n \sigma_d p}$$

where σ_d is the effective cross section area for collision, p is the pressure and n is the number of particles per unit volume. The most effective way is to work in vacuum, but this increases the processing time as well as the setup complexity. Another possibility is to use a process gas exhibiting a smaller cross section than air molecules.

For this reason tests have been carried out with Helium. Structuring tests were carried out with a constant Helium flow where a gas nozzle was placed close to the sample. In this fashion the recast on the surface can be decreased but it was not possible to completely remove it by subsequent rinse steps.

Another strategy, such as employing a thin sacrificial layer of photoresist on the top surface which can be removed selectively by the resist developer, turned out to be efficient and simple. The positive AZ-type (AZ[®] 6612) was spincoated on the sample after the post exposure bake. A resist thickness of 1.4 microns was sufficient for this purpose. After laser structuring a final flood exposure was carried out for two purposes. On the one side the (negative) shaping resist layer becomes even more resistant where the sacrificial layer, which is of positive type, changes into its solvable state.

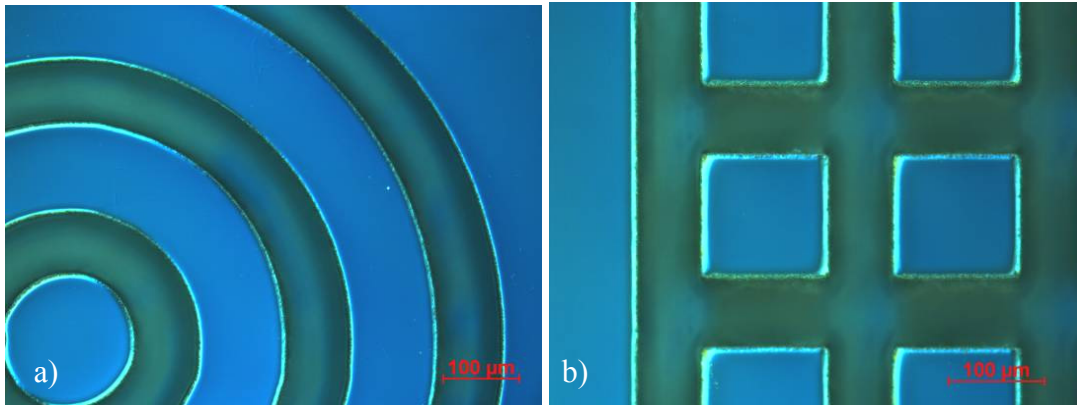


Figure 46: Structures generated in AZ[®] nLOF 2070 by selective laser structuring from a glass substrate; by employing a sacrificial resist layer (AZ[®] 6612), which can be solved by a subsequent rinse step, the debris on the top surface can be completely removed

The sacrificial layer was removed by a rinse step for one minute in AZ[®] 726 MIF, a special developer for these resist systems. The recast was completely removed from the sample surface. Figure 46 shows two structures after the removal of the AZ[®] 6612 layer.

Depending on the resist thickness two or more recurrences of the scanning procedure have to be carried out to completely remove the material. In figure 47 White Light Interferometer images (see appendix A1) of two scanned areas are shown.

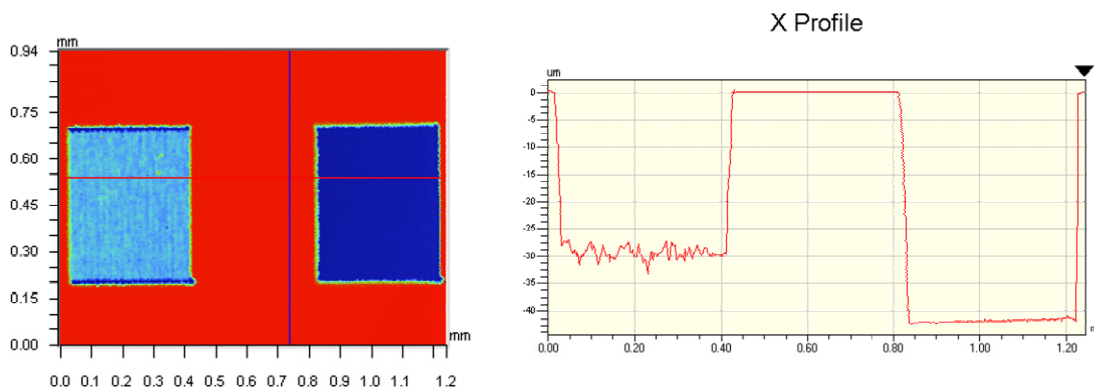


Figure 47: Rectangular test structures with varying scanning recurrences; measurements carried out with a White-Light Interferometer show a top view and a cross section of two ablated areas after one and two recurrences, respectively. The areas were scanned vertically with a pitch of 10 µm and a vector velocity of 1 mm/s. The laser beam was attenuated to a pulse fluence of 0.4 J/cm² at a repetition rate of 5 kHz.

After the first scanning procedure a depth of approx. 30 microns was achieved. A second time completely removed the layer. By comparing the two areas in terms of surface quality a much higher quality of the bottom area is achieved by the etch stop at the substrate with respect to bulk machining. Measurements of the average surface roughness (R_a) carried out with the White Light Interferometer shows a value of $R_a = 0.79 \mu\text{m}$ after the first scan. The second iteration, leading to a complete removal of the layer, results in a surface roughness of $R_a = 0.05$ microns.

It can also be seen in figure 47 that the side walls of the ablated structures are inclined. The resulting angle is a consequence of the Gaussian beam profile. If the structures are used for embossing means a certain inclination of the side wall is desired for the subsequent demoulding of the sample. If smaller angles are needed, the intensity profile of the beam should be changed to a tophat profile.

The second scan, where the resist layer is completely removed, also removes any recast.

To further increase the quality of the bottom surface “laser cleaning scans” have been carried out where the debris of the previous scan procedure is ablated again. In figure 48 a and b six ablated areas are shown after scanning several times from one (rectangle on the right side in figure 48 b) up to six repetitions (figure 48 a left).

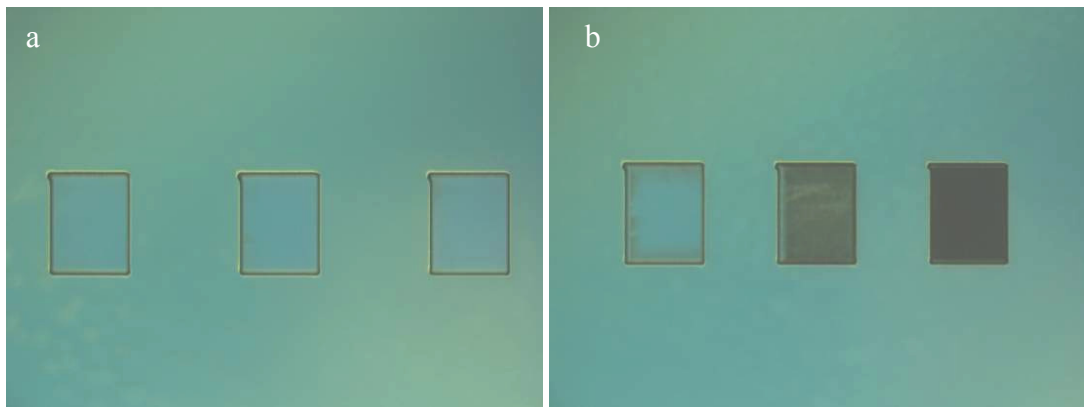


Figure 48: Six rectangular test structures in photoresist AZ[®] nLOF 2070, selectively ablated from a glass substrate with a pulse duration of 330 fs and a wavelength of 520 nm. The bottom surface quality can be enhanced by repetitive scans. The rectangles show the quality after one repetition (b right) up to six repetitions (a left)

The rectangles with a size of 500x400 microns were ablated with a fluence of 0.4 J/cm² and repetition rate of 5 kHz.

By looking at the surface roughness at the bottom of the structures it can be seen that the highest quality enhancement is achieved by an additional procedure after removing the resist layer.

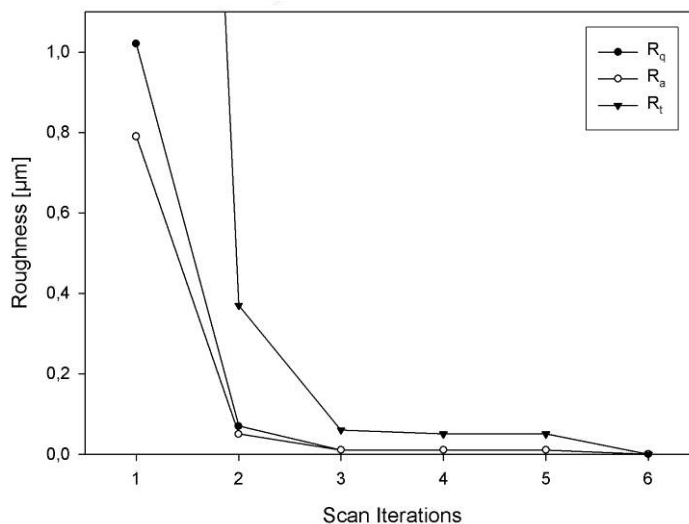


Figure 49: Surface Roughness at the bottom of the ablated structure depending on the number of scans where R_a is the arithmetic mean surface roughness, R_q the root mean square (RMS) surface roughness and R_t the peak to valley height

The results of the roughness measurements of the bottom surface is shown in the graph in figure 49 where the mean surface roughness R_a , the root mean surface roughness R_q and the total height of the measured surface profile R_t have been determined.

The results demonstrate that laser cleaning scans and the use of a sacrificial resist layer enables the generation of high quality structures in resist materials by selective ablation with ultrashort laser pulses. The structures can be used for further processing by common methods in MEMs manufacturing like plasma etching or micro electroplating.

Chapter 7: Two color ablation

Ultrashort laser pulses allow high quality machining of surfaces without thermal damage to the remaining substrate. If the pulse duration is below the electron phonon relaxation time that ranges from femtoseconds to a few picoseconds, nonthermal ablation mechanisms come into play that may in some systems improve the ablation results. Excellent results have been obtained with femtosecond laser pulses from amplified Ti:Sapphire oscillators [37], [55], [108], [114]. Femtosecond pulses require complex and expensive sources and are difficult to handle because of pulse dispersion in the steering and focusing optics. However, even pulse durations just below about 10 ps allow multiphoton excitation at moderate pulse energies so that media transparent to the laser radiation such as dielectrics and semiconductors can be machined with high spatial precision [75], [112]. Multiphoton excitation of electrons into the conduction band serves to create a quasi-free electron gas that can then absorb the infrared radiation providing the ablation energy. Picosecond pulses are also short enough to avoid significant diffusion of the deposited energy into the substrate [27]. Compact lasers that can deliver picosecond or even nanosecond pulses of sufficient energy are therefore important sources for laser ablation from a commercial point of view.

Since for a given pulse energy the rate of n-photon transitions scales with τ_p^{-n} , where τ_p is the pulse duration, lasers with longer pulse durations are far less efficient than femtosecond lasers in producing the required initial free carrier population and tend to waste a considerable amount of energy by transmission into the substrate before a significant conduction band population can build up. Various techniques have been developed to ‘seed’ the conduction band with carriers and thus to increase the ablation rate and/or improve the ablated cavity. One possibility is to excite the material (predominantly dielectrics) with additional pre-pulses of a UV- or a IR-femtosecond laser. In [45] and [57] the fourth harmonic of a Nd:YAG laser was used in combination with a Raman cell filled with hydrogen gas to generate a VUV excitation beam (171 nm and 184 nm) that was employed to produce excited states in fused quartz which was ablated by the remaining 20% of the laser beam.

Other groups carried out dual beam experiments by exciting fused silica by means of an F₂-excimer laser (157 nm) and ablating with another excimer laser at 248 nm [47], [62], [63]. In another approach, [29] increased the ablation rate of femtosecond laser pulses using subsequent pulses ($\lambda = 532$ nm) with a pulse length in the nanosecond time scale and a fluence which was below the ablation threshold. While these studies demonstrated enhanced yields, it was achieved at the expense of significantly increased complexity (two-laser-

systems) or a strongly reduced efficiency (UV-conversion schemes). A promising new technique is to exploit incubation effects with temporally tailored pulse trains [95], [96], [105].

The above mentioned developments suffer from unavoidable energy losses due to limited conversion ratios to the harmonic wavelengths or from complex two-laser setups. As a highly efficient and inexpensive alternative we introduce a two-color scheme that relies on the lossless conversion of a small fraction of the fundamental beam to its second or third harmonic. We investigated the dependence of the ablation yield effect on the pulse duration and a time delay between fundamental and harmonic pulse. We also performed ablation experiments where the SH radiation was replaced by variably delayed excimer (ArF) laser pulses. These experiments have been carried out with an ablation pulse with a length of 10 ps.

7.1. Two color ablation: Nanosecond pulses

The laser used was a Q-switched Nd:YAG system (“Brilliant” Quantel) providing laser pulses at a wavelength of 1064 nm and a pulse duration of 5 ns. For the ps experiments a Nd:Vanadate laser was used emitting at the same wavelength allowing a comparison of the ablation mechanisms with just the pulse duration as a variable laser parameter.

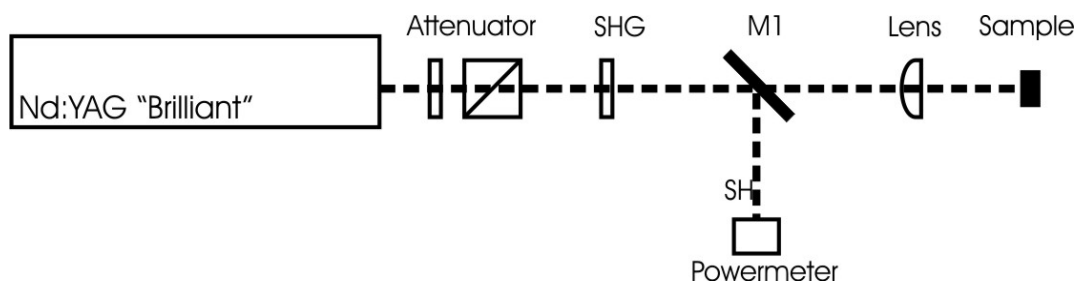


Figure 50: Schematic setup for the two-color ablation experiments with the second harmonic and pulse durations in the nanosecond time scale.

Figure 50 shows the experimental setup. The power of the beam was adjusted by a combination of a half wave plate and a polarizing beam splitter.

The harmonic radiation was generated by placing a nonlinear crystal into the beam path.

The beam was focused on the sample surface by a single convex lens with a focal length of 100 mm for the SH experiments. The fluences of the harmonics in all cases was kept below the multipulse ablation threshold.

The ablation rate was determined by measuring the cross-section of the ablated cavity with a Tencor Alphastep 2000. To allow the comparison of the ablation rates from various experiments the ablation rate was normalized to units of nm/pulse and each cavity was ablated with a burst of hundred pulses.

In figure 51 the ablation rate as a function of the conversion rate is shown with the total intensity kept constant.

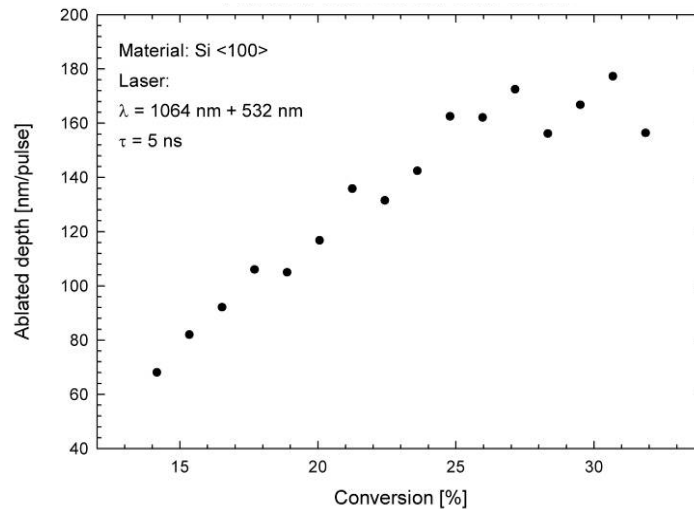


Figure 51: Ablation rate as a function of the SH-conversion, adjusted by tuning the phase matching angle. At an SH-conversion of approx. 27% the enhancement saturates.

The depth of the ablation crater increases linearly with increasing SH-conversion and saturates at a value of approximately 27%. The conversion ratio provided by the optical setup was limited to 35%. The maximum ablation rate enhancement of the two-color scheme was approximately 160 % with respect to the fundamental ablation at the same intensity.

The ablation rate saturates at values of approx. 170 nm per pulse. The excitation is generated in a volume determined by the optical penetration depth of the 523 nm wavelength. By assuming intrinsic silicon, the linear absorption coefficient α for the second harmonic wavelength is $1.12 \cdot 10^6 \text{ m}^{-1}$ which is corresponding to an optical penetration depth l_α of 893 nm which is approx. 5 times more than the highest ablation per pulse achieved with the two-color scheme. This indicates that the saturation effect occurs not due to the localized excitation volume. Rather the saturation effect can be explained by a saturation of the electron population where the absorption process by the IR radiation is initiated.

Additional experiments with cubic silicon carbide have been carried out. 3C-SiC is a wide band gap semiconductor with its minimum indirect band gap of 2.39 eV, corresponding to a

wavelength of 519 nm and its direct band gap of 5.3 eV [83] (6 eV [93]) corresponding to a wavelength of 234 (206) nm. Due to the higher band gap of silicon carbide the seeding was done with the third harmonic which was generated with an additional crystal by sum frequency mixing of the fundamental and the second harmonic. The adepte experimental setup is shown in figure 52.

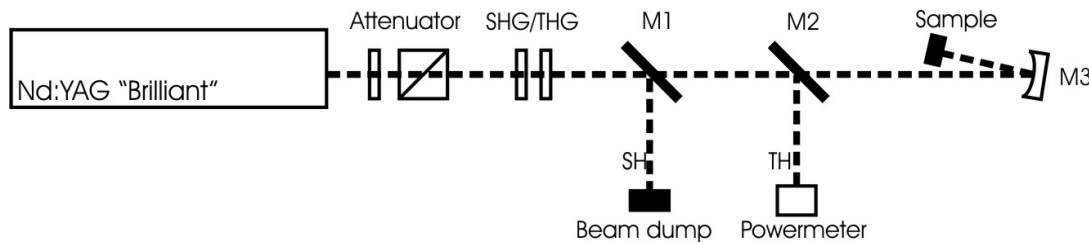


Figure 52: Optical setup used for experiments with the third harmonic generated by sum frequency mixing. To avoid chromatic aberration the beam was focused by a mirror M3.

The residual SH radiation was sampled out by a wavelength separator M1 (HR @ 532 nm, HT @ 1064 nm & 355 nm). The mirror M2 was placed on a flip mount to allow the measurement of the third harmonic intensity. To avoid chromatic aberration the beam was focused by a mirror (M3) with a radius of 100 mm corresponding to a focal length of 50 mm. The higher bandgap of cubic silicon carbide compared to silicon leads to a negligible linear absorption at the fundamental and the second harmonic wavelength.

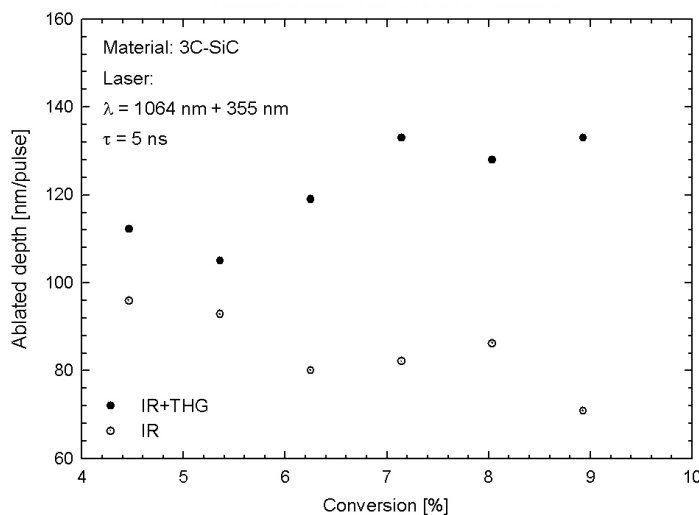


Figure 53: Ablation rate of cubic silicone carbide versus the TH-conversion of the fundamental and the third harmonic. Although the conversion was limited due to the optical setu, an enhancement effect can be observed.

Corresponding to the graph shown in figure 18 (chapter 3) the optical penetration depth for a relatively pure crystal at the second and third harmonic has been calculated to be approx. 280 and 10 microns, respectively. In figure 53 the ablation rate of 3C-SiC versus TH-conversion efficiency is shown. In our setup the conversion is limited to a value of 9 %. Nevertheless the conversion range is small, a significant enhancement effect can be observed.

7.2. Picosecond pulses: Delay time dependence of the yield enhancement

The seeding effect has been studied by introducing a time delay between the main pulse at the fundamental and the seeding pulse at the harmonic wavelength for picosecond and femtosecond pulse durations. Collinear SH radiation was again generated by passing the beam through a thin BBO crystal. The conversion efficiency was adjusted by tuning the phase matching angle. To generate a variable time delay between the fundamental and the SH pulse a setup resembling a Michelson interferometer was used employing a dichroic beam separator (reflecting at the SH and transmitting at the fundamental (see figure 54)).

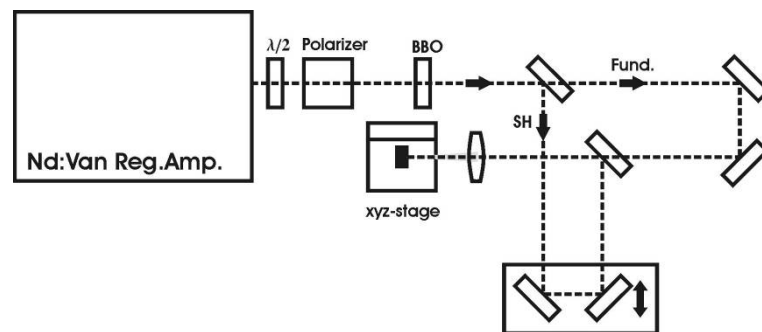


Figure 54: Schematic diagram of the setup which allows time delays from -120 to +100 ps between the fundamental and the second harmonic. The pulse overlap was determined with a LBO-crystal by the detection of the sum frequency [P2]

The fundamental beam was passed through the fixed branch of the Michelson setup, while the SH pulse was delayed by translation of the second branch reflector on a translation stage. With this setup a maximum delay time of ± 110 ps can be obtained. The beam was focused onto the surface by a single lens ($f = 100\text{mm}$); the beam diameter in the ablation plane was determined for both beams using a knife edge method. The fundamental intensity was adjusted by a combination of a halfwave plate and a polarizer. The spatial and temporal overlap of the fundamental and SH pulse was optimized by inserting a nonlinear crystal

detecting the third harmonic generated by sum frequency in the target plane. For this purpose a prism was placed in the beam path after the focal point to work as a wavelength separator. For negative delay times exceeding about $\Delta t < -40$ ps (SH pulse after IR pulse), no effect of the SH radiation on the ablation yield can be noticed, while $\Delta t > -40$ ps results in a significant increase of the ablation rate of up to 70% with respect to the rate of the fundamental alone.

The maximum enhancement occurs at approximately zero time delay, where the pulses are overlapping. With further increase, the enhancement drops quickly (within a few ps) to about 30% and then declines only slightly over our range of 100 ps provided by our setup. As can be seen from the UV seeding experiments (figure 57), the impact of the seeding lasts for several 100 ns. The ablation enhancement with UV seeding is comparable to the one obtained with SH radiation.

To study the ablation at delays longer than about 100 ps, which are difficult to realize with optical means, we employed an excimer laser with adjustable trigger delay for seeding. The setup is shown in figure 56. The trigger delay was realized electronically by a combination of a Schmitt-Trigger and an RC-circuit, with continuously adjustable resistance. With this setup delays of up to 6 ms can be obtained.

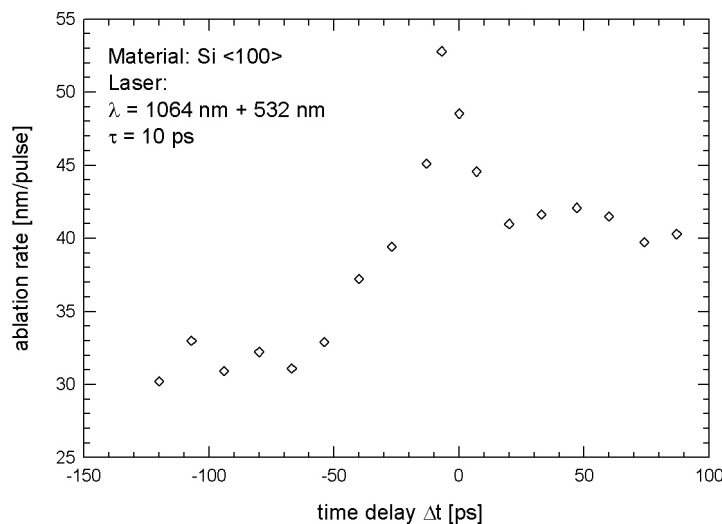


Figure 55: Ablation rate as a function of the time delay. For positive values of the delay the second harmonic pulse is earlier than the ablation pulse. The maximum enhancement occurs at approximately zero time delay, where the pulses are overlapping [P10]

The excimer laser used was an ArF with a wavelength of 193 nm and a pulse duration of 25 ns. The IR and UV beams were combined using a dichroic mirror. The time delay was

measured with an oscilloscope using two photo diodes. The intensity of the excimer laser was attenuated by expanding the beam with a Galilei telescope followed by an iris diaphragm. The ablation was carried out with the fundamental of the Nd:Vanadate laser. The intensity of the seeding laser was attenuated below the (multipulse) ablation threshold. The IR-fluence in our experiments was kept constant at 1.3 J/cm^2 , while the SH-fluence was varied up to 75 mJ/cm^2 .

Measuring the ablation rate (by means of a profilometer Tencor Alphastep 2000) as a function of the delay between the intense IR pulse and the weak seeding pulse yields a kind of cross-correlation as shown in figure 55 and figure 57.

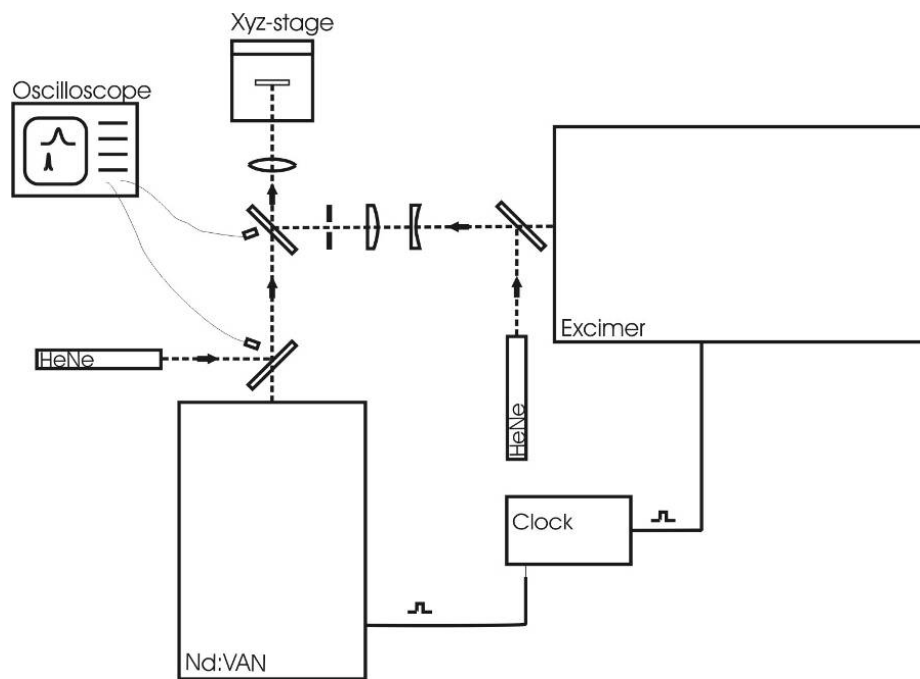


Figure 56: Experimental setup for ablation with time delayed laser pulses from an ArF-excimer laser and a Nd:VAN solid state laser. The time delay was realized electronically with an adjustable RC-element [P10]

The ‘seeding’ effect persists over the life time of the excited carriers, which in silicon and for moderate electron densities can range up to microseconds near the surface and much longer in the defect free bulk. At densities exceeding 10^{18} cm^{-3} , Auger-recombination becomes significant on the time scale of our pulse duration. While an enhanced ablation rate therefore exists for delays up to milliseconds, the maximum enhancement occurs only if the pulses overlap within a few picoseconds. Our measurements do not allow one to determine exactly the optimum delay in terms of the ablation yield, but we assume that an advance of a few picoseconds may be beneficial, since the IR-radiation then encounters an already existing

conduction band population. As an inspection of figure 55 shows, a moderate enhancement occurs also within a small range of negative delay times that is if the SH-pulse hits the target up to 40 ps after the peak of the IR-pulse.

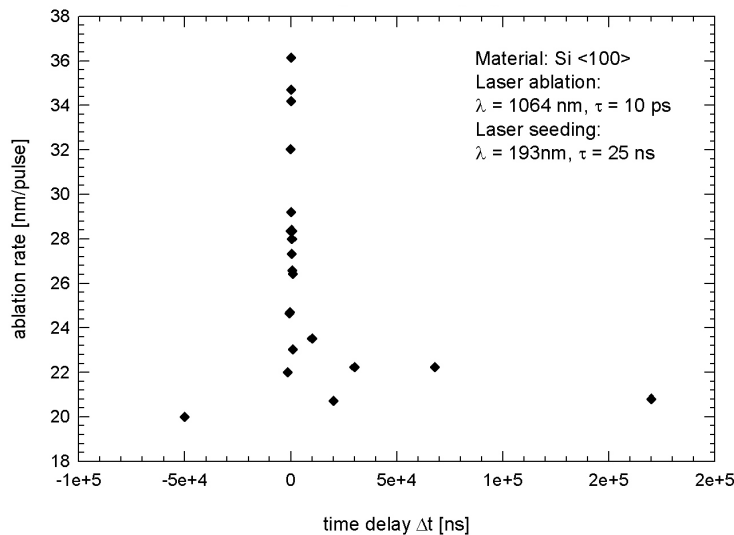


Figure 57: Ablation rate of silicon depending on the time delay between the IR pulse and the excimer laser 'seed' pulse [P10]

This is, in principle, not surprising, since the SH pulse naturally can also contribute to the heating of the free carriers. Note that under ablation conditions, the peak carrier density is such that the reflectivity of the irradiated area decreases with increasing frequency [104]; a SH-pulse arriving immediately after the IR pulse therefore experiences lower reflection losses and can deposit more energy into the target than a hypothetical IR-afterpulse of equal energy. This explains why the relatively weak SH-afterpulse can contribute significantly to the total ablation yield. For longer negative delays, the IR-generated free carriers have cooled down so far that the further heating by the SH-pulse cannot drive the system above the ablation threshold.

Over the range of seeding intensities (chosen to be significantly below the onset of multipulse damage due to the seeding pulses alone), the dependence of the ablation rate on the seeding intensity was approximately linear, as shown in figure 58.

The single shot ablation thresholds were extracted by measuring the ablated area depending on the delay between the SH and the fundamental pulse which is outlined in figure 59. The ablation threshold drops to its minimal value close to zero delay to approx. 0.5 J/cm².

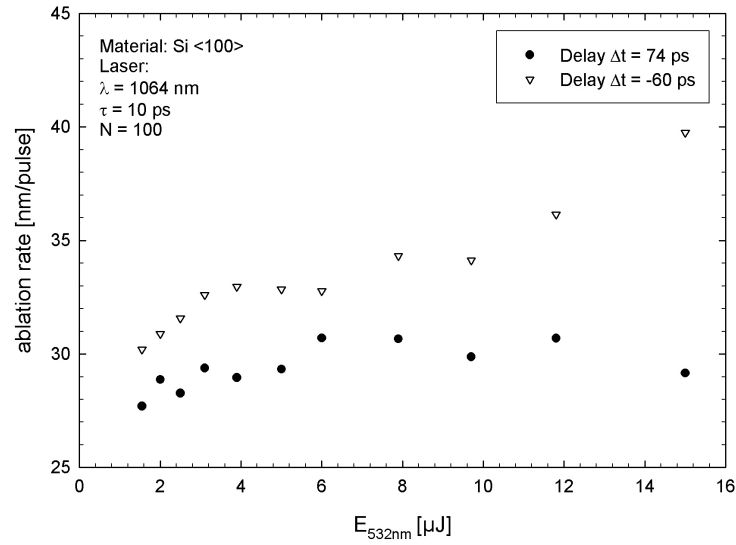


Figure 58: Ablation rate as a function of the intensity of the exciting pulse for delay times of 74 ps and -60 ps, respectively [P10]

For the fundamental wavelength the ablation threshold has been additionally determined by plotting the ablated area versus pulse energy (see figure 60).

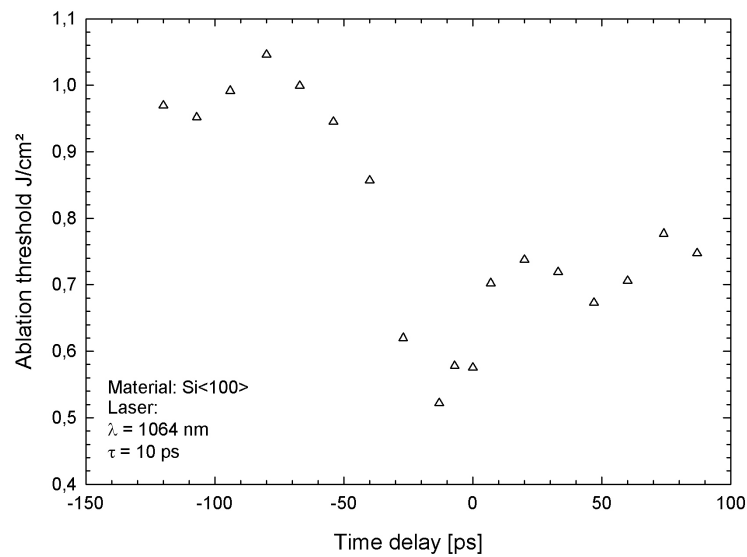


Figure 59: Single shot ablation threshold versus time delay between the SH and the fundamental pulse. [P2]

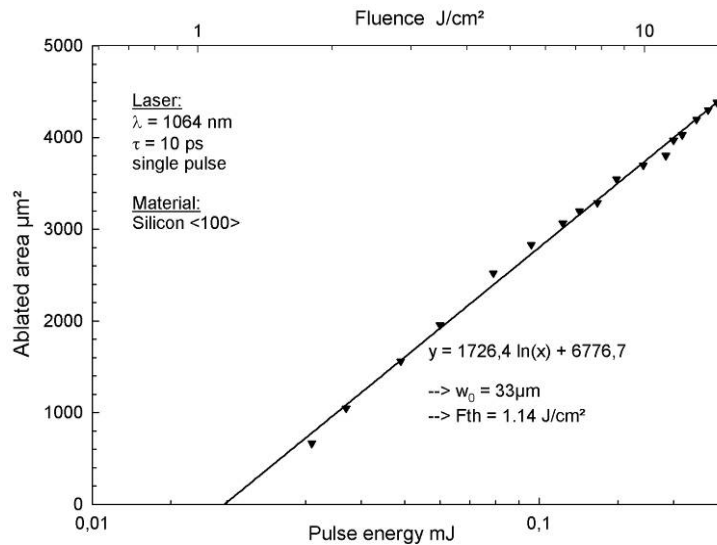


Figure 60: Determination of the threshold fluence for single pulse ablation of silicon with a pulse duration of 10 ps and a wavelength of 1064 nm. Assuming a Gaussian intensity profile the threshold fluence can be determined by plotting the ablated area vs. pulse energy.

With respect to the single pulse threshold fluence of 1.1 J/cm² for the fundamental, the value drops significantly for the two-color scheme to approximately 0.5 J/cm².

7.3. Theoretical considerations on the two-color ablation scheme

At a wavelength of 1064 nm (1.17 eV), with the photon energy hardly above the (indirect) band gap (1.12 eV), the linear absorption of silicon is negligible and ablation has to rely on two-photon absorption (TPA) to get started. The linear absorption coefficient α of silicon is $2.19 \cdot 10^3 \text{ m}^{-1}$ for the fundamental wavelength and $1.12 \cdot 10^6 \text{ m}^{-1}$ [20] for the second harmonic. Once carriers are excited into the conduction band, they gain energy from the laser field with a rate that scales with the square of wavelength λ (see equation 22). The accelerated electrons can then produce additional free carries by impact excitation. This process continues until a critical plasma density N_c is reached. At the fundamental wavelength and the second harmonic the critical density plasma is reached at

$$N_c|_{\lambda=1064nm} = \frac{\omega_p^2 \epsilon_0 m_e}{e^2} = 9.86 \cdot 10^{20} \text{ cm}^{-3}$$

$$N_c|_{\lambda=532nm} = 3.94 \cdot 10^{21} \text{ cm}^{-3}$$

$$\epsilon_0 \dots 8.8542 \cdot 10^{-12} \text{ F/m}$$

$$m_e \dots 9.11 \cdot 10^{-31} \text{ kg}$$

$$e \dots 1.6021765 \cdot 10^{-19} \text{ C}$$

For an analysis of our experimental results, we have to compare the two-photon excitation rate at 1064 nm with the linear excitation at 532 nm. Neglecting recombination and diffusion during excitation, the interband excitation rate is

$$\left. \frac{\partial N_e}{\partial t} \right|_{lin} = \frac{\alpha_{2\omega} I_{2\omega}}{2\hbar\omega} \quad \text{Equ. 32}$$

due to linear absorption by the SH radiation and

$$\left. \frac{\partial N_e}{\partial t} \right|_{TPA} = \frac{\beta_{\omega} I_{\omega}^2}{2\hbar\omega} \quad \text{Equ. 33}$$

due to TPA, where

$$I = (1 - R)I_0 \quad \text{Equ. 34}$$

is the intensity transmitted into the target of reflectivity R , N_e is the conduction band electron density, α is the linear and β is the two-photon interband absorption coefficient. The reflectivity R is 0.31 for the fundamental wavelength (1064 nm) and 0.36 for the second harmonic.

Just above the indirect band gap, silicon has a rather small TPA-cross-section of $\beta \approx 1 \text{ cm/GW}$ [50]. With the respective photon fluences ($F_{fund} = 1.3 \text{ J/cm}^2$, $F_{SH} = 75 \text{ mJ/cm}^2$) in the experiment with picosecond pulses, the linear excitation rate by the SH turns out to be six fold higher than the TPA-channel (which, of course, still contributes to the carrier excitation). With IR-excitation alone, a significant fraction of the IR-photons is lost by transmission into the sample substrate before a sufficient conduction band population can build up.

It should be noted that because of the λ^2 -dependence of the free carrier heating rate, IR-irradiation is much more efficient for the further energy deposition into the electron system. In figure 61 a comparison of the excitation rate of the fundamental wavelength and the linear excitation at the second harmonic depending on the pulse duration is shown. The calculations have been carried out for different SH-conversions from 1 up to 30 % which was in our experimental results the onset of a saturation effect.

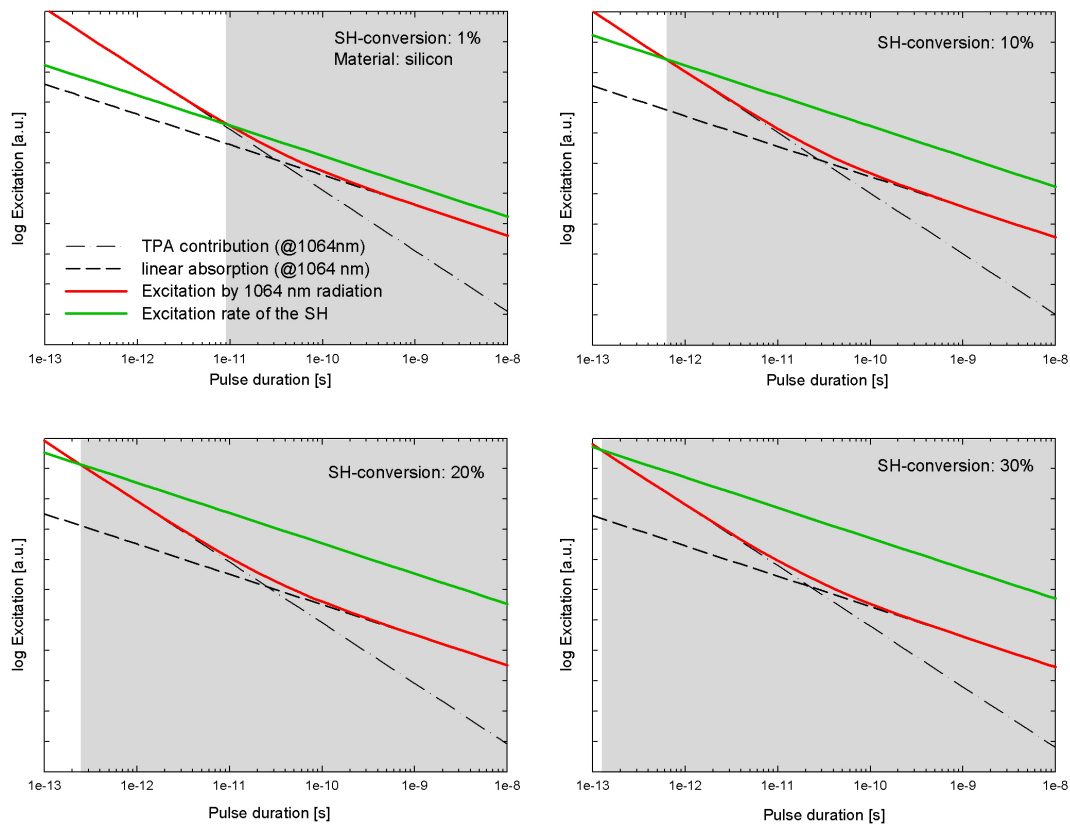


Figure 61: Comparison of the excitation rate at the fundamental wavelength and the linear excitation at the second harmonic depending on the pulse duration. The calculations have been carried out for various SH-conversions up to 30 %

The green line shows the excitation at the second harmonic and the red line by the fundamental wavelength. In case of the fundamental, linear as well as two-photon absorption was considered in our calculations. The contributions of linear and two-photon absorption are additionally shown in the dashed black lines.

In case of pure IR ablation the excitation process is initiated by linear absorption down to pulse durations of tens of nanoseconds. At a given pulse energy, for decreasing pulse lengths the two photon absorption process becomes more and more dominant which can be seen in

the bend of the curve in figure 61. In case of the two-colour scheme a conversion of just 1 % is sufficient to achieve a higher excitation by the second harmonic radiation with respect to pure IR excitation for pulse durations in the nanosecond time scale or longer. However the excitation by IR radiation is higher for pulses shorter than approx. 100 ns.

For a SH-conversion of 30 %, which turned out to be the value where saturation effects initiate, the two colour scheme is beneficial with respect to pure IR ablation down to pulse durations of approx. 10 ps.

Additional experiments have been carried out with a Ti:Sapphire system at 800 nm and a pulse duration of 50 fs. As predicted, the effect becomes insignificant, since sufficient conduction band population is provided by multiphoton absorption.

The experimental results show that the effect of ablation enhancement is very sizable especially for nanosecond pulses. Since ns-laser systems are relatively simple and inexpensive, the economical impact of this technique is obvious. The setup to realize the two color scheme is as simple by just placing a nonlinear crystal in the beam path and by using an achromatic lens.

7.4. Morphology

Figure 62 shows two images from the bottom of ablation cavities obtained at different time delays between the fundamental and SH pulses with a duration of 10 ps. Delays that result in enhanced yields also provide improved surface quality. When normalized to the ablation yield, the amount of debris on the surface surrounding of the cavity appears to be unaffected by the IR/SH delay.

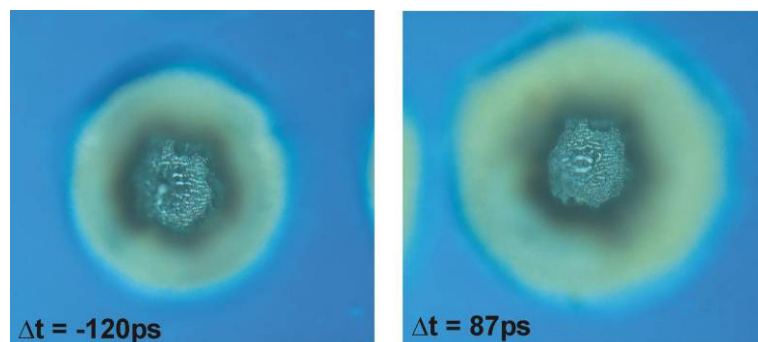


Figure 62: Images of two ablated cavities showing a clear dependence of the bottom surface quality on the delay time between fundamental and second harmonic pulse [P10]

Figure 63 shows the cross-section of two ablated cavities. On the left side the sample was treated with 100 pulses of the fundamental and the second harmonic with a conversion efficiency of 20 % and pulse durations in the nanosecond time scale. In the case of the cavity on the right side the SH-radiation was blanked out.

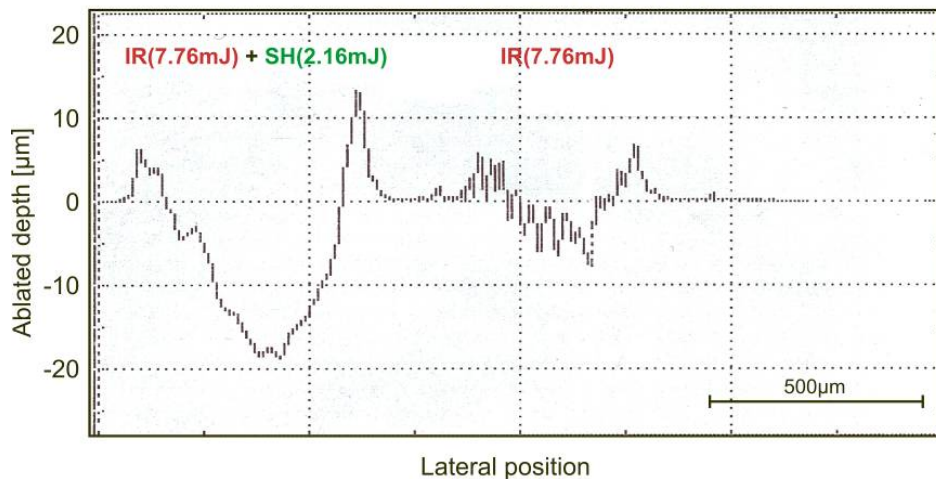


Figure 63: Cross-section of two ablated cavities. On the left side an additional fraction of SH (approx. 20%) contributes to the ablation process, which results in a much higher ablation rate and a decrease of the surface roughness [P2]

It can be seen that the shape of the cavity is well defined in the case of the two-color scheme whereas it is much more corrugated for ablation with the fundamental alone. Although the total intensity of the two cavities is somehow different, the difference between the ablation quality and yield is obvious.

The decrease in surface roughness in case of the two color scheme and the influence of the second harmonic fraction on the cavities is also shown in figure 64.

An array of laser ablated spots is shown where the upper row is treated with the two-color scheme (fund. + SH) whereas the harmonic radiation was blanked out by a dichroic mirror in the second line. Each position was treated with a burst of 100 pulses at pulse energies between 4.34 and 7 mJ.

The poor linear absorption of the fundamental wavelength results in narrow cavities with a strongly corrugated surface. The additional fraction of the SH wavelength (approx. 16 % of the total energy) results in cavities exhibiting a higher lateral dimension, a highly enhanced ablation rate and a smoother surface.

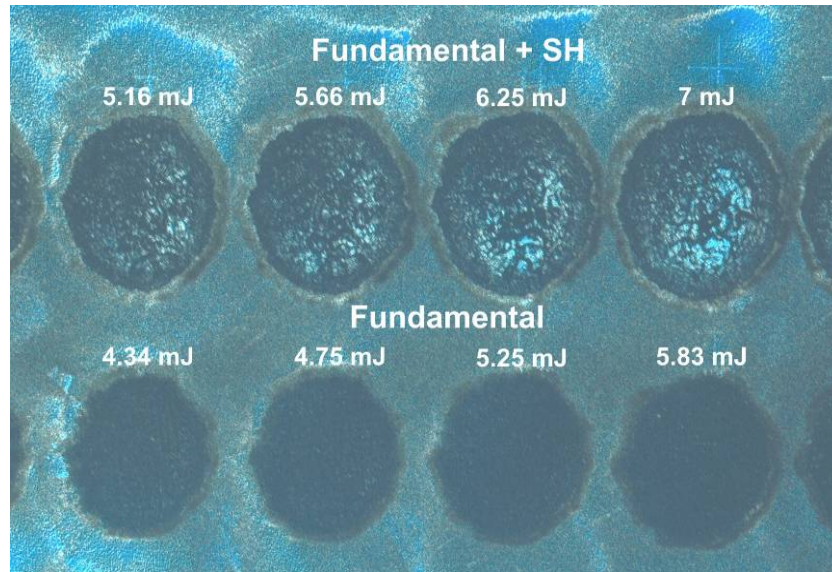


Figure 64: Silicon ablated with a pulse duration of 5 ns at different laser intensities. In the upper line the sample was treated with the two color scheme, in the second line the SH was blanked out by a dichroic mirror.

We attribute the quality enhancement to the fact that the SH absorption occurs within a very short penetration depth of about 1 μm , while TPA initially happens within the IR penetration depth of 100 μm .

Chapter 8: Morphological effects of laser ablation

Ripple formation

One of the morphological modifications occurring during laser ablation is the formation of ripple structures. This phenomenon has been observed for various laser parameters and different materials like metals [51] as well as semiconductors [16],[91] and dielectrics [9] and has also been found in the course of this work. Especially in microstructuring applications these ripples are usually an undesired side effect reducing the structure quality. In ultrashort pulsed laser ablation the formation of ripples is nearly unavoidable. We have observed these modifications in metals (e.g. Ni, Cu, steel) as well as in semiconductors (Si, GaAs).

Various attempts have been made to explain the origin and period of these ripples. Up to this date, however, no consistent theory has been developed. The most established explanation is based on the interference of the incident beam with the diffracted wave travelling very nearly along the surface [118]. In this theory the diffracted wave evolves due to random surface disturbances working as surface gratings. According to this theory the ripple spacing is given by

$$\Lambda = \frac{\lambda}{1 \pm \sin \theta} \quad \text{Equ. 35}$$

where θ is the angle of incidence in respect to the sample surface normal. In various publications dealing with ultrashort pulse-material interactions, the ripple period for normal incidence agrees well with this theory where the observed period of approx. 800 nm corresponds to the wavelength of the most frequently used Ti:Sapphire laser. In the present work we also observed a ripple period of 800 nm, however, with a laser wavelength of 1064 nm. We also studied the dependence of the ripple period on the angle of incidence for both, s- and p-polarized light. The material used was a polished silicon wafer <100>.

The results are shown in figure 65 and they are in complete disagreement with this theory. In the case of p-polarization the ripple spacing decreases with increasing angle. The decay is in agreement with equation 35 in the case of a positive sign in the denominator but with the assumption of a wavelength of 800 nm. In the case of s-polarized light the ripple period increases slightly with increasing values of the angle of incidence, which is not in accordance with the theory that would expect a steeper rise.

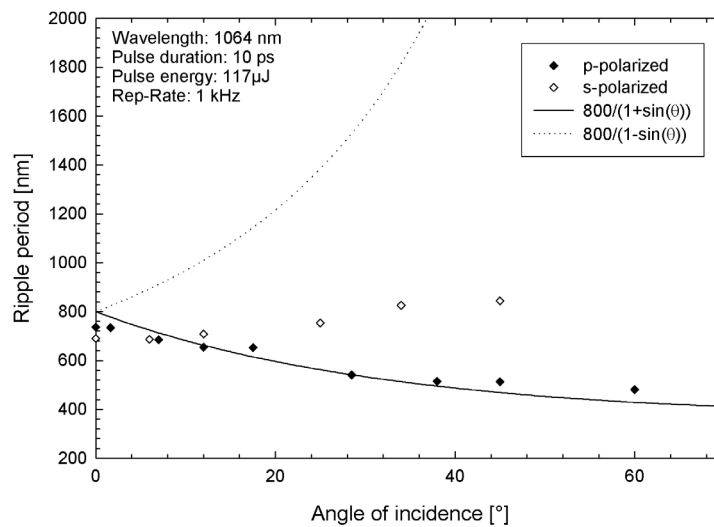


Figure 65: In this figure the ripple spacing depending on the angle of incidence is shown for p- and s-polarized light; the material used for the experiments was a polished silicon wafer

Generally the ripples can be divided in two groups depending on their characteristics. The first group consists of concentric fringes centered at a few locations and spread out over the ablated area.

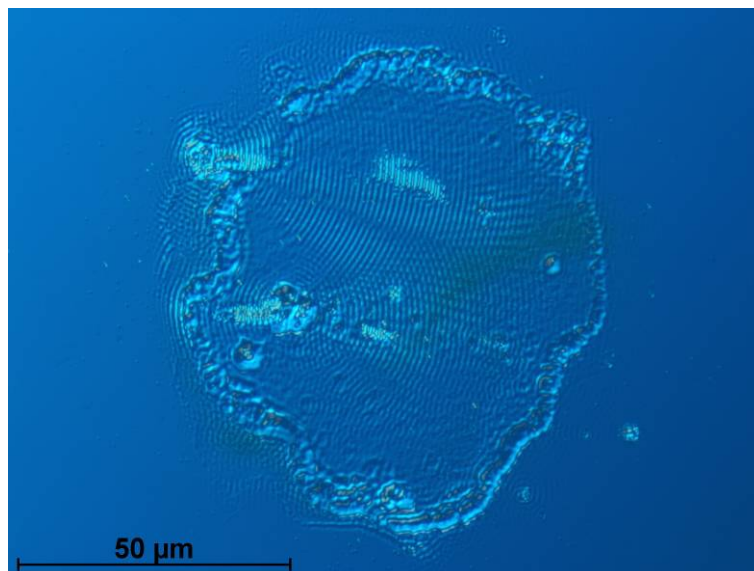


Figure 66: Ablated area of Si single crystal <100> after treatment with a single pulse with a fluence of 1.3 J/cm² at a wavelength of 1064 nm and a pulse duration of 12 ps. The image is taken with a light microscope with DIC (differential interference contrast)

In figure 66 the surface of a silicon wafer is shown after treatment with a single pulse at a fluence of 1.3 J/cm^2 ($\lambda=1064 \text{ nm}$, $\tau=12 \text{ ps}$). The ripple formation is enhanced with increasing fluence. It can be seen that the origins are surface defects or bubbles which evolve in the liquid phase during ablation.

Dauscher and coauthors [3] have observed these ripples during ablation of iron with pulses in the nanosecond time scale and explained them by the interference of the incident radiation with the scattered light at a point defect. This explanation would be consistent with our observations because the measured ripple period ($\Lambda=1 \mu\text{m}$) is in the range of the wavelength used.

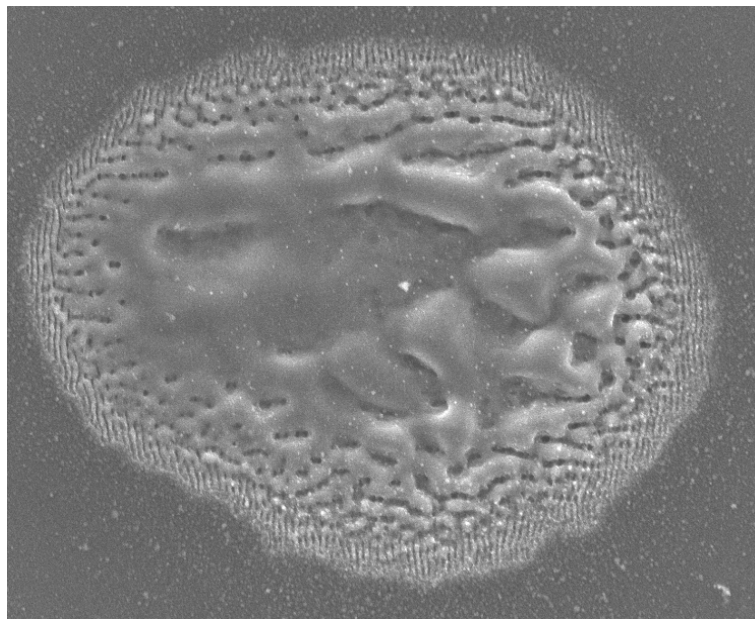


Figure 67: Silicon surface ablated with a burst of 50 pulses at a wavelength of 1064 nm and a pulse duration 10 ps; the experiment was carried out in air

The second group of ripples develops during multi pulse treatment at fluences slightly above the ablation threshold. In the multipulse regime a ripple structure evolves which is independent of the number of additional shots and the initial surface conditions. For treatment with higher fluences melting occurs in the center of the laser spot suppressing the ripple formation in this area. Under this condition the ripple structures just appear at the boundary of the ablated cavity. Ripples exhibiting these characteristics have not been observed after ablation with one laser pulse. In figure 67 an ablated area of a silicon sample is shown which has been exposed with 50 pulses with a duration of 10 ps and a wavelength of 1064 nm. The experiments were done in air. A significant feature of these ripples is that their orientation is perpendicular to the polarization of the laser light. Various theories about

the formation of this phenomenon have been given in terms of frozen surface acoustic waves [31], plasmon condensation [48] or interaction of the light with pre-existing surface defects [77],[79]. For circularly polarized light the formation of the periodic structures can not be observed but the surface shows small dots. Van Driel and his coworkers [38] carried out studies with linear as well as circular polarized light where the Fraunhofer diffraction pattern of the ablated area has been studied. For normal incidence and linear polarization the orientation of the ripples was, as expected, normal to the polarization of the light. For circular polarization the material (Ge) exhibits a speckled surface and the corresponding diffraction pattern displays a circle. As a consequence the absence of the typical structures was explained by a superposition of isotropically oriented ripples along the surface.

The ripple formation is a side effect which is distinctive in ultrashort pulsed laser ablation. For many applications like thin film structuring, drilling or cutting, it is an undesired phenomenon decreasing the quality. In figure 68 an image of a cutting edge in silicon carbide single crystal (cubic) is shown. The laser used for the experiments provided radiation at a wavelength of 1040 nm and a pulse duration of 300 fs. The cut velocity in this case was 10 mm/s and the fluence was 36 J/cm². The polarisation was perpendicular to the vector velocity. Although the quality of the cutting edge is high and the surrounding area of the cut shows no thermal damage, the micrograph on the right side shows that the surface roughness is superpositioned by a ripple structure. The brighter areas near the cutting edge are surface ripple structures evolved at laser fluences close to the ablation threshold.

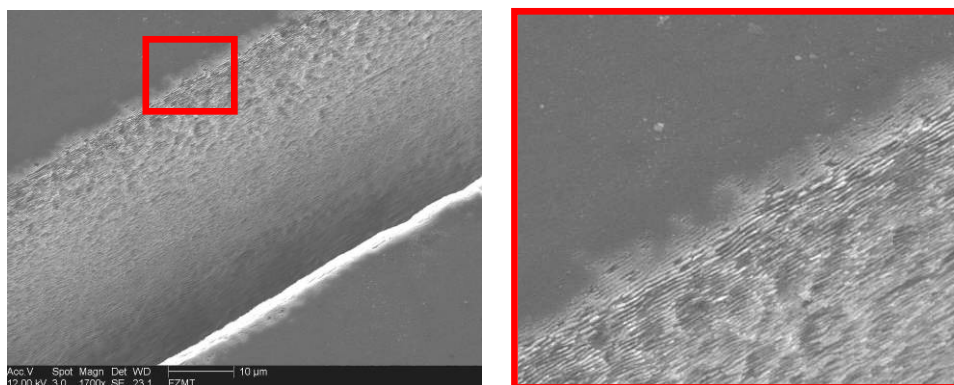


Figure 68: Laser cut made in 3C-SiC with a pulse duration of 300 fs at a wavelength of 1040 nm. The image shows a magnified section of the cut. The surface roughness is superpositioned by a ripple structure. The cutting edge exhibits no heat affected zone. The brighter areas near the cutting edge are surface ripple structures evolved at laser fluences close to the ablation threshold.

However, there are applications where a certain surface texture offers new characteristics. One example is the generation of hydrophobic surfaces due to the so called lotus effect, a self-cleaning property found with lotus plants. Another possible application is the modification of the surface of implants to enhance the bone-bonding.

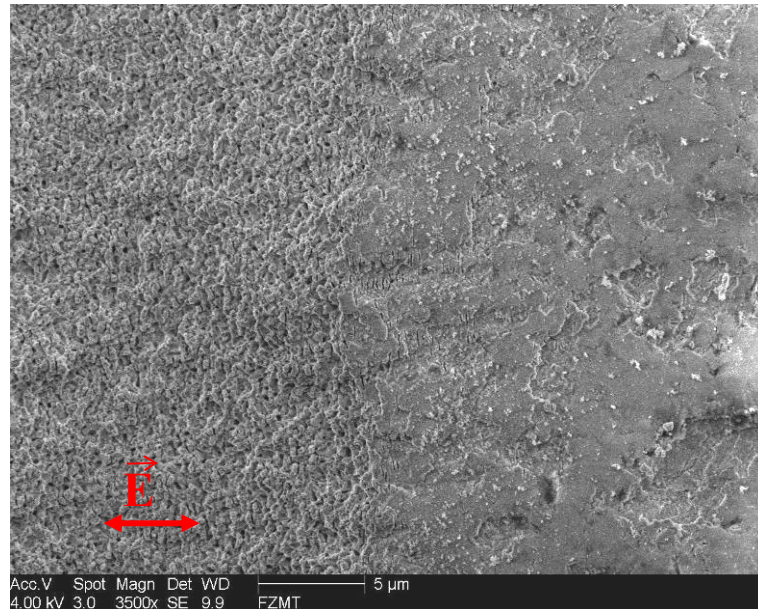


Figure 69: Surface of ZrO₂ ceramic, laser surface scanned on the left side, initial surface on the right side of the figure. The fluence was slightly above the ablation threshold which permits the generation of submicron features.

By suitable scanning algorithms and laser fluences slightly above the ablation threshold, large surface areas can be modified and covered with periodic structures of sub-micron dimensions. Figure 69 shows the surface of ZrO₂, a ceramic material which is used for implants, scanned with a laser beam at a wavelength of 1040 nm and a pulse duration of 330 fs. The laser was operated at a repetition rate of 1 kHz and the processing speed was 1 mm/s. The beam with a pulse energy of 40 μJ was focussed by a single lens (100 mm focal length) down to a diameter of 60 μm. On the right side the material surface is in its original condition. Compared to the untreated surface the laser ablated area shows feature sizes in the range of 200 to 400 nm. Due to the laser fluence slightly above the ablation threshold no significant material removal takes place. The sample shows no redeposition of ablated material. The sample was not treated with any cleaning procedure after ablation. The orientation of the electric field vector was perpendicular to the movement of the laser beam. With a line to line distance of 5 microns a high degree of beam overlap can be achieved resulting in a homogenous modification of the surface.

Chapter 9: Conclusions

While laser materials processing is well established in engineering, for example as a tool for welding or cutting, it is becoming a valuable new tool for micro machining. With the development of powerful ultrafast lasers, novel ablation mechanisms that yield high quality machined surfaces without thermal damage to the remaining substrate has become feasible.

In this work laser ablation with the focus on micro structuring, predominantly with ultrafast laser sources, has been investigated. The experiments were concentrated on selected semiconductors and dielectrics, materials which are intrinsically tied to the fabrication of micro systems.

A part of the work was concentrated on selected materials which are important in the field of microtechnology but could be processed with conventional methods just with difficulty. Especially SiC is the material of choice for high power, high frequency and high temperature electronics due to its outstanding properties where Si reaches its limits. In terms of structuring, the very same material properties render SiC a very difficult material, requiring electrochemical etching or high intensity plasma etching with low etching rates.

We have studied laser ablation of silicon carbide as a process for microtechnology. Our studies were focused on cubic 3C-SiC, which is one of the most auspicious polytypes. Experiments have been carried out with conventional excimer lasers emitting at 193 and 248 nm and solid-state lasers providing ultrashort pulse durations. The last mentioned system permits through drilling of 400 μm thick wafers with high quality and drilling speed.

It is well known that the wavelength, the pulse duration and the intensity of the ablation laser are parameters which significantly influence the ablation interaction process. To enable laser ablation of semiconductor or dielectric materials UV-photons have to be employed to bridge the band gap to provide sufficient absorption. Although working with high energy photons we have shown a considerable influence of the pulse duration on the ablation result, especially in structuring of mechanically sensitive materials like strontium titanate as a representative material. Earlier studies, however, have shown that laser machining of SrTiO_3 with nanosecond lasers suffers from the tendency of this material to form cracked surfaces. By the comparison of UV nanosecond and sub-picosecond ablation of SrTiO_3 we have shown that the formation of cracks in laser ablation can be avoided by using pulses in the femtosecond timescale. The formation of cracks is the result of a thermal shock affecting the material when using nanosecond pulse durations. The comparison of the ablation parameters has shown an order of magnitude lower ablation threshold and a higher ablation rate for

ultrashort pulses. The cavities ablated with femtosecond pulses show no indication of melting and exhibit smooth and well-defined surfaces.

Nevertheless femtosecond pulses require complex and expensive sources and are difficult to handle because of pulse dispersion in the steering and focusing optics. Lasers with longer pulse durations are far less efficient than femtosecond lasers in producing the required initial free carrier population and tend to waste a considerable amount of energy by transmission into the substrate before a significant conduction band population can build up. On the basis of these considerations we investigated a two-color ablation scheme where the excitation of the material and the consecutive ablation are regarded individually by providing each process with the suitable wavelength at an optimized intensity ratio. The experiments were carried out with silicon and silicon carbide at pulse durations from the nanosecond down to the femtosecond time regime.

The experiments with nanosecond radiation have shown an ablation rate enhancement of the two-color scheme of approx. 160% with respect to the fundamental ablation at the same intensity. This considerable enhancement can be achieved by an industrial relevant “one-laser solution” by converting a small fraction of the IR fundamental to its second or third harmonic. The harmonic fraction serves to generate free carriers in the material by linear absorption. The excited electrons gain energy from the laser field with a rate that scales with the square of wavelength making this process most efficient at the fundamental wavelength. We found that the conversion ratio shows an optimum value where sufficient free carriers are provided by the harmonic wavelength to start the heating and the ablation process by the fundamental.

Besides the highly increased yield an improved quality of the ablated cavities can be observed. The two-color concept benefits from the lossless conversion of the fundamental to its harmonic wavelength whereas pure frequency converted solutions suffer from an unavoidable energy loss due to the limited conversion ratio to the harmonic wavelength.

A possible application which could benefit from these results is for example wafer dicing. Wafer dicing of silicon with lasers is getting more and more attractive due to the scaling down of the wafer thickness where the conventionally used mechanical saws are reaching their limits.

Due to the nonthermal nature of the ablation process ultrashort pulses exhibit sharp ablation thresholds. Utilizing this attribute in combination with the high flexibility of a focused laser beam we developed methods for selective laser structuring of thin metallic and dielectric layers as well as thick photoresists on dielectric substrates. In this connection we established a method to define parameter windows for selective ablation which is based on the determination of ablation threshold.

We have studied, as prototypical systems for solar cell applications, the ablation of molybdenum, tin dioxide and zinc oxide on glass substrates. Apart from the determination of the threshold fluences of the various layer material and substrates we have also investigated the process speed. It is possible to completely remove the thin films of either material by one scan at velocities of 1 mm/s at a repetition rate of 10 kHz. An extrapolation to a repetition rate of 1 MHz, available with state-of-the-art systems, promises a process speed as high as 100 mm/s meeting industrial demands.

Another approach on selective laser ablation is the direct structuring of photoresist on glass. Conventional methods in microtechnology use lithography steps for the pattern generation. In case of an early stage of development where normally manifold design changes are needed, the use of a mask can lead to considerable delay times. Based on these considerations we adopted the selective ablation scheme for the direct structuring of resist with a focused Gaussian laser beam. This allows a developmentless and a maskless 2½-dimensional structure generation. In this fashion the substrate operates as an etch-stop layer. By employing a thin sacrificial resist layer the debris generated during laser structuring can be removed without any residues leading to high quality surfaces.

References

- [1] A. Athanassiou, M. Lassithiotaki, D. Anglos, S. Georgiou, C. Fotakis, *Appl. Surf. Scie.* **154-155**, 89-94 (2000).
- [2] A. Cavalleri, K. Sokolowski-Tinten, J. Bialkowski, M. Schreiner, D. von der Linde, *J. Appl. Phys.* **85**(6), 3301-3309 (1999).
- [3] A. Dauscher, V. Feregotto, P. Cordier, A. Thomy, *Appl. Surf. Scie.* **96-98**, 410-14 (1996).
- [4] A. Goetzberger, C. Hebling, *Sol. Energy Mater. Sol. Cells* **62**, 1-19 (2000).
- [5] A. Ruf, P. Berger, F. Dausinger, H. Hügel, *J. Phys. D: Aool. Phys.* **34**, 2918-2925 (2001).
- [6] A.D. Compaan, I. Matulionis, S. Nakade, *Opt. Las. Eng.* **34**, 15 (2000).
- [7] A.T. Findikoglu, Q.X. Jia, X.D. Wu, G.J. Chen, T. Venkatesan, and D.W. Reagor, *Appl. Phys. Lett.* **68**, 1651-1653 (1996).
- [8] A. Vogel, S. Busch, K. Jungnickel, R. Birngruber, *Lasers Surg. Med.* **15**, 32-43 (1994).
- [9] B.C. Stuart, M.D. Feit, S. Herman, A.M. Rubenchik, B.W. Shore, M.D. Perry, *Phys. Rev. B* **53**(4), 1749-61 (1996).
- [10] C.A. Zorman, M. Mehregany, *Mater Sci Forum* **457-460**, 1451-1456 (2004).
- [11] Connell, G. A. N., Paul, W.: *J. Non-Cryst. Solids* **8-10**, 215 (1972).
- [12] D. Ashkenasi, G. Mulller, A. Rosenfeld, R. Stoian, I.V. Hertel, N.M. Bulgakova, E.E.B. Campbell, *Appl. Phys. A* **77**, 223-228 (2003).
- [13] D. Ashkenasi, M. Lorenz, R. Stoian, A. Rosenfeld, *Appl. Surf. Scie.* **150(1-4)**, 101-106 (1999).
- [14] D. Basting, G. Marowsky: *Excimer laser technology*, Springer, Berlin, 2005, ISBN 3-540-20056-8.
- [15] D. Bäuerle: *Laser processing and chemistry*, Springer, Berlin, 2000.
- [16] D. Jost, W. Luethy, H.P. Weber, R.P. Salathé, *Appl. Phys. Lett.* **49**(11), 625-7 (1986).
- [17] D. Most, J. Choi, L.J. Belenky, C.B.Eom, *Solid-State Electronics* **47**: 2249-2253 (2003).
- [18] D. Meschede: *Optik, Licht und Laser*, Teubner, Leipzig 1999.
- [19] Dalven, R. *J. Phys. Chem. Solids* **26**, 439 (1965).
- [20] David R. Lide: *CRC handbook of Chemistry and physics*, CRC Press, 8th edition, 2004/2005.
- [21] D. von der Linde, K. Sokolowski-Tinten, *Appl. Surf. Scie.* **154-155**, 1-10 (2000).

- [22] E. Hecht: Optik, Oldenbourg, München 2001.
- [23] E. Martinez, S. Garcia, E. Marin, O. Vasallo, G. Pena-Rodriguez, A. Calderon, J.M. Siqueiros, J. Mat. Scie. **39**, 1233-1239 (2004).
- [24] F. Beinhorn, J. Ihlemann, K. Luther, J. Troe, Appl. Phys. A **79**, 869-873 (2004).
- [25] F. Benitez, F. Sanchez, V. Trtik, M. Varela, M. Bibes, B. Martinez, J. Fontcuberta, Appl.Phys.A 69, 501-504 (1999).
- [26] F. Dausinger, F. Lichtner, H. Lubatschowski: Femtosecond technology for technical and medical applications, Springer Verlag, 2004.
- [27] F.Dausinger: Riken Review **50**, 77 (2003).
- [28] F.Spaepen and D. Turnbull: Laser Annealing of Semiconductors, Academic, New York, 1982.
- [29] F.Theberge, S.L. Chin: Appl. Phys. A **80(7)**, 1505-1510 (2005).
- [30] G.A. Reider: Photonik. Eine Einführung in die Grundlagen, Springer, Wien 1997, ISBN3-211-82855-9.
- [31] G.N. Maracas, G.L. Harris, C.A. Lee, R.A. McFarlane, Appl. Phys. Lett. 33, 453 (1987).
- [32] Goldberg Yu., Levinshtein M.E., Rumyantsev S.L. in Properties of Advanced Semiconductor Materials GaN, AlN, SiC, BN, SiC, SiGe . Eds. Levinshtein M.E., Rumyantsev S.L., Shur M.S., John Wiley & Sons, Inc., New York, 93-148 (2001).
- [33] H. Cho, K.P. Lee, P. Leerungnawarat, S.N.G. Chu, F. Ren, S.J. Pearton, C.M. Zetterling, J Vac Sci Technol A **19(4)** 1878-1881 (2001).
- [34] H. Hügel: Strahlwerkzeug Laser, Teubner Studienbücher, Stuttgart, 1992.
- [35] H. Ishibashi, S. Arisaka, K. Kinoshita, T. Kobayashi, Jpn. J. Appl. Phys. **33(9A)**: 4971-4977 (1994).
- [36] H.J. McSkimin, P. Andreatch: J. Appl. Phys. **35** 2161(1964).
- [37] H.K. Toenshoff, A. Ostendorf, N. Baersch: In: *High-Power Laser Ablation 4* (Ed. By C.R. Phipps), Vol. 4760, p. 326. SPIE (2002).
- [38] H.M. Van Driel, J.E. Sipe, J.F. Young, Phys. Rev. Lett. 49(26), 1955-8 (1982).
- [39] Harris, G.L., Density of SiC , in Properties of Silicon Carbide. Ed. Harris, G.L., EMIS Datareviews Series, **N13**, 3 (1995).
- [40] Heltemes, E. C., Swinney, H. L.: J. Appl. Phys. **38**, 2387 (1967).
- [41] Ibach, H.: Phys. Status Solidi **33**, 257 (1969).
- [42] J. Hermann, M. Benfarah, S. Bruneau, E. Axente, G. Coustillier, T. Itina, J.-F. Guillemoles, P. Alloncle, J. Phys. D: Appl. Phys. **39**, 453-460 (2006).
- [43] J. Ihlemann, A. Scholl. H. Schmidt, Appl. Phys. A **60(4)**, 411-417 (1995).
- [44] J. Ihlemann, B. Wolff-Rottke, Appl. Surf. Scie. **106**, 282-286 (1996).

- [45] J. Zhang, K. Sugioka, S. Wada, H. Tashiro, K. Toyoda, Appl. Phys. A **64**, 367-371 (1997).
- [46] J. Zhang, K. Sugioka, S. Wada, H. Tashiro, K. Toyoda, K. Midorikawa, Appl.Surf.Sc. **127-129**, 793-799 (1998).
- [47] J. Zhang, K. Sugioka, T. Takahashi, K. Toyoda, K. Midorikawa: Appl. Phys. A **71**, 23 (2000).
- [48] J.A. Van Vechten, Solid State Commun. **39**, 1285 (1981).
- [49] J.-C. Diels, W. Rudolph: Ultrashort laser pulse phenomena, Academic Press, 1995.
- [50] J.F. Reintjes, J.C. McGroddy: Phys. Rev. Lett. **30**, 901 (1973).
- [51] J.F. Young, J. E. Sipe, H. M. van Driel, Phys. Rev. B 30(4), 2001-5 (1984).
- [52] J.H. Klein-Wiele, J. Bekesi, P. Simon, Appl. Phys. A **79**, 775-778 (2004).
- [53] J.J. Wang, W.S. Lambers, S.J. Pearton, M. Ostling, C.-M. Zetterling, J.M.Grow, F. Ren, R.J. Shul, Solid-State Electronics **42**, 2283-2288 (1988).
- [54] J.M. Liu, Opt. Lett. **7**, 196 (1982).
- [55] J.O.Bonse, S. Baudach, J.Kruger, W. Kautek, M. Lenzner: Appl. Phys. A **74**, 19 (2002).
- [56] J.T. Dickinson, L.C. Jensen, R.L. Webb, J. Appl. Phys. **74**(6): 3758-3767 (1993).
- [57] J.Zhang, K. Sugioka, S. Wada, H. Tashiro, K. Toyoda: Appl. Phys. A **64**, 477 (1997).
- [58] John F. Ready: Effects of high power laser radiation, Academic press, 1971.
- [59] K. Chen, J. Ihlemann, Appl.Phys. A **65**, 517-518 (1997).
- [60] K. Chen, J. Ihlemann, P. Simon, I. Baumann, W. Sohler, Appl. Phys. A **65**, 517-518 (1997).
- [61] K. Korte, S. Adams, A. Egbert, C. Fallnich, A. Ostendorf: Opt. Express **7**(2), 41(2000).
- [62] K. Obata, K. Sugioka, T. Akane, N. Aoki, K. Toyoda, K. Midorikawa: Appl. Phys. A **73** (2001).
- [63] K. Shibuya, T. Ohnishi, M. Lippmaa, M. Kawasaki and H. Koinuma, Appl. Phys. Lett. **85**(3), 425-427 (2004).
- [64] K. Zimmer, J. Dienelt, F. Herfurth, A. Braun, K. Otte, G. Lippold, V. Gottschalch, F. Bigl, Appl. Surf. Sci. **127-129**, 800 (1998).
- [65] K.P. Adhi, R.L. Owings, T.A. Railkar, W.D. Brown, A.P. Malshe, Appl. Surf. Scie. **225**, 324-331 (2004).
- [66] Katiyar, R. S., Dawson, P., Hargreave, M., Wilkinson, G. K.: J. Phys. **C4**, 2421 (1971).
- [67] Kern, E.L, Hamill, D.W., Deem, H.W., Sheets, H.D. Mater. Res. Bull. **4**, 25 (1969).
- [68] L. Dirnberger, P.E. Dyer, S.R. Farrar, Appl. Surf. Science **69**(1-4): 216-220 (1993)

-
- [69] L.Jiang, H.L.Tsai, J. Phys. D: Appl. Phys. **37**, 1492-1496 (2004).
 - [70] L. Patrick, W.J. Choyke, Phys. Rev. **186**(3), 775-777(1969).
 - [71] M. Farsari, G. Filippidis, S. Zoppel, G.A. Reider, C. Fotakis, J.Micromech.Microeng. **15**, 1786-1789 (2005).
 - [72] M. Mehregany, C.A. Zorman, Thin Solid Films **355-356**, 518-524 (1999).
 - [73] M. Niemz: Laser-Tissue Interactions. Fundamentals and Applications, Springer, Berlin, Second Edition, 1996, ISBN3-540-42763-5.
 - [74] M.D. Feit, A.M. Komashko, A.M. Rubenchik, Appl. Phys. A **79**, 1657-1661 (2004).
 - [75] M.D. Perry, B.C. Stuart, P.S. Banks, M.D. Feit, V. Yanovsky, A.M. Rubenchik, J. Appl. Phys. **85**(9), 6803-6810 (1999).
 - [76] M.H. Rice, J.M. Walsh: J. Chem. Phys. **26**, 824-830 (1957).
 - [77] M.J. Soileau, IEEE J. Qant. Electr., QE-20(5), 464-7 (1984).
 - [78] N. Bityurin, A. Malyshev, J. Appl. Phys. **92**(1), 605-613 (2002).
 - [79] N.R. Isenor, Appl. Phys. Lett. **31**, 148 (1977).
 - [80] P. Becker, K. Dorenwendt, G. Ebeling, R. Lauer, W. Lucas, R. Probst, H.J. Rademacher, G. Reim, P. Seyfried, H. Siegert: Phys. Rev. Lett. **46** 1540 (1981).
 - [81] P. Chabert, J Vac Sci Technol B **19**(4), 1339-1345 (2001).
 - [82] P. H. Yih, V. Saxena, and A. J. Steckl, Phys. stat. sol. (b) **202**(1), 605-642, (1997).
 - [83] P. Mandracci: Growth and characterization of SiC thin films by a plasma assisted technique for electronic applications; PhD thesis, Dip. Elettronica Politecnico di Torino (2001).
 - [84] P. Simon, J. Ihlemann, Appl Phys. A **63**,505-508 (1996).
 - [85] P. Stampfli, K. H. Benneman, Phys. Rev. B **49**, 7299 (1994).
 - [86] P.M. Sarro, Sens Actuators A **82**, 210-218 (2000).
 - [87] P.P. Pronko, S.K. Dutta, J. Squier, J.V. Rudd, D. Du, G. Mourou: Opt. Commun. **114**, 106 (1995).
 - [88] Patrick, L., Choyke, W.J. Static Dielectric Constant of SiC. Phys. Rev. **B 2**, 2255-2256 (1970).
 - [89] Peercy, P. S., Morosin, D.: Phys. Rev. **B7**, 2779 (1973).
 - [90] Philipp, H.R., Taft, E.A. Silicon Carbide - A High Temperature Semiconductor , Eds. O'Connor, J.R., Smiltens, J., Pergamon Press, Oxford, London, New York, Paris 1960, 366.
 - [91] Q. Wu, Y. Ma, R. Fang, Y. Liao, Q. Yu, X. Chen, K. Wang, Appl. Phys. Lett. **82**(11), 1703-5 (2003).

- [92] Q. Zhao, M. Lukitsch, J. Xu, G. Auner, R. Niak, P-K. Kuo, MRS Internet J. Nitride Semicond. Res. **5S1**, W11.69 (2000).
- [93] R. Dalven. J. Phys. Chem. Solids **26**, 439 (1965).
- [94] R. Stoian, D. Ashkenasi, A. Rosenfeld, E.E.B. Campbell, Phys. Rev. B **62(19)**, 167-173 (2000).
- [95] R. Stoian, M. Boyle, A. Thoss, A. Rosenfeld, G. Korn, I.V. Hertel, SPIE Proc. 4830 435-442, (2003).
- [96] R. Stoian, S. Winkler, M. Hildebrand, M. Boyle, A. Thoss, M. Spyridaki, E. Koudoumas, N.M. Bulgakova, A. Rosenfeld, P. Tzaneakis, C. Fotakis, I.V. Hertel: Mater. Res. Soc. **780** (2003).
- [97] R. Viana, P. Lunkenheimer, J. Hemberger, R. Bohmer, A. Loidl: Phys. Rev. B **50**, 601 (1994).
- [98] R.L. Webb, L.C. Jensen, S.C. Langford, J. Appl. Phys. **74(4)**: 2323-2337 (1993).
- [99] R.R. Gay, Sol. Energy Mater. Sol. Cells **47**, 19 (1997).
- [100] S. Bäuerle, E. Braun, V. Saile, S. Sprussel, E.E. Kock, Z. Phys. B **18**, 5177 (1978).
- [101] S. Kim, B.S. Bang, F. Ren, J. D'Entremont, W. Blumenfeld, T. Cordock, S.J. Pearton, J.Electr.Mat. **33(5)**, 477-80 (2004).
- [102] S. Preuss, A. Demchuk, M. Stuke, Appl. Phys. A **61(1)**, 33-37 (1995).
- [103] S. Rsys, H. Sadowski, R. Helbig, J. Solid State Electrochem. **3**, 437-445 (1999).
- [104] S.I. Ashitkov, A.V. Ovchinnikov, M.B. Agranat: JETP Letters **79**, 529 (2004).
- [105] S.M. Klimentov, S.V. Garnov, T.V. Kononenko, V.I. Konov, P.A. Pivovarov, F. Dausinger: Appl. Phys. A **69**, 633 (1999).
- [106] Slack, G. A. Phys. Rev. **6**, 3791 (1972).
- [107] Summitt, K.: J. Appl. Phys. **39**, 3762 (1968).
- [108] T. Wagner: Abtragen von Silizium mit ultrakurzen Laserpulslen. PhD thesis, Universität Hannover – Institut für Fertigungstechnik und Werkzeugmaschinen, Schönebeckerallee 2, 30823 Garbsen (2001).
- [109] T.F. Boggess, K.M. Bohnert, K. Mansour, S.C. Moss, I.W. Boyd, A.L. Smirl: IEEE J. Quantum Electron. **QE-22**, 360 (1986).
- [110] Tuerkes, P., Pluntke, Ch., Helbig, K.: J. Phys. C **13**, 4941 (1980).
- [111] Vogel, D., Krüger, P., Pollmann, J.: Phys. Rev. B **54**, 5495 (1996).
- [112] W. Kautek, J. Kruger, M. Lenzner, S. Sartania, C. Spielmann, F. Krausz: Appl. Phys. Lett. **69**, 3146 (1996).
- [113] W.-H. Chang, Sensor Actuat A **112(1)**, 36-43 (2004).
- [114] X.Liu, D. Du, G. Mourou: IEEE J. Quantum Electron. **QE-33**, 1706 (1997).
- [115] Y. Dong, C. Zorman, P. Molian, J.Micromech.Microeng. **13**, 680-685 (2003).

- [116] Y. Dong, P. Molian, Appl. Phys. A **77**, 839-846 (2003).
- [117] Yoshikawa, H., Adachi, S.: Jpn. J. Appl. Phys. **36**, 6237 (1997).
- [118] Z. Guosheng, P.M. Fauchet, A. E. Siegman, Phys. Rev. B **26(10)**, 5366-5381 (1982).

List of Publications

- [P1] S. Zoppel, H. Huber, G.A. Reider, Selective ablation of thin Mo and TCO films with femtosecond laser pulses for structuring thin film solar cells, *Appl. Phys. A* **89(1)**, 161-163 (2007).
- [P2] S. Zoppel, J. Zehetner, G.A. Reider, Two color laser ablation: Enhanced yield, improved machining, *Appl. Surf. Scie.* **253(19)**, 7692-7695 (2007).
- [P3] S Zoppel, D Gray, M Farsari, R Merz, G A Reider and C Fotakis: UV-femtosecond laser ablation of SrTiO₃ single crystals, *Journal of Physics: Conference Series* **59** (2007) 610–615.
- [P4] V. Wieger, S. Zoppel, and E. Wintner, Ultrashort Pulse Laser Osteotomy, *Laser Physics* **17(4)**, 438-442 (2007).
- [P5] D. Andrijasevic, W. Smetana, J. Zehetner, S. Zoppel, W. Brenner, Aspects of micro structuring low temperature co-fired ceramic (LTCC) for realisation complex 3D objects by embossing, *Microelectronic Engineering* **84(5-8)**, 1198-1201 (2007).
- [P6] J. Nicolics, L. Musiejovsky, J. Steurer, I. Giouroudi, H. Hauser, M. Mündlein, S. Zoppel, J. Zehetner, Laser Welding Process Optimization for the Production of Giant Magnetoimpedance Magnetic Field Sensors, *Sensor Letters* **5(1)**, 204-206 (2007).
- [P7] S. Zoppel, M. Farsari, R. Merz, J. Zehetner, G. Stangl, G.A. Reider, C. Fotakis, Laser micromachining of 3C-SiC single crystals, *J. Microelectr. Engin.* **83**, 1400-1402 (2006).
- [P8] S. Zoppel, J. Zehetner, G.A. Reider, Improved picosecond laser ablation with second harmonic seeding, *Photonics, Devices, and Systems III*, Pavel Tománek, Miroslav Hrabovský, Miroslav Miler, Dagmar Senderáková, Editors, *Proceedings of SPIE*, Volume **6180**, 61801S (2006).

- [P9] A.Yousif, M. Strassl, V. Wieger, S. Zoppel, E. Wintner, Oral Applications of Ultra-Short Laser Pulses - a New Approach for Gentle and Painless Treatment?, High-Power Laser Ablation VI. Edited by Phipps, Claude R.. Proceedings of the SPIE, Volume **6261**, 62611M (2006).
- [P10] S. Zoppel, R. Merz, J. Zehetner, G.A. Reider, Enhancement of laser ablation yield by two color excitation”, Applied Physics A **81**, 847-850 (2005).
- [P11] S. Zoppel, D. Gray, M. Farsari, R. Merz, G.A. Reider, C. Fotakis, Elimination of cracking during UV laser ablation of SrTiO₃ single crystals by employing a femto second laser, Applied Surface Science **252**, 1910-1914 (2005).
- [P12] M. Farsari, G. Filippidis, S. Zoppel, G. A. Reider and C. Fotakis, Efficient femto second lasermicromachining of bulk 3C-SiC, J. Micromech. Microeng. **15**, 1786-1789 (2005).

Conference Contributions

Invited Presentations

Heinz Huber, Sandra Zoppel, Max Lederer, Joerg Smolenski, Robert Braunschweig, Daniel Kopf, „High Repetition Rate Micromachining of Dielectrics and Ceramics with Ultrafast Lasers”, PHAST 2006 – Photonic applications system technologies, 22-25 May 2006 in Long Beach, California, USA

Oral Presentations

S. Zoppel, S. Partel, P. Choleva, M. Lederer, G.A. Reider, “Selective femtosecond laser micro-structuring of photoresists and TCO”, ICALEO 2007 - 26th International Congress on Applications of Lasers Electro-Optics, Oktober 29 - November 2, Orlando, Florida, 2007.

S. Zoppel, S. Partel, J. Zehetner, P. Hudek, G.A. Reider, „Selective Laser Ablation of Photoresists for MEMS Devices”, LPM 2007 - 8th International Symposium on Laser Precision Microfabrication, April 23-27, Vienna, Austria, 2007.

S. Zoppel, H. Zehetner, L. Musiejovsky, H. Hauser, and J. Nicolics, „Laser Micromachining for GMI-Sensors”, EMSA 2006 - 6th European Conference on Magnetic Sensors and Actuators, June 3-5, Bilbao, Spanien, 2006.

V. Wiegner, S. Zoppel, and E. Wintner, “Ultra-short pulse laser osteotomy”, LPHYS 2006 - 15th International Laser Physics Workshop, July 24-28, Lausanne, Switzerland, 2006.

S. Zoppel, S. Partel, J. Nicolics, G.A. Reider, J. Zehetner, „Laserablation und ihre Anwendung in der Mikrotechnik“, Dornbirner Mikrotechniktage, May 30/31, Dornbirn, Austria, 2006.

S. Partel, S. Zoppel, P. Hudek, T. Auer, J. Zehetner, W. Smetana, H. Homolka, B. Balluch, “Entwicklung zusammenhängender Fertigungsschritte für optische, elektrische und

fluidische Mikrosysteme“, Dornbirner Mikrotechniktage, May 30/31, Dornbirn, Austria, 2006.

A. Yousif, M. Strassl, V. Wieger, S. Zoppel, E. Wintner, “Oral Applications of Ultra-Short Laser Pulses - a New Approach for Gentle and Painless Treatment?”, Proceedings of the SPIE, High Power Laser ablation VI, Vol. 6261, ISBN 0-8194-6342-6, 2006.

Heinz Huber, Sandra Zoppel, Johann Zehetner, Robert Merz, Max Lederer, Wolfgang Seitz, Daniel Kopf, „High Repetition Rate Ultrafast Lasers and their Applications in Micromachining“, LAMP 2006 - The 4th International Congress on Laser Advanced Materials Processing, May 16-19, Kyoto, Japan, 2006.

S. Zoppel, J. Zehetner, G. A. Reider, “Improved picosecond laser ablation with second harmonic seeding”, Photonics Prague - The 5th International Conference on Photonics, Devices and Systems, June 8 - 11, Prague, Czech Republic, 2005.

J. Zehetner, S. Zoppel, R. Merz, H. Huber: Neue Pikosekundenlaserkonzepte und ihre Anwendungen, Laser in der Elektronikproduktion & Feinwerktechnik, Tagungsband: LEF 2005, Hrsg.: M. Geiger, S. Polster, Meisenbach Bamberg 2005.

Poster presentations

S. Zoppel, S. Partel, P. Choleva, P. Hudek, H. Huber, M. Lederer, J. Aus der Au, G.A. Reider, „Micro structuring of photoresist with femtosecond laser pulses“, Cleo Europe 2007 – Conference on lasers and electro-optics, June 17-22, Munich, Germany, 2007.

S. Zoppel, G.A. Reider, „Quality and yield enhancement of IR-laser ablation by harmonics seeding“, LPM 2007 - 8th International Symposium on Laser Precision Microfabrication, April 23-27, Vienna, Austria, 2007.

Daniela Andrijasevic, Walter Smetana, Johann Zehetner, Sandra Zoppel, Werner Brenner, „Aspects of micro structuring Low Temperature Cofired Ceramic (LTCC) for realisation complex 3D objects by embossing“, MNE 2006 - 32nd International Conference on Micro- and Nano-Engineering, September 17-20, Barcelona, Spain, 2006.

Sandra Zoppel, Max Lederer, Joerg Smolenski, Heinz Huber, Robert Braunschweig, Daniel Kopf, „Compact Ultrafast Lasers: Thin film structuring for photovoltaic applications”, ICALEO 2006, 25th International Congress on Applications of Lasers Electro-Optics, Oktober 30 - November 2, Scottsdale, Arizona, 2006.

Sandra Zoppel, Johann Zehetner, Georg A. Reider, „Two color laser ablation: enhanced yield, improved quality”, E-MRS - European Materials Research Society Spring meeting 2006, May 29 - June 2, Nice, France, 2006.

S.Zoppel, M.Farsari, C.Fotakis, G.A.Reider, “Micro structuring of 3C-SiC single crystals by laser ablation”, E-MRS - European Materials Research Society Spring meeting 2006, May 29 - June 2, Nice, France, 2006.

S. Zoppel, M. Farsari, R. Merz, J. Zehetner, G. Stangl, G. A. Reider, C. Fotakis, “Laser micro machining of 3C-SiC single crystals”, MNE 2005 - 31st International Conference on Micro- and Nano-Engineering, September 19-22 , Vienna, Austria, 2005.

S. Zoppel, D. Gray, M. Farsari, R. Merz, G. A. Reider, C. Fotakis, “UV-femtosecond laser ablation of SrTiO₃ single crystals”, COLA 2005 - 8th Conference on laser ablation, Banff, Canada, 2005.

M. Farsari , G. Filippidis, S. Zoppel, G. A. Reider, C. Fotakis, “Micromachining of Silicon Carbide using femtosecond lasers”, COLA 2005 - 8th Conference on laser ablation, Banff, Canada, 2005.

G. Stangl, G.A. Reider, S. Zoppel, W. Friza, A. Jarisch, “Overview on Ablation Techniques at wavelengths of 193 and 248 nanometers”, 7th International Conference on Laser Ablation, Crete, Greece, 2003.

List of figures

Figure 1: Schematic graph of the two-temperature model. When the energy deposition happens on an ultrashort time scale the heating of the electrons and the lattice has to be considered separately	14
Figure 2: Temperature of the electron system and the lattice versus time on the front (solid lines) and the back surface (dashed lines) of a 100 nm thin nickel foil irradiated with 200 fs pulses at 400 nm ($F \sim 234 \text{ mJ/cm}^2$). Thermal equilibrium is reached after a time of approx. 6 ps [15].....	16
Figure 3: Decay of the intensity versus penetration depth for different ratios of the linear and TPA coefficient. The axes are normalized to the initial intensity and to the optical penetration depth, respectively.....	17
Figure 4: Decay of the intensity versus distance for different values of the initial intensity.....	18
Figure 5: Evolution of the electron density due to multiphoton and avalanche ionization with respect to the intensity envelope of a Gaussian laser pulse [74].....	19
Figure 6: Cavity ablated in glass with a pulse duration of 300 fs at a wavelength of 1040 nm and a repetition rate of 1 kHz demonstrating high quality structuring by plasma-induced ablation with ultrashort laser pulses.....	20
Figure 7: Well-defined ablation thresholds in ultrashort pulsed laser ablation enables feature sizes smaller than the beam diameter by tuning the intensity close to the threshold value.....	21
Figure 8: Time scale of physical effects induced by optical breakdown after an estimated laser pulse of 30 ps. Cavitation and jet formation may only occur in soft or liquid materials [73].....	22
Figure 9: Schematical diagram showing the mechanism of material removal by coulomb explosion.....	23
Figure 10: Thermodynamic pathway during ablation schematically outlined in a P-V diagram of a material	24
Figure 11: Schematical drawing of the propagation of a shock wave through a slab of material [73].....	26
Figure 12: Shock and particle velocity versus shock wave pressure in water [73].....	27

Figure 13: Laser induced shock wave pressure versus distance from the centre of emission after optical breakdown in water. The values are calculated for pulses with a duration of 30 ps (50 μ J pulse energy) and 6 ns at 1 mJ, respectively [73]	28
Figure 14: Band structure and optical transitions of a direct (a) and an indirect semiconductor (b).....	30
Figure 15: The absorption coefficient [20] of Si highlighting the values for the fundamental and the second harmonic of the Nd:Van laser wavelength. The linear absorption of the fundamental is negligible. The absorption has to rely on two-photon transitions for this wavelength	32
Figure 16: Absorption coefficient of SrTiO ₃ at room temperature.....	33
Figure 17: Stacking order of three different SiC polytypes. It is indicated by the number of bilayers within the unit cell and a letter indicating the lattice symmetry.....	34
Figure 18: The absorption coefficient of cubic silicon carbide vs. photon energy for different electron concentrations T=300 K (1:relatively pure crystal, 2: Nd = 1019 cm ⁻³ [70]	34
Figure 19: Optical path for micromachining purposes with an excimer laser. An array of cylindrical lenses is used to achieve a constant intensity distribution in the homogenized plane.....	36
Figure 20: Setup used for direct structuring with a focussed beam. The sample was positioned on a 3-axis translation stage. The beam can be blanked by means of a electric mechanical shutter, operated by the motion controller of the motorized stage.	37
Figure 21: Setup of the knife edge method used to determine the 1/e ² diameter of the Gaussian beam shape in the ablation plane. The razor blade was fixed on a motorized translation stage with a resolution of 100 nm and an accuracy of 200 nm.....	39
Figure 22: Schematic diagram on the dependence of the ablated spot area on the pulse energy to determine the beam diameter as well as the ablation threshold of the treated material by means of a Liu-plot	40
Figure 23: Liu-plot to determine the single pulse ablation threshold of silicon and the beam diameter in the ablation plane.....	41
Figure 24: Optical Setup used for the determination of the ablation threshold and the ablation rate for experiments with the excimer lasers and the dye laser, respectively. For ns pulse durations the sample was placed in the conjugated plane of the aperture (1), for the UV-femtosecond pulses the sample was positioned closer to the lens (2) due to breakdown in air in the focal plane.	45

Figure 25: Cavity ablated with a pulse duration of 500 fs at a wavelength of 248 nm. The cross-section measured by a profilometer was transferred to Matlab® to calculate the ablated volume.	46
Figure 26: Comparison of the ablation rate of SrTiO ₃ for a wavelength of 248 nm at pulse durations of 34 ns and 500 fs, respectively. The dotted lines are a guide for the eye [P11]	47
Figure 27: Ablation rate of 3C-SiC for three different sets of laser parameters [P7]	48
Figure 28: Array of through-vias in a 3C-SiC wafer with a thickness of 400 µm drilled with a solid state laser providing pulses with a duration of 300 fs at a wavelength of 1040 nm. [P7].....	49
Figure 29: Comparison of cavities (3C-SiC) ablated with excimer lasers with pulse durations in the ns time scale and a wavelength of 193 nm (A) and 248 nm (B), respectively	50
Figure 30: Crack formation along the crystallographic axis of SrTiO ₃ after a single shot with a fluence of 1.5 J/cm ² , λ = 248 nm, τ = 34 ns [P11]	51
Figure 31: XRD-measurment of SrTiO ₃ . The sample has been exposed with fluences just below the ablation threshold. [P11].....	52
Figure 32: Ablated cavity in SrTiO ₃ after 100 shots at a fluence of 3.3 J/cm ² , λ = 248 nm, τ = 34 ns.....	53
Figure 33: Ablated structure in SrTiO ₃ , λ = 248nm, τ = 500fs.....	53
Figure 34: Schematic diagram of selective structuring of photoresist compared to bulk machining. The cross section of the ablated area exhibits a trapezoidal shape.	55
Figure 35: Schematic view of a copper indium selenide (CIS, upper side) and an a-Si solar cell. The transparent conductive oxide (TCO) and the Mo layer must be selectively ablated from the glass substrate for structuring the first layer	56
Figure 36: Thin film of molybdenum on glass structured at different velocities (0.5, 1, 2 and 4 mm/s) with a pulse energy of 800 nJ. The beam was focused to a diameter of 8.6 µm [P1]	57
Figure 37: Line ablated in Molybdenum with linear polarized light. At fluences close to the ablation threshold the well known effect of ripple formation can be observed. By employing circular polarization this effect can be practically avoided [P1]	58
Figure 38: Determination of the ablation threshold of ZnO and the substrate by plotting the ablated area versus pulse energy. The intersection with the ordinate indicates the ablation threshold. The range of fluences between the two threshold	

values defines a process window where the TCO film can be selectively removed from the substrate. [P1].....	59
Figure 39: Thin layer of zinc oxide (a) and tin dioxide (b) selectively ablated from the glass substrate with a fluence of 0.5 J/cm ² and 0.8 J/cm ² , respectively (10 kHz, 1 mm/s). [P1].....	59
Figure 40: Absorption coefficient of AZ [®] nLOF versus wavelength; the resist is a poor absorber at the second harmonic (520 nm) so the light-material coupling has to rely on two-photon absorption (source: Microchemicals GmbH).....	61
Figure 41: Determination of the multipulse ablation threshold of AZ [®] nLOF 2070. The sample was treated with a burst 500 pulses at a repetition rate of 1 kHz.....	62
Figure 42: Determination of the multipulse ablation threshold of borosilicate glass (D 263 T, Schott) for a pulse duration of 330 fs and a wavelength of 520 nm.	62
Figure 43: Test structures ablated on an 11 micron thick resist sample with a wavelength of 520 nm, a fluence of 0.4 J/cm ² , a repetition rate of 5 kHz and a scan velocity of 0.5 mm/s. The resist shows no tendency of local melting; the cutting edges are well defined and show no chipping of material as observed when using the fundamental wavelength.....	63
Figure 44: Test structures in AZ [®] nLOF 2070 selectively removed from a glass substrate with a fluence of 0.35 J/cm ² , a repetition rate of 5 kHz and a scan velocity of 5 mm/s.....	64
Figure 45: Structure showing a partial stripping of the resistlayer from the substrate after treatment in an ultrasonic bath to remove the recast layer on the top surface.....	65
Figure 46: Structures generated in AZ [®] nLOF 2070 by selective laser structuring from a glass substrate; by employing a sacrificial resist layer (AZ [®] 6612), which can be solved by a subsequent rinse step, the debris on the top surface can be completely removed.....	66
Figure 47: Rectangular test structures with varying scanning recurrences; measurements carried out with a White-Light Interferometer show a top view and a cross section of two ablated areas after one and two recurrences, respectively. The areas were scanned vertically with a pitch of 10 µm and a vector velocity of 1 mm/s. The laser beam was attenuated to a pulse fluence of 0.4 J/cm ² at a repetition rate of 5 kHz.	66
Figure 48: Six rectangular test structures in photoresist AZ [®] nLOF 2070, selectively ablated from a glass substrate with a pulse duration of 330 fs and a wavelength of 520 nm. The bottom surface quality can be enhanced by repetitive scans. The rectangles show the quality after one repetition (b right) up to six repetitions (a left).....	67

Figure 49: Surface Roughness at the bottom of the ablated structure depending on the number of scans where R_a is the arithmetic mean surface roughness, R_q the root mean square (RMS) surface roughness and R_t the peak to valley height	68
Figure 50: Schematic setup for the two-color ablation experiments with the second harmonic and pulse durations in the nanosecond time scale.....	70
Figure 51: Ablation rate as a function of the SH-conversion, adjusted by tuning the phase matching angle. At an SH-conversion of approx. 27% the enhancement saturates.	71
Figure 52: Optical setup used for experiments with the third harmonic generated by sum frequency mixing. To avoid chromatic aberration the beam was focused by a mirror M3.....	72
Figure 53: Ablation rate of cubic silicone carbide versus the TH-conversion of the fundamental and the third harmonic. Although the conversion was limited due to the optical setu, an enhancement effect can be observed.....	72
Figure 54: Schematic diagram of the setup which allows time delays from -120 to +100 ps between the fundamental and the second harmonic. The pulse overlap was determined with a LBO-crystal by the detection of the sum frequency [P2].....	73
Figure 55: Ablation rate as a function of the time delay. For positive values of the delay the second harmonic pulse is earlier than the ablation pulse. The maximum enhancement occurs at approximately zero time delay, where the pulses are overlapping [P10].....	74
Figure 56: Experimental setup for ablation with time delayed laser pulses from an ArF-excimer laser and a Nd:VAN solid state laser. The time delay was realized electronically with an adjustable RC-element [P10].....	75
Figure 57: Ablation rate of silicon depending on the time delay between the IR pulse and the excimer laser ‘seed’ pulse [P10]	76
Figure 58: Ablation rate as a function of the intensity of the exciting pulse for delay times of 74% and -60ps, respectively [P10]	77
Figure 59: Single shot ablation threshold versus time delay between the SH and the fundamental pulse. [P2]	77
Figure 60: Determination of the threshold fluence for single pulse ablation of silicon with a pulse duration of 10 ps and a wavelength of 1064 nm. Assuming a Gaussian intensity profile the threshold fluence can be determined by plotting the ablated area vs. pulse energy.....	78

Figure 61: Comparison of the excitation rate at the fundamental wavelength and the linear excitation at the second harmonic depending on the pulse duration. The calculations have been carried out for various SH-conversions up to 30 %	80
Figure 62: Images of two ablated cavities showing a clear dependence of the bottom surface quality on the delay time between fundamental and second harmonic pulse [P10]	81
Figure 63: Cross-section of two ablated cavities. On the left side an additional fraction of SH (approx. 20%) contributes to the ablation process, which results in a much higher ablation rate and a decrease of the surface roughness [P2]	82
Figure 64: Silicon ablated with a pulse duration of 5 ns at different laser intensities. In the upper line the sample was treated with the two color scheme, in the second line the SH was blanked out by a dichroic mirror.	83
Figure 65: In this figure the ripple spacing depending on the angle of incidence is shown for p- and s-polarized light; the material used for the experiments was a polished silicon wafer.....	86
Figure 66: Ablated area of Si single crystal <100> after treatment with a single pulse with a fluence of 1.3 J/cm ² at a wavelength of 1064 nm and a pulse duration of 12 ps. The image is taken with a light microscope with DIC (differential interference contrast).....	86
Figure 67: Silicon surface ablated with a burst of 50 pulses at a wavelength of 1064 nm and a pulse duration 10 ps; the experiment was carried out in air	87
Figure 68: Laser cut made in 3C-SiC with a pulse duration of 300 fs at a wavelength of 1040 nm. The image shows a magnified section of the cut. The surface roughness is superpositioned by a ripple structure. The cutting edge exhibits no heat affected zone. The brighter areas near the cutting edge are surface ripple structures evolved at laser fluences close to the ablation threshold.....	88
Figure 69: Surface of ZrO ₂ ceramic, laser surface scanned on the left side, initial surface on the right side of the figure. The fluence was slightly above the ablation threshold which permits the generation of submicron features.	89
Figure 70: Veeco NT1100 Whitelight Interferometer.....	115
Figure 71: Schematic drawing of a white light interferometer. Depending on the magnification either a Michelson or a Mirau setup is used for the measurements.....	116

Index of symbols and abbreviations

A_L	m^2	laser spot area
c, c_0	ms^{-1}	speed of light, in vacuum $c_0 = 2,998 \cdot 10^8 \text{ ms}^{-1}$
$C_{e,l}$	JK^{-1}	heat capacity of electrons, lattice
e	C	elementary charge
E_F	eV	Fermi level
E_p	J	pulse energy
ϕ	Jm^2	fluence
h	Js	Planck constant $h = 6,626 \cdot 10^{-34} \text{ Js}$ $\hbar = h/2\pi$
$h\nu$	eV	Photon energy $h\nu [\text{eV}] \approx 1240 / \lambda [\text{nm}]$
I	Wm^{-2}	Intensity
k	m^2s^{-1}	thermal diffusivity
$K, K_{e,l}$	$\text{Wm}^{-1}\text{K}^{-1}$	Thermal conductivity, of electrons, lattice
k_B	J/K	Boltzmann constant
l_{diff}	m	thermal diffusion length
l_e	m	electron diffusion length
l_a	m	optical penetration depth
m_e	kg	electron mass
$N_e^{(cr)}$	m^{-3}	(critical) electron density
\tilde{n}	-	complex index of refraction
n	-	(real part of) index of refraction
p	Pa	pressure
R	-	Reflectivity
T	K	Temperature
T	-	transmission
u_s	ms^{-1}	shock wave velocity
α	m^{-1}	linear absorption coefficient
α_a	$\text{cm}^2\text{ps}^{-1}\text{GW}^{-1}$	avalanche coefficient
β	cmGW^{-1}	two-photon absorption coefficient
β_m	$\text{cmGW}^{(1-m)}$	m-photon absorption coefficient
κ	-	imaginary part of the index of refraction
λ	m	wavelength
ν	s^{-1}	frequency
ρ	kgm^{-3}	material density
σ_d	m^2	effective crosssection area for collisions
σ_m	m^2	multiphoton cross section
ω	s^{-1}	angular frequency

Γ_{e-ph}		electron-phonon coupling
α_{fc}	m^{-1}	free carrier absorption coefficient
ϵ_0	Fm^{-1}	permittivity of free space
τ_e	s	mean time of collisions between electrons
τ_p	s	pulse duration
ω_p	s^{-1}	plasma frequency

Appendix

A1: Measurement methods

White-light interferometer: Veeco NT1100

The Measurements of the surface topography and roughness as well as the determination of layer thicknesses were carried out with a White Light Interferometer Veeco NT1100 (see Figure 70). Compared to a profilometer it is possible to obtain three dimensional data of surfaces or structured samples.



Figure 70: Veeco NT1100 Whitelight Interferometer

The schematic setup of the white light interferometer is shown in Figure 71. The light from a halogen lamp is split into two beams either by a Mirau or by a Michelson interferometer. One beam is reflected by the sample, the other one by the reference mirror. The beams are recombined and registered by a CCD detector. There are two possible measurement techniques available depending on the required information. The one is the Phase Shifting Interferometry (PSI), the other one the Vertical Scanning Interferometry (VSI).

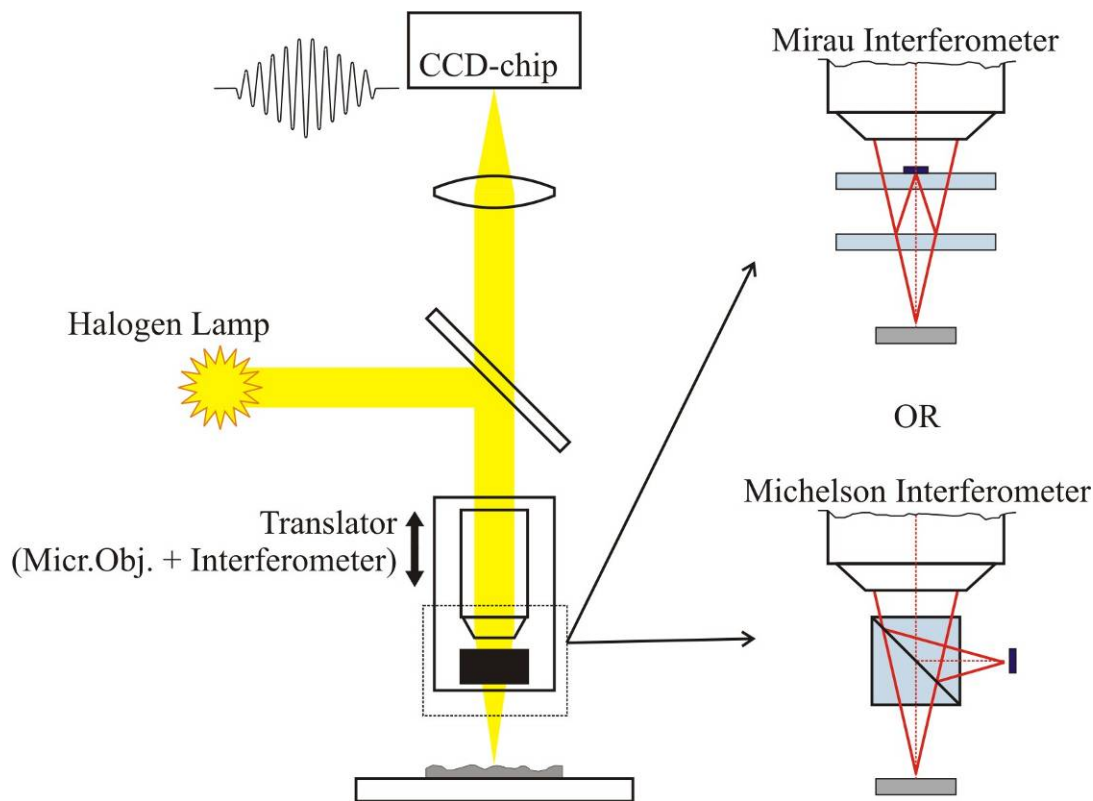


Figure 71: Schematic drawing of a white light interferometer. Depending on the magnification either a Michelson or a Mirau setup is used for the measurements

Vertical Scanning Interferometry (VSI) Mode

In this mode, the white light interferometer operates similar to a confocal microscope and scans a sample in the vertical direction. Due to the wide spectral bandwidth of the source the interferogram exhibits an envelope with its maximum at identical branch lengths. From this intensity maximum versus vertical height, a three-dimensional image can be formed.

VSI measurements are suitable for measurements with step heights greater than 160nm. The vertical resolution is around 5nm.

Phase Shifting Interferometry (PSI) Mode

This is a true interferometric technique in which monochromatic light (filter) is used for the measurement. PSI is suitable for measurements smaller than 150 nm ($\lambda/4$ of the wavelength) in height. In principle, topographical features smaller than 1nm can be measured with this mode.

A2: Selected material properties

	Si	3C-SiC	6H-SiC	SrTiO ₃	SnO ₂	ZnO
Crystal structure	diamond	zinc Blende	wurtzite	perovskite	rutile	wurtzite
Band gap [eV]	1.12	2.36 6 (direct) ^[93]	3 2.86 (direct) ^[90]	3.2	3.46 (direct)	3.4 ^[111]
Thermal conductivity [Wm ⁻¹ K ⁻¹]	130	3.6	4.9	12	98	54 ^[106]
Thermal diffusivity [m ² s ⁻¹]	0.8	1.6	2.2			
Specific heat capacity [Jg ⁻¹ K ⁻¹]	0.7	0.69	0.69		52.59 [Jmol ⁻¹ K ⁻¹]	
Melting point [°C]	1687	3103 ±40	3103 ±40	2080	1630	1975
Thermal expansion [K ⁻¹]	2.56·10 ⁻⁶ ^[80]	3.8·10 ⁻⁶ ^[32]	4.3·10 ⁻⁶ ^[67]	10.4·10 ⁻⁶	4·10 ⁻⁶ (⊥c) 3.7·10 ⁻⁶ (c) ^[89]	29.2·10 ⁻⁷ (to c-axis) ^[41] 47.5·10 ⁻⁷ (⊥ to c)
Density [gcm ⁻³]	2.33	3.21 ^[39]	3.21	5.13	6.994 ^[110]	5.606
Hardness Mohs scale	7	9.2-9.3		6-6.5		5
Surface Microhardness [kgmm ⁻²]	1150	2900-3100				
Bulk modulus [dyn/cm ²]	9.8·10 ¹¹	2.5·10 ¹² ^[32]	2.2·10 ¹²			
Acoustic wave speeds [10 ⁵ cms ⁻¹]	@298 K, p-type (ρ = 410 [Ωcm]) v ₁ = 8.4332 v ₂ = 5.8446 v ₃ = 9.1333 v ₄ = 5.8442 v ₅ = 4.6740 ^[36]	v ₁ = 9.5 v ₂ = 4.1 v ₃ = 9.95 v ₄ = 5.1 v ₅ = 2.9	v ₁ = 12.5 v ₂ = 7.1 (E [001]) v ₆ = 13.1 v ₇ = 7.1		v ₁ = 7.54 v ₂ = 5.27 v ₆ = 6.69 v ₇ = 2.82 ^[66]	v _{1,⊥c} = 6.0776 v _{3, c} = 6.0961 v _{4, c} = 2.7353 v _{4,⊥c} = 2.735
Dielectric constant	11.7 ^[11]	9.72 ^[88]	9.66	288 ^[97]	3.78 _{⊥c} / 4.17 _c ^[107]	7.8 _{⊥c} / 8.75 _c ^[40]
Absorption coefficient @ 1064 nm [m ⁻¹]	2.19·10 ³	4·10 ³		-	-	-
Absorption coefficient @ 532 nm [m ⁻¹]	1.46·10 ⁶	5·10 ³		-	-	53 ^[117]